공학박사학위논문

상압소결법으로 제작된 니켈/알루미나 경사기능재료의 재료 물성 및 소결 거동

Sintering Behavior and Material Properties of Nickel/Alumina Functionally Graded Materials Fabricated by Pressureless Sintering Method

2015 년 8 월

서울대학교 대학원

기계항공공학부

이 재 철

상압소결법으로 제작된 니켈/알루미나 경사기능재료의 재료 물성 및 소결 거동

Sintering Behavior and Material Properties of Nickel/Alumina Functionally Graded Materials Fabricated by Pressureless Sintering Method

지도교수 안 성 훈

이 논문을 공학박사 학위논문으로 제출함

2015 년 4 월

서울대학교 대학원

기계항공공학부

이 재 철

이재철의 공학박사 학위논문을 인준함

2015 년 6 월

위 원 장 : _____

부위원장 : _____

위 원 : _____

위 원 : _____

위 원 : _____

Abstract

Sintering Behavior and Material Properties of Nickel/Alumina Functionally Graded Materials Fabricated by Pressureless Sintering Method

Jae-Chul Lee
School of Mechanical and Aerospace Engineering
The Graduate School
Seoul National University

In this study, a heat-resistant material is developed to increase the operating temperature as a strategy for increasing the thermal energy efficiency. To do so, the use of FGMs is introduced. As a heat shielding material, alumina was used, and nickel was employed as the structural material of the FGM. The powder metallurgy process and the pressureless sintering method were used for efficient and cost-efficient manufacturing of the FGM.

To allow mechanical engineers without a strong background in material science to develop FGM parts, a system making use of a material science database was required. To make this system, the variables to be considered for the design and fabrication of FGMs from the materials science field should be input into the database; the experiments required from the materials science field should be standardized; and the number of required experiment should be reduced.

A measurement method and estimated models of material properties including the following have been studied in the thesis.

1. A measurement method of porosity for each layer of a FGM

2. A method and a model to estimate material properties depending on porosity for the fabricated nickel/alumina FGM

3. A method and a model to predict sintering shrinkage of each layer of a FGM

A precise measurement method for the porosity of the FGM, an estimation method for the material properties depending on porosity of the FGM, and an estimation model that can predict the sintering shrinkage with a minimal number of experiments are suggested in this study as basic research for the development of a database of the materials science field. To confirm the reliability of the estimation model, an analysis of the results using estimated values from the estimation model were compared with measured values of fabricated FGMs. The proposed estimation models in the study are determined to be reliable using the comparison results.

When a mechanical engineer who designs and fabricates a FGM uses the database employing basic data made by this study, it is possible to predict the stress and displacement of the FGM. Finally, a FGM providing excellent performance can be manufactured using this database system.

Keywords: Nickel/Alumina Functionally Graded Materials, Porosity measurement method, Estimation model of material properties, Estimation model of sintering shrinkage, Numerical analysis of thermal residual stress

Student Number: 2005-31034

Contents

List of Tables

List of Figures

Chapter 1. Introduction

1.1 Functionally Graded Materials

In general, homogeneous material have uniform functions and/or properties. However, if one side has high mechanical strength and the other side has high thermal resistant property, there are "two aspects" in one material. However, this difference in material properties generates stress concentrations or delamination at the interface of the two substances because of discontinuous properties.

To overcome this problem, gradual changes (gradient) of compositions and/or functions are inserted at the interface of the two substances, which is called a Functionally Graded Materials (FGMs). In other words, FGMs are materials whose compositions and/or functions vary continuously or step-wisely from one side to the other side. Typically, these materials are made from engineering ceramics and metals, as shown in Figure 1.1.

Engineering ceramics are useful due to their high compressive strength and thermal applications, however suffers from low fracture toughness. On the contrary, a metal exhibits better tensile strength and thermal shock resistance but cannot withstand exposure to high temperatures. From the mixture of these materials, a FGM can withstand high-temperature environments while maintain their structural integrity. For example, a plate used as a thermal barrier may be graded through the thickness direction from ceramic on the face of the plate that is exposed to high temperature to metal

on the other face of the plate that maintains their structural integrity. Due to these advantages, various concepts for FGMs have been introduced and applied to many engineering parts in fields such as aeronautics, industrial materials, optoelectronics, energy materials, biomaterials, and others.

In FGMs, change of compositions is continuous or step-wised. The continuous-type (particulate type) has continuous and gradient functions without generating any boundary by mixing two particles of different functions. This type has the advantages that properties are continuous and there are no stress concentrations throughout the FGM. However, it presents difficulties in terms of design and manufacturing. On the other hand, the step-wised-type (layered type) has boundaries between the bonded individual compositions. Thus, properties are discontinuous and stress concentration can occur in the FGM. However, this type can be obtained allowable stress according to design parameters such as volume fraction and thickness, and it can overcome the limitations caused by discontinuous properties in the boundary of the different composition layers. Manufacturing of this type of FGMs is easier and cheaper than the continuous-type. Figure 1.2 shows the change in composition throughout a plate for both types of FGMs. The bright and dark areas correspond to ceramic and metal particles, respectively. Figure 1.2 (a) shows the continuous-type FGM where the substance compositions are varied continuously though the thickness direction. In addition, Figure 1.2 (b) presents the step-wised-type FGM made of numerous layers.

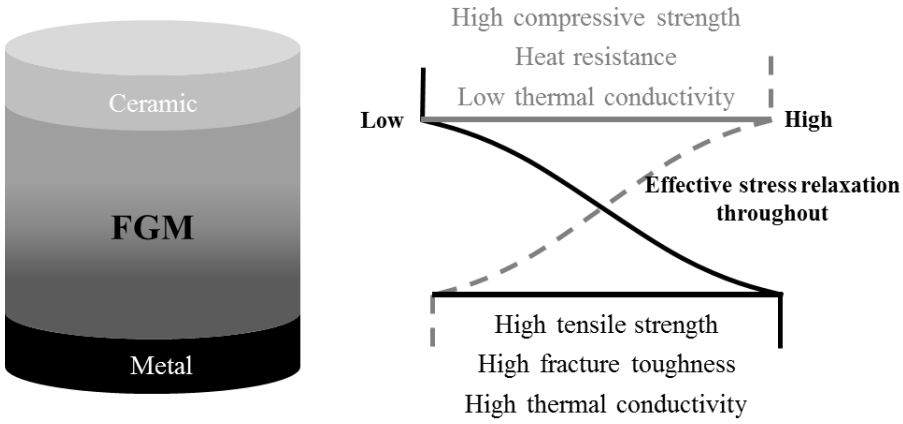

Figure 1.1 A typical functionally graded materials consisting of metal and ceramic

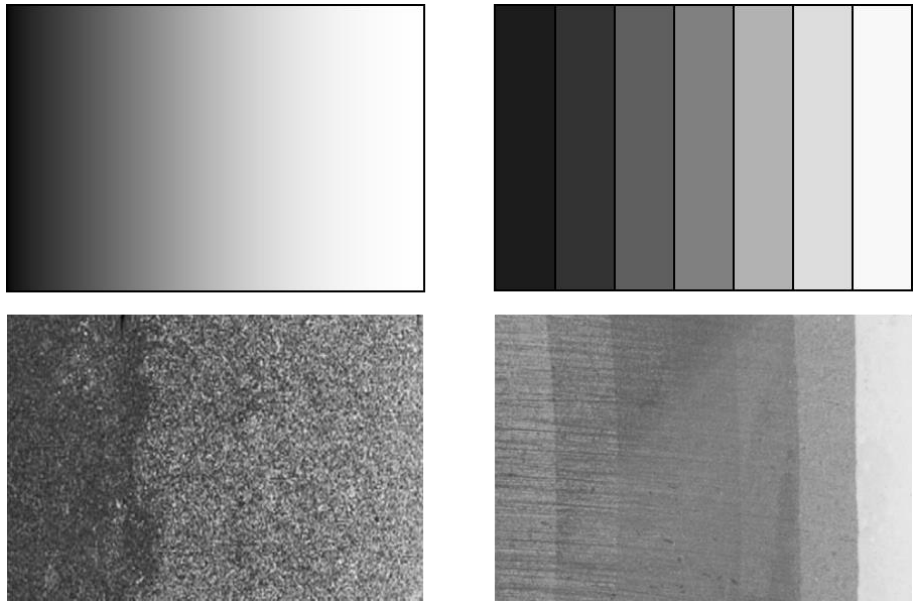

(a) Continuous-type (particulate type) [1] (b) Step-wised-type (layered type)

Figure 1.2 Two types of functionally graded materials

1.2 The origin of FGM

There are numerous examples of functionally graded structures in nature. They can be seen in the bio-tissues of plants and animals and also in the human body in places such as the bones and teeth. Bamboos, shells and coconut leaves are also examples of natural structures who derive their unique properties from functionally graded structures. Both bamboos and shells are very strong near their outside surface, and soft inside. Bamboo is known as an example of natural material that is lightweight, strong and elastic, which is due to nodes in the hollow which creates a hierarchy and step-wised structure. When a coconut leaf is blown by the wind, the section closest to the tip is tender and is able to move freely in any direction along with the wind, but the remaining part is very stiff and doesn't move. This type of structure is very suitable for its living environment.

Living creatures in nature are generally optimized with graded structures and tissues according to their living environments. Biomimetics or biomimicry is the applications of design features from nature to human-made products. Due to their unique potential, FGMs are one important aspect of biomimetics that can be used to improve man-made products.

FGMs were first proposed around 1984-85 by two researchers talking about their dream of developing spaceplanes; one was studying aeronautics and the other was studying advanced materials. The outer body of a spaceplane has to be exposed to very high temperatures and, therefore, needs to be resistant to severe conditions resulting from the temperature gap (about 1000 ℃) between the inside and the outside of the spaceplane. Since there

is no single material able to endure such conditions, the researchers devised the concept for FGMs in order to fabricate a spaceplane's body using materials with improved thermal resistance and mechanical properties by gradually changing (grading) its composition. They designed the body to use ceramic for the outer surface that is exposed to a high temperature environment and thermally conductive material for the inner surface.

This was the beginning of the FGM research activities. In 1987, their FGM research was accepted for a large project with the Ministry of Education and Science. During the period from 1987 to 1991, many researchers from universities, national laboratories and corporations participated in the research project entitled "Research on the Generic Technology of FGM Development for Thermal Stress Relaxation". They keenly discussed on methods of FGM development, and systemized the process such as material design, production and evaluation. Finally, a thermal stress relaxing material based on FGM principles was developed. Today, the concepts of FGMs was expanded and developed such that a large variety of materials have been developed [2].

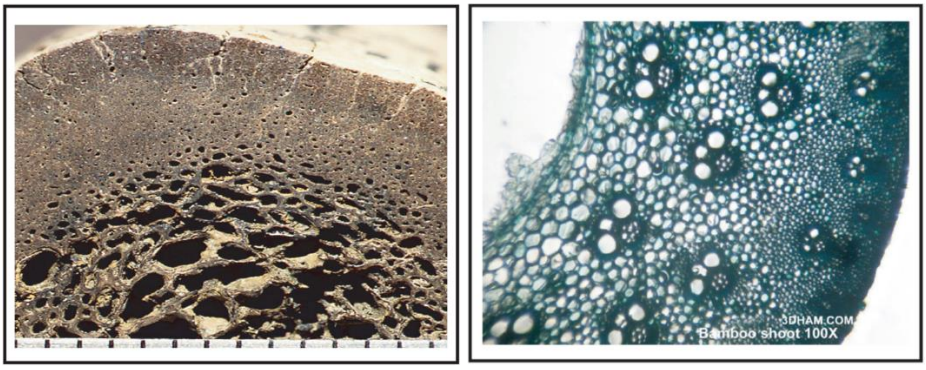

(a) Bone microstructure [3] (b) Bamboo microstructure [4]

Figure 1.3 Examples of naturally occurring FGMs

1.3 Motivation

Since prehistory, materials have played a crucial role in the development of our society and culture. In the twentieth century, the exploitation of base elements from the periodic table into various inorganic and organic compounds has made way for the development of advanced polymer, engineering alloys, and advanced structural ceramics, as shown in Figure 1.4. Furthermore, FGMs have been developed by combining advanced engineering materials in the form of particulates, fibers, whiskers, or platelets. In the continuous drive to improve structural performance, architecture of new materials using advanced experimental and numerical methods are required [5].

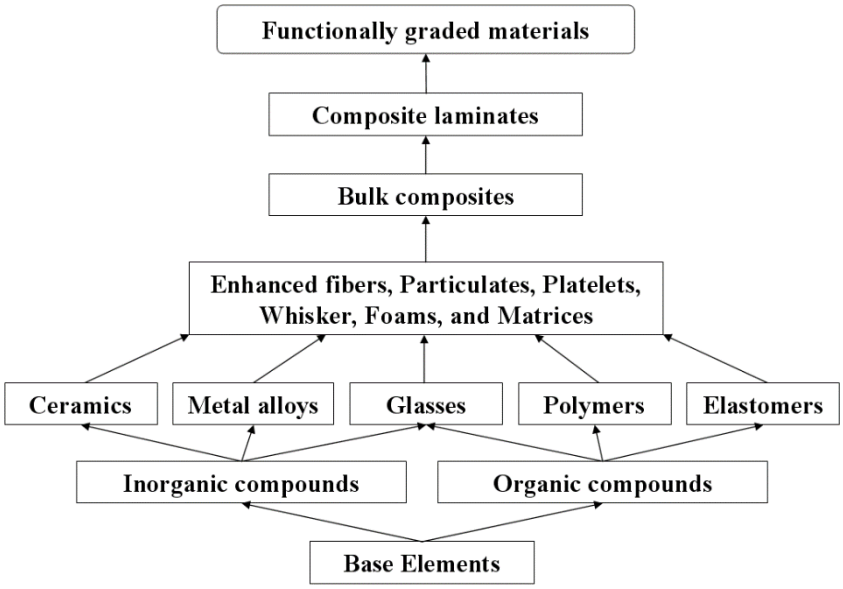

Figure 1.4 Illustration of our modern material hierarchy

Chapter 2. Objective

The research and development of industrial materials is a constantly evolving fields with new material improved materials being steadily developed. Nevertheless, modern machine parts are used in complicated conditions and severe environment, and require to be optimized simultaneously for a number of functions and environmental conditions.

Currently, in order to meet these needs, instead of a single material, composite material combining a suitable material for their needs is being developed rapidly. Composite materials have improved properties such as strength, stiffness, corrosion resistance, abrasion resistance, light weight, durability, heat resistance, sound insulation, etc. through the careful selection of the characteristics of the different materials.

However, these composite materials have disadvantages that the interface between the materials and components can be separated by the residual stress caused by differences of the coefficient of thermal expansion, lattice constant, physicochemical properties and others. To overcome this disadvantages and to improve bonding strength at the interface, Functionally Graded Materials (FGMs) have been developed [6-10].

In this study, a heat-resistant material is developed to increase the operating temperature as a strategy for increasing the thermal energy efficiency. To do so, the use of FGMs is introduced. As a heat shielding material, alumina was used because it maintains high strength at high

temperatures, and has good oxidation, corrosion, heat stability and thermal shock resistance capabilities. Nickel was used as the second material due to its high melting point and stiffness, which is used as the structural material of the FGM. Powder Metallurgy process and Pressureless Sintering Method were used for efficient and cost-efficient manufacturing of the FGM.

In order to produce FGM parts using specific materials and manufacturing methods, the process shown in Figure 2.1 is generally used [11]. Knowledge from both materials science and mechanical engineering science must be used to adequately develop FGMs. Therefore, the manufacturer should have a knowledge of both fields, otherwise it is difficult to develop FGM parts.

Therefore, in order to allow mechanical engineers without a strong background in material science to develop FGM parts, the goal of the present study is to develop a system making use of a material science database as shown in Figure 2.2. To make this system, the variables to be considered for the design and fabrication of FGMs from the materials science field should be input into the database, and the experiments required from the materials science field should be standardized, and the number of required experiment should be reduced.

Therefore, a precise measurement method for the porosity of the FGM, an estimation method for the material properties depending on porosity of the FGM and an estimation model that can predict the material properties with a minimal number experiments are suggested as basic research for the development of a database of materials science field in this study.

In order to confirm the reliability of the estimation model, the results of

analysis using estimated values from the estimation model were compared with measured values of fabricated FGMs.

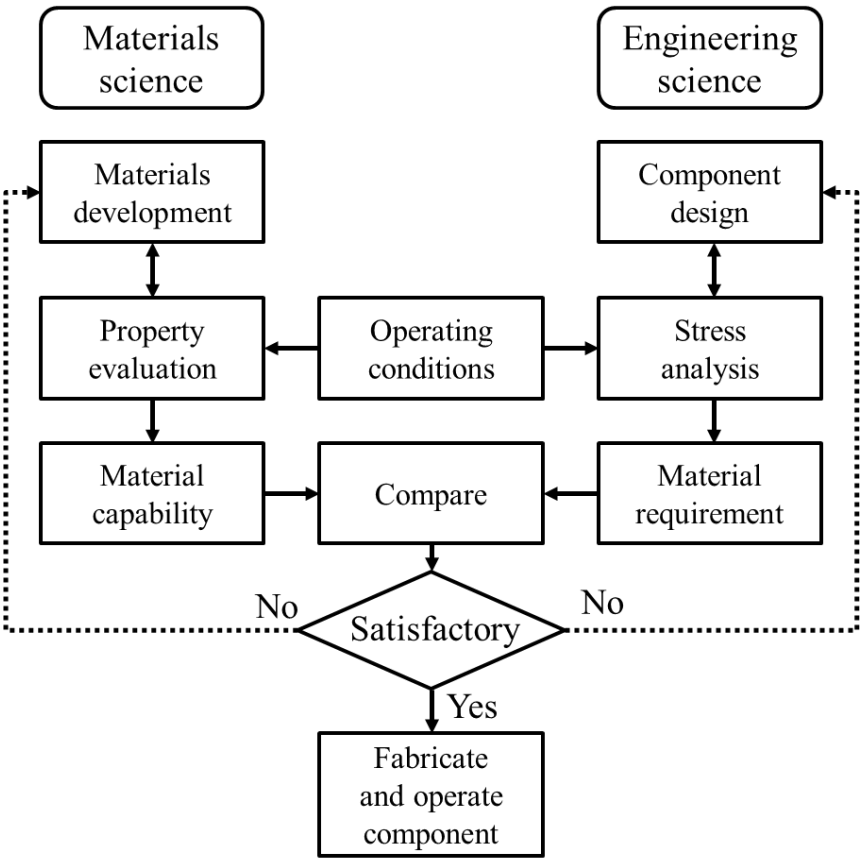

Figure 2.1 Present general process for the production of engineering parts of FGM forms

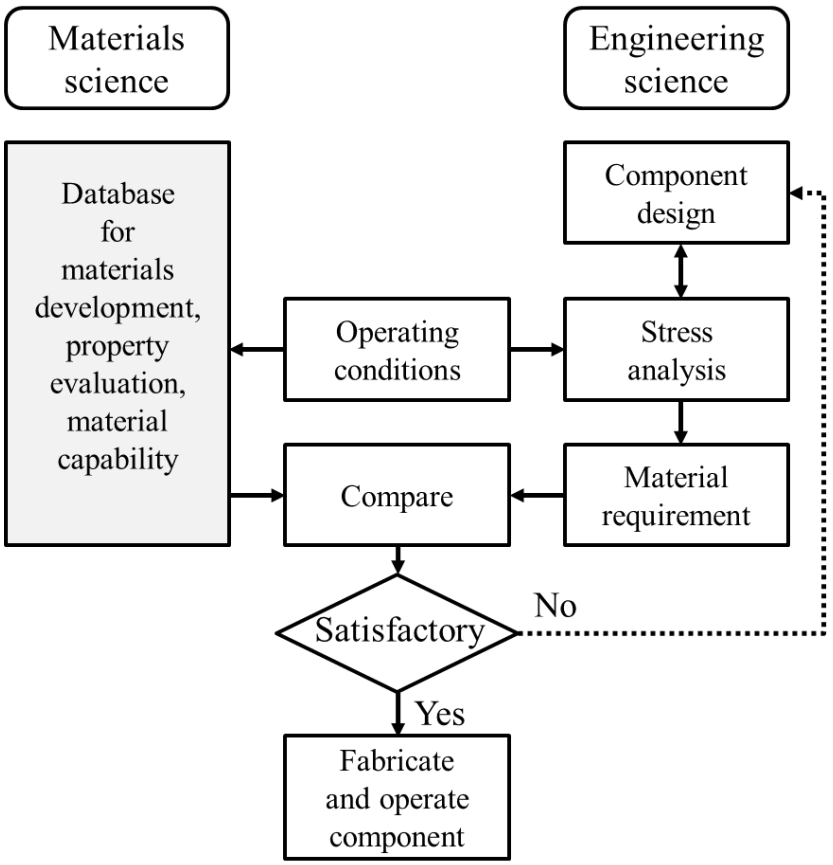

Figure 2.2 Process for the production of engineering parts of FGM forms with the aim in this study

Chapter 3. Literature reviews

3.1 Effective material properties of Functionally Graded Materials

A FGM is a composite material that is fabricated by mixing particles of two dissimilar material phases, for example, a metal and a ceramic. The constituent material phases are assumed to be perfectly bonded to one another. The result is a multi-phase structure which we consider to be isotropic in nature. Often, precise information about the size, shape and distribution of the particles may not be readily available and the effective modulus of the graded composite must be evaluated based only on the volume fraction distributions and the approximate shape of the dispersed phase. When presented with such a configuration, as is the case with functionally graded materials, it is necessary to estimate the effective material properties in order to perform numerical simulations of the thermo-elastic problems [12].

Several micromechanical models have been developed over the years to estimate the effective properties of two-phase FGMs. The simplest, and perhaps most common, is the classical linear law of mixtures [13], which assumes that the effective material property is the sum of each constituent's material property times its respective volume fraction. Another method is the modified rule of mixtures [14], which is an empirical formula that incorporates the interaction effects into the stress and strain values associated with each phase. Fan *et al*. [15] proposed a generalized law of mixtures which

can account for variations in volume fraction, grain shape and phase distribution that has agreed well with experiment. However, this method requires a number of input parameters, and in addition, is only suitable for determining effective elastic modulus and effective yield strengths.

These methods, Mori-Tanaka [16, 17] and self-consistent [18] schemes, each possess a complete set of estimates for the material properties used in this work. The Mori-Tanaka and self-consistent estimates, both derived from the solution of elasticity problems, do not require any additional information about the composite other than the relative volume fraction and material properties of the constituents.

As demonstrated by Reiter *et al*. [19] and Reiter and Dvorak [20] using finite element simulations of realistic microstructures, the Mori-Tanaka method works well for estimating the effective material properties in instances where the microstructure consists of clearly defined matrix and particulate phases. The Mori-Tanaka method assumes that the matrix phase is reinforced with spherical inclusions and accounts for the interplay of the elastic fields between neighboring particulate particles. In the following expressions, the matrix phase will be denoted by subscript 1 and the particulate phase by subscript 2. In this notation, K_1, μ_1, k_1, and α_1 denote the bulk modulus, the shear modulus, the thermal conductivity and the thermal expansion coefficient, respectively, and V_1 the volume fraction of the matrix phase. K_2, μ_2, k_2, α_2 and V_2 denote the corresponding material properties and the volume fraction of the particulate phase. It should be noted that for a two-phase FGM without voids, $V_1 + V_2 = 1$ at every location within the body.

The Mori-Tanaka estimates for the effective bulk modulus K and the effective shear modulus μ are [17]

$$\frac{K-K_1}{K_2-K_1}=\frac{V_2}{\left[1+(1-V_2)\dfrac{K_2-K_1}{K_1+\left(4\diagup 3\right)\mu_1}\right]} \tag{3.1}$$

and

$$\frac{\mu-\mu_1}{\mu_2-\mu_1}=\frac{V_2}{\left[1+(1-V_2)\dfrac{\mu_2-\mu_1}{\mu_1+f_1}\right]} \tag{3.2}$$

respectively, where the quantity f_1 is defined as

$$f_1=\frac{\mu_1(9K_1+8\mu_1)}{6(K_1+2\mu_1)} \tag{3.3}$$

Hatta and Taya [21] derived the effective thermal conductivity k of a composite with spherical particles embedded in a matrix as

$$\frac{k-k_1}{k_2-k_1}=\frac{V_2}{\left[1+(1-V_2)\dfrac{k_2-k_1}{3k_1}\right]} \tag{3.4}$$

The effective coefficient of thermal expansion α is determined by the correspondence relation [22] as

$$\frac{\alpha-\alpha_1}{\alpha_2-\alpha_1}=\frac{1\diagup K-1\diagup K_1}{1\diagup K_2-1\diagup K_1} \tag{3.5}$$

Once the effective properties of the bulk modulus, shear modulus, thermal conductivity and thermal expansion coefficient are obtained, determination of other material properties, such as the elastic modulus E, the Poisson's ratio ν, Lamé constant λ and stress temperature coefficient β are easily calculated using well-known relations of the theory of elasticity [23].

The self-consistent method draws its estimates through the solution of an elastic problem in which an ellipsoidal inclusion is embedded in a matrix possessing the effective material properties of the composite. The self-consistent scheme performs well in determining the effective properties of a two-phase composite in regions with a skeletal microstructure where there is no clearly defined matrix or particulate phase [19]. This is due, in part, because the self-consistent estimation scheme does not distinguish between the matrix and reinforcement phases. Thus, this scheme yields the same result for the modulus of a composite even when the material roles are reversed. Therefore, in the subsequent expressions, it is not important which of the material phases is denoted by a subscript 1 and which by subscript 2. The self-consistent estimate for the bulk modulus K and the shear modulus μ are given by the relationships [18]

$$\frac{\zeta}{K} = \frac{V_1}{K - K_2} + \frac{V_2}{K - K_1} \tag{3.6}$$

and

$$\frac{\tau}{\mu} = \frac{V_1}{\mu - \mu_2} + \frac{V_2}{\mu - \mu_1} \tag{3.7}$$

where

$$\zeta = 3 - 5\tau = \frac{K}{K + \left(4/3\right)\mu} \tag{3.8}$$

Equation (3.6) can be solved to obtain K after substitution of ζ from Equation (3.8),

$$K = \frac{1}{\left[\dfrac{V_1}{K_1 + \left(4/3\right)\mu} + \dfrac{V_2}{K_2 + \left(4/3\right)\mu}\right]} - \left(\frac{4}{3}\right)\mu \tag{3.9}$$

Equations (3.7), (3.8) and (3.9) yields the following quartic equation for the shear modulus μ

$$\frac{V_1 K_1}{K_1 + \left(4/3\right)\mu} + \frac{V_2 K_2}{K_2 + \left(4/3\right)\mu} + 5\left[\frac{V_1\mu_2}{\mu + \mu_2} + \frac{V_2\mu_1}{\mu + \mu_1}\right] + 2 = 0 \tag{3.10}$$

The self-consistent estimate of the effective thermal conductivity k is obtained by solving the quadratic equation [24]

$$\frac{V_1\left(k_1 - k\right)}{k_1 + 2k} + \frac{V_2\left(k_2 - k\right)}{k_2 + 2k} = 0 \tag{3.11}$$

The self-consistent estimate for the coefficient of thermal expansion α is

obtained by using the self-consistent estimate of the effective bulk modulus K in the correspondence relation Equation (3.5). It is worthwhile noting that the self-consistent scheme is harder to implement analytically than the Mori-Tanaka scheme since it requires the solution of a pair of implicit equations. However, numerical implementation of the self-consistent scheme can be performed without much difficulty due to readily available techniques for finding roots of polynomial equations.

3.2 Porous Material Characteristics

Contemporary elasticity theories for the properties of porous materials consider materials as composites whose porosity has zero material constants. At the same time it is necessary to consider the specific deformation of sintered materials from powders during production processing into articles. In contrast to cast or condensed materials that form as a result of solidification and crystallization, powder metallurgy materials relate to the class of consolidated materials that are prepared by forming, compaction, and sintering of fine powder particles. Therefore it is necessary to introduce a conceptual factor of their imperfection into rheological models of porous materials formed from. It emerges from the fundamental conditions of forming an imperfect powder material meso-structure intermediate between the micro- and macrostructure, as a result of random packing of powder particles in the initial stage of forming the material itself [25].

This approach to analyzing the elastic properties of sintered materials in relation to their porosity taking account of their meso-structural imperfection has been employed in [26]. Two of the most proven and verified methods for calculating the elasticity modulus of composite materials were chosen for the analysis: the self-congruent method developed in the fundamental work Mackenzie [27], Eshelby [28], Hill [29], and developed in the work of Skorokhod [30], Mori and Tanaka [16], Zhao, Tandon, and Weng [31], Budiansky and O'Connell [32]; the variation method of Hashin and Shtrikman [33]. From the results of analyzing the elasticity of porous materials [26] subsequently there was correction and refinement of approximation

dependences of these properties on the relative density of porous materials. Generalized dependences that have a simpler form [31] are used alongside expanded equations containing tensor components of Eshelby transformations. Elastic modulus of porous materials within the self-congruent theory for pores of spherical shape are determined by the equations

$$\frac{K}{K_0} = 1 - \frac{1-\rho}{1-\alpha_0\rho} \quad ; \quad \frac{\mu}{\mu_0} = 1 - \frac{1-\rho}{1-\beta_0\rho} \tag{3.12}$$

here K and K_0 are uniform compression modulus for porous material and the matrix that forms it; μ and μ_0 are porous material and matrix shear modulus, respectively; ρ is relative density;

$$\alpha_0 = \frac{1}{3} \cdot \frac{1+\nu_0}{1-\nu_0} \quad ; \quad \beta_0 = \frac{2}{15} \cdot \frac{4+5\nu_0}{1-\nu_0} \tag{3.13}$$

(ν_0 matrix Poisson's ratio [31]). Values of K and μ, calculated by Equation (3.12), agree with the results of calculation by the Hashin and Shtrikman variation method [33] for porous material.

The overall dependence for uniform compression and shear modulus on porosity in the self-congruent method for a random spatial pore distribution [27] is described by the equations

$$\frac{K}{K_0} = \left\{1 + \frac{(1-\rho)}{\rho} P_2\right\}^{-1} \quad ; \quad \frac{\mu}{\mu_0} = \left\{1 + \frac{(1-\rho)}{\rho} q_2\right\}^{-1} \tag{3.14}$$

For pores of needle-like shape randomly orientated in space:

$$P_2 = \frac{1}{3} \cdot \frac{5 - 4\nu_0}{1 - 2\nu_0} \quad ; \quad P_2 = \frac{8}{15} \cdot (5 - 3\nu_0) \tag{3.15}$$

For disk-shaped pores (the shape of coin) randomly orientated in space

$$P_2 = \frac{4}{3} \cdot \frac{1 - 4\nu_0^2}{1 - 2\nu_0} \cdot \frac{1}{\pi a} \quad ; \quad P_2 = \frac{8}{15} \cdot \frac{(1 - \nu_0)(5 - 3\nu_0)}{2 - \nu_0} \cdot \frac{1}{\pi a} \tag{3.16}$$

where $a = t/d$ (t is thickness, d is pore diameter). For cracks randomly orientated in space relationships (3.14) take the form

$$\frac{K}{K_0} = \left\{1 + \frac{16(1 - \nu_0^2)}{9(1 - 2\nu_0)}\eta\right\}^{-1} \quad ; \quad \frac{\mu}{\mu_0} = \left\{1 + \frac{32(1 - \nu_0)(5 - \nu_0)}{45(2 - \nu_0)}\eta\right\}^{-1} \tag{3.17}$$

here η is crack concentration [32]; $\eta = nd^3/V$, where V is volume and d is crack diameter. In variation method of Hashin and Shtrikman [33] the elasticity modulus of porous material are determined by relationships

$$\frac{K}{K_0} = \rho\left\{1 + (1 - \rho)\frac{3K_0}{4\mu_0}\right\}^{-1} \quad ; \quad \frac{\mu}{\mu_0} = \left\{1 + \frac{2}{3}(1 - \rho)\left(1 + \frac{10\mu_0}{9K + \mu_0}\right)\right\}^{-1} \tag{3.18}$$

After determining K and μ for porous material by known values of K_0 and μ_0 for compact material (it corresponds to the porous body matrix) by means of the relationships

$$\nu = \frac{1}{2} \cdot \frac{3K - 2\mu}{3K + \mu} \quad ; \quad E = 2(1+\nu)\mu \tag{3.19}$$

Poisson's ratio ν and elastic modulus (tensile modulus) E are determined for isotropic porous material.

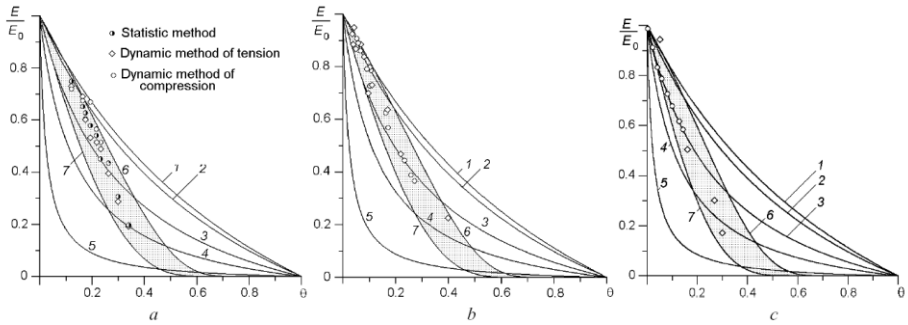

Figure 3.1 Dependence of the ratio of elastic modulus of porous E and pore-free E_0 nickel (a), iron (b), and boron carbide (c) on porosity θ. Curves were calculated by the self-congruent method for pores of spherical (1), needle-like (2) and disk shape with a thickness to diameter ratio of a = 0.1 (3), 0.05 (4), and 0.01 (5). The hatched fork of curves corresponds to approximation relationship (9) within the perfect (6) and imperfect material with an imperfection coefficient m = 0.65 (7). Points are experimental data.

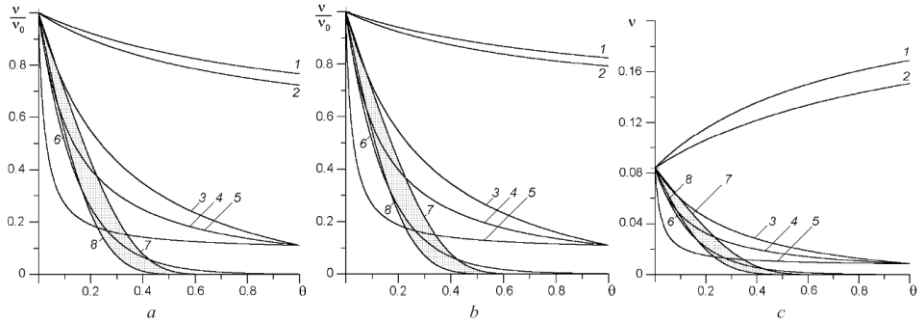

Figure 3.2 Dependence of Poisson's ratio ν for nickel (a), iron (b), and boron carbide (c) on porosity. Curves were calculated by the self-congruent method for pores of spherical (1), needle-like (2) and disk shape with a thickness to diameter ratio of a = 0.1 (3), 0.05 (4), and 0.01 (5). Curve 6 corresponds to the empirical relationship $\nu = \nu_0 \exp(-6.8\theta)$. The hatched fork of curves corresponds to approximation relationship (8) within the perfect (7) and imperfect material with an imperfection coefficient m = 0.65 (8).

Results of computer calculations with respect to elastic modulus and Poisson's ratio for a porous nickel (E_0 = 194 GPa, ν_0 = 0.32), iron (E_0 = 211 GPa , ν_0 = 0.28), and boron carbide B_4C (E_0 = 465.6 GPa, ν_0 = 0.084) together with experimental data for porous nickel [34], iron [35], and boron carbide [36, 37] are given in Figure 3.1 and Figure 3.2 [40]. There is a general tendency of a regular reduction in the value of E/E_0 with an increase in porosity. There is no general tendency for Poisson's ratio and a recently established empirical dependence (curve 6) that is expressed by the equation $\nu = \nu_0 \exp(-6.8\theta)$ [38], has the same nature as curves 3-5. These points to a change in pore shape in relation to overall porosity and also presence in the structure of actual porous material of two-dimensional defects in the form of meso-element boundaries [25]. In order to describe the elastic behavior of actual porous material with mechanical loads it is necessary to introduce a quantitative characteristic of the degree of structural imperfection connected with the presence of meso-defects. Therefore, as in the case of the ductility of porous materials [39] it is desirable to select a phenomenological coefficient m as the imperfection index of material elastic behavior.

None of the theoretical dependences of elastic properties on porosity for definite pore shape describe the elastic behavior of porous material (Figure 3.1 and Figure 3.2). Therefore computer calculations have been performed for the effective elastic modulus of porous materials using approximation equations in order to describe the dependence of these properties on porosity. Here it was assumed that with low porosity approximation should be as close as possible to both a theoretical equation and experimental data, but with high

porosity calculated dependences should be close to experimental data. As a result of this approximation equations for Poisson's ratio and shear modulus have been suggested

$$\frac{\nu}{\nu_0} = \rho^{\frac{3}{(1-m^2)\rho}} = \rho\varpi \qquad ; \qquad \frac{\mu}{\mu_0} = \rho^{\frac{c-(1-m^2)\rho}{(1-m^2)\rho}} \tag{3.20}$$

Elastic modulus E and uniform compression modulus K were determined taking account of Equation (3.19)

$$E = 2\mu_0(1+\nu_0\rho\varpi)\left(\frac{\mu}{\mu_0}\right) \qquad ; \qquad K = \frac{E}{3(1-2\nu)} \tag{3.21}$$

The value of c correlates with the Poisson's ratio, c = 2 for metallic materials (nickel, iron), and c = 2.5 for ceramic materials (boron carbide). These approximation relationships, shown as the hatched forks of curves 6-7 (Figure 3.1) and 7-8 (Figure 3.2) for perfect (m = 0) and imperfect (m = 0.65) materials, point to the conformity of the suggested description with experimental data. Curves 1 (Figure 3.1 and Figure 3.2) calculated by the self-congruent method coincide with curves calculated by the Hashin and Shtrikman variation method.

3.3 Porosity of composite fabricated by Pressureless Sintering Method

Various approaches based on the bulk (particulate processing), pre-form processing, layer processing and melt processing are used to fabricate the FGMs. Especially, the particulate processing used heat such as pressureless sintering, hot pressing, and hot isostatic pressing is general. However, it have been reported that their methods are caused thermal residual stress in the interface of other materials due to differential shrinkage and generated defect such as pore, micro crack, and etc.. Especially composite fabricated by pressureless sintering has many pores [41-45]. This pore causes variation of material properties. Therefore the porosity becomes important parameter in design of FGM fabricated by pressureless sintering.

Shabana *et al*. published paper for porosity of FGM joined by Nickel and Alumina in International Journal of Solid and Structures; Volume 43 [48]. In the paper, pressureless sintering of particulate processing is used to fabricate layered FGM, and initial- and final-porosity were measured as shown in Figure 3.3.

Also Bruck & Pines proposed two prediction models for porosity of composite in Acta MATERIALIA journals [46, 47]. First theoretical porosity model was assumed that all porosity is associated with the matrix material as shown in Figure 3.4.

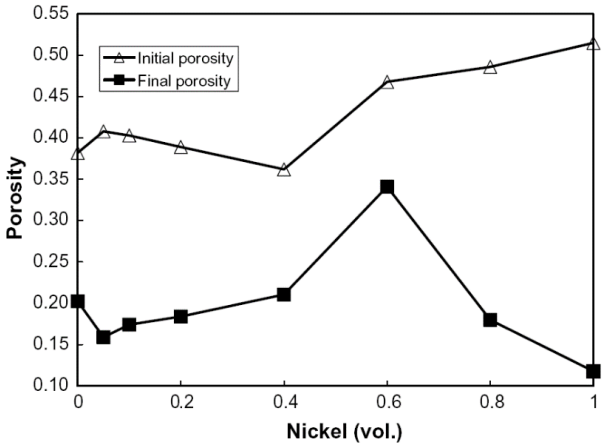

Figure 3.3 Variation of initial and final porosity with the nickel compositions in the paper [48]

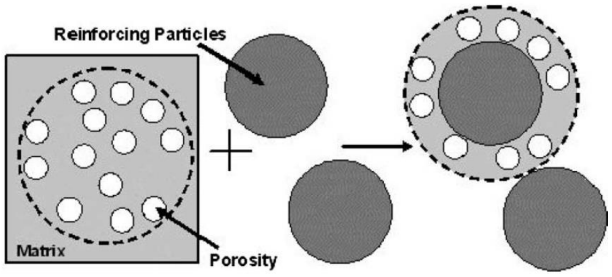

Figure 3.4 First theoretical porosity model, assuming all porosity is associated with the matrix [46]

In first model, the particle reinforcement occupies a constant volume fraction of the composite before and after sintering, and all porosity is a result of the incomplete packing of the smaller particles in the matrix material. Therefore, these calculations of porosity are based upon the volume fraction of the matrix material present in a particular composition.

The final porosity volume fraction is calculated by Equation (3.22), and then υ^* is determined by Equation (3.23), as follows:

$$P_{\mathrm{f}} = 1 - \upsilon_{\mathrm{matrix_f}} \left(1 + \upsilon^*\right) \tag{3.22}$$

$$\upsilon^* = \left\{ \begin{array}{l} \dfrac{1-\upsilon_{\mathrm{Ni}}}{\upsilon_{\mathrm{Ni}}} \text{ for Ni matrix} \\ \dfrac{\upsilon_{\mathrm{Ni}}}{1-\upsilon_{\mathrm{Ni}}} \text{ for } Al_2O_3 \text{ matrix} \end{array} \right\} \tag{3.23}$$

where the final porosity values, P_{f}, the ideal volume fractions of nickel, υ_{Ni}, and the finial volume fraction of the matrix material, $\upsilon_{\mathrm{matrix_f}}$.

Second theoretical porosity model is assumed that porosity associated with matrix and particles as shown in Figure 3.5. This calculation of porosity is completed by scaling the volume fraction of the matrix based upon the amount of porosity associated with the pure matrix. Hence, the ratio of the initial porosity to the initial volume fraction of the pure matrix material is used to convert the fraction of matrix material into the amount of porosity

associated with the matrix. This conversion assumes the matrix material behaves the same in each composite as it does when there is no reinforcing phase present. Therefore, the volume fraction of porosity associated with the matrix, $\left(\upsilon_{\text{porosity}}\right)_{\text{matrix}}$, is given by

$$\frac{\left(\upsilon_{\text{porosity}}\right)_{\text{matrix}}}{\upsilon_{\text{matrix}}} = \frac{P_{\text{pure}}}{1-P_{\text{pure}}} = \text{constant} \tag{3.24}$$

In Equation (3.24), the amount of porosity due to the matrix material is computed using the known volume fraction of the matrix material, υ_{matrix}, and the known ratio of porosity to matrix material. The term P_{pure} is the amount of porosity in the pure matrix material. Following the calculation of the porosity in the matrix, the porosity associated with the presence of the reinforcing phase, $\left(\upsilon_{\text{porosity}}\right)_{\text{particle}}$, is simply the difference between the whole porosity in the material and the partial volume fraction of the porosity due to the matrix phase such as Equation (3.25).

$$\left(\upsilon_{\text{porosity}}\right)_{\text{particle}} = P - \left(\upsilon_{\text{porosity}}\right)_{\text{matrix}} \tag{3.25}$$

Finally the final porosity of Equation (3.27) can be determined from the porosity-matrix material relationship shown in Equation (3.24) using the final

porosity of the pure materials and the relations for $\left(\upsilon_{\text{porosity}}\right)_{\text{matrix}}$ and $\left(\upsilon_{\text{porosity}}\right)_{\text{particle}}$ employed in Equation (3.26) as follows.

$$\frac{\left(\upsilon_{\text{porosity}}\right)_{\text{particle}_{\text{f}}}}{\upsilon_{\text{matrix}_{\text{f}}}} = \frac{\left(\upsilon_{\text{porosity}}\right)_{\text{particle}_{\text{i}}}}{\upsilon_{\text{matrix}_{\text{i}}}} \tag{3.26}$$

$$P_{\text{f}} = \upsilon_{\text{matrix}_{\text{f}}}\left[\left(\frac{P_{\text{pure}}}{1-P_{\text{pure}}}\right)_{\text{f}} + \frac{\left(\upsilon_{\text{porosity}}\right)_{\text{particle}_{\text{i}}}}{\upsilon_{\text{matrix}_{\text{i}}}}\right] \tag{3.27}$$

The experimental porosity measurements are shown in Figure 3.6, along with the results from both of the models described for the theoretical porosity. As can be seen, the theoretical estimates for the final porosity are lower than measured values. The differences between the estimated and measured porosities are larger for the nickel-rich compositions, especially for the 60 vol.% Ni composite, it show 29% error. The second theoretical model is more approximate for measured porosity volume fraction than the first theoretical model.

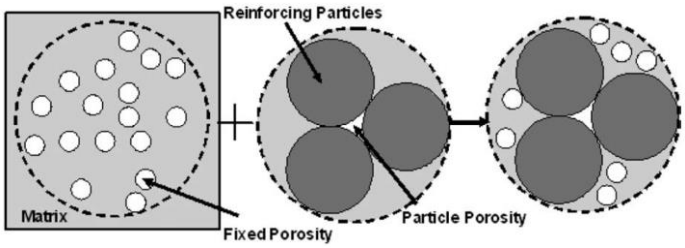

Figure 3.5 Second porosity model attributing an amount of porosity to the matrix equivalent to that of the pure material, and all remaining porosity associated with the particles [46]

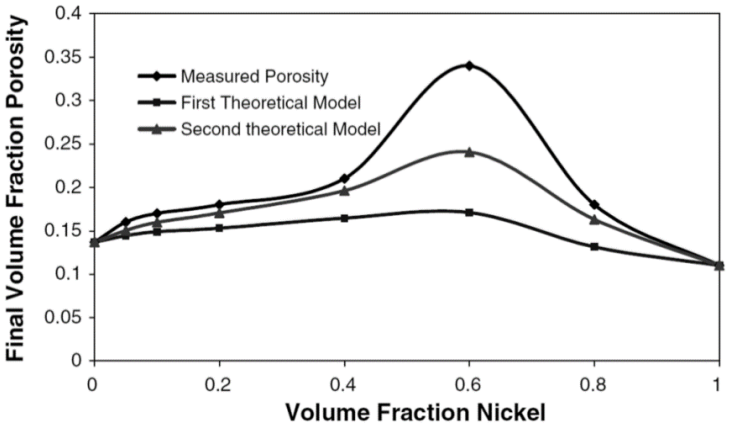

Figure 3.6 Plot of the measured and predicted values from each of the models for the final porosity [46]

3.4 Analysis of FGM behavior

The Modeling and thermal stress analysis of FGMs have been studied strongly and actively.

Markwort *et al*. [49] described the modeling studies relative to FGMs. They included two aspects of the modeling procedure: models for microstructure-dependent thermo-physical properties, and models for the design, processing, and performance of FGMs.

Fuchiyama and Noda [50] developed computer programs that analyze the transient heat transfer and the transient thermal stress of FGM plates, composed of ZrO_2 and Ti-6Al-4V, by the finite element method.

Ravichandran [51] examined a one-dimensional calculation of thermal residual stresses, arising from the fabrication of an Al_20_3/Ni FGM. Several functional forms of gradation of constituents were examined to arrive at the optimum profile giving the minimum residual stress level. The effects of temperature dependent elastic and thermal expansion characteristics of constituents on residual stress were found to be small.

Aboudi *et al*. [52, 53] extended a micromechanical theory for the thermo-elastic response of functionally graded composites with nonuniform fiber spacing in the through-thickness direction to enable analysis of material architectures characterized by arbitrarily nonuniform fiber spacing in two directions and to include the inelastic and temperature-dependent response of constituent phases.

Aboudi *et al*. [54] also employed the higher-order theory for the response of a FGM plate subjected to a through-thickness thermal gradient to optimize

the composite's microstructure. In addition, Aboudi *et al*. [55] developed the full generalization of the Cartesian coordinate-based higher-order theory for FGMs. The theoretical framework was based on volumetric averaging of the various field quantities, together with imposition of boundary and interfacial conditions in an average sense between the sub-volumes used to characterize the composite's functionally graded microstructure.

Reddy and Chin [56] studied the dynamic thermo-elastic response of FGM cylinders and plates. The three-dimensional heat conduction and the memo-elastic equations were solved and coupled in the formulation, and a finite element model of the formulation was developed.

Reddy and Cheng [57] analyzed three-dimensional thermo-mechanical deformations of a simply supported FGM rectangular plate by using an asymptotic method. The locally effective material properties were estimated by the Mori-Tanaka scheme. The temperature, displacements and stresses of the plate were computed for various volume fractions.

Reddy [58] presented the theoretical formulation, Navier's solutions of rectangular plates and finite element models based on the third-order shear deformation plate theory for FGM plates. The formulation accounted for the thermo-mechanical coupling, time dependency and the von Karman geometric nonlinearity.

Cheng and Batra [59] obtained a new solution in closed form for the thermo-mechanical deformations of an isotopic linear thermo-elastic FGM elliptic plate rigidly clamped at the edges. The method of asymptotic expansion was used to study three-dimensional mechanical deformations,

and the deformations due to thermal loads were straightforwardly found. In this work, it was found that the through-thickness distributions of the in-plane displacements and transverse shear stresses in a FGM plate did not agree with those assumed in classical and shear deformation plate theories.

Vel and Batra [60] obtained an exact solution for three-dimensional deformations of a simply supported Al/SiC functionally graded rectangular plate subjected to mechanical and thermal loads on its top and/or bottom surfaces. The effective material properties at a point were estimated by either the Mori-Tanaka or the self-consistent scheme.

Vel and Batra [61] also presented an analytical solution for three-dimensional thermo-mechanical deformations of a sm1ply supported FGM rectangular plate subjected to time-dependent loads on its top and/or bottom surfaces. The transient temperature, displacements, and thermal stresses at several critical locations were investigated for plates subjected to either time-dependent temperature or heat flux prescribed on the top surface. Fur1her,

Vel and Batra [62] analyzed a three-dimensional exact solution for free and force vibration of simply supported FGM rectangular plates. In this study, suitable displacement functions that identically satisfy boundary conditions were used to reduce equations governing steady state vibrations of a plate to a set of coupled ordinary differential equations, which were then solved by employing the power series method.

Qian *et al*. [63] investigated the static deformations and free and forced vibrations of a thick rectangular FGM plate by using a higher-order shear

and normal deformable plate theory and a meshless local Petrov-Galerkin method. The response of the plate to impulse loads was computed for different volume fractions.

Cho and Oden [64] presented thermal-stress characteristics of FGM beams using the Crank-Nicolson-Galerkin scheme. The effects of the material variation through the thickness and the size of the FGM layer inserted between ceramic (Al_2O_3) and metal (Ni) layers were studied using the finite element method.

Cho and Ha [65] estimated the thermo-mechanical properties and responses of dual-phase FGMs by conventional averaging approaches, such as rules of mixtures, mean-field micromechanics, and so on. They numerically investigated three representatives averaging estimation methods, the linear and modified rules of mixtures and the Wakashima-Tsukamoto estimate, by comparing with the finite element discretization approach utilizing rectangular cells.

Wang and Tian [66] developed a finite element/finite difference method to solve the time-dependent temperature field in non-homogeneous materials such as functionally graded materials. The method used the finite element space discretization to obtain a first-order system of differential equations, which was solved by employing finite difference scheme to resolve the time-dependent response.

Gasik [67] discussed the main principles of FGM structure modeling, justification of several model approaches, W/Cu FGM properties evaluation with respect to their application in a fusion reactor.

The micromechanical and nano analysis of FGMs have been researched in many engineering fields.

Rodriguez-Castro *et al*. [68] investigated the microstructure and mechanical behavior including tensile and fracture properties of a Al A359/SiC_p FGM processed by centrifugal casting.

Tsukamoto [69] presented an analytical description of thermal stress states in a FGM plate subjected to through-thickness heat flow by combining micromechanical with macro-mechanical approaches.

Kumar and Wang [70] performed nano-indentation experiments on various sintered bio-ceramic powders and bio-ceramic FGM coatings with a berkovich indenter to establish an improved method for determining hardness and elastic modulus from load and displacement data.

The failure and fracture analyses of FGMs have been investigated in many studies.

Bao and Wang [71] analyzed the multiple cracking in functionally graded ceramic/metal coatings. To guide the design of coating gradation so that cracking damage could be minimized, a fracture mechanics study was made of the crack driving force for multiple cracks. Systematic finite element calculations were made for the energy release rate of the cracks in the coating as determined by the coating gradation, crack length and the crack density; both mechanical and thermal loads were considered.

Jin and Batra [72] studied the effects of loading conditions, specimen size and metal particle size on the crack growth resistance curve(R-curve) and residual strength of a FGM based on the crack-bridging concept. It was

found that the FGM exhibited strong R-curve behavior when a crack grew from the ceramic-rich region toward the metal-rich region and the residual strength of the FGM with an edge crack at the ceramic side was notch-insensitive.

Butcher *et al*. [73] measured elastic modulus in FGM. Elastic modulus gradients occurred over length scales suitable for experimental mechanics investigations using optical interferometry. The optical measurements were used to extract fracture parameters based on the prevailing understanding of the crack tip behavior in FGMs.

Bruck and Gershon [74] utilized a 3-D model to predict the residual stress distribution in a joint composed of a nickel and alumina plate joined by a 60 vol.% Ni particulate reinforced composite interlayer.

Becker Jr. *et al*. [75] studied the crack path and fracture criteria with application to homogeneous and FGMs.

Cho and Choi [76] explored the suitability of the yield-stress-calibrated objective function for maximizing the yield strength of heat-resisting FGMs. They used two-level finite element meshes, coarse mesh for the volume fraction field and fine mesh for the thermo-elastic deformation field, in order to resolve the quality-time dilemma effectively.

Ma *et al*. [77] investigated the electro-elastic behavior of a Griffith crack in a functionally graded piezoelectric strip.

Zhang and Paulino [78] investigated dynamic fai1ure processes in homogeneous and FGMs. The failure criterion was incorporated in the cohesive zone model using both a finite cohesive strength and work to

fracture in the material description.

Zhang *et al*. [79] analyzed the thermo-mechanical behaviors and the distribution of residua1 stresses in ZrO_2/NiCoCrAlY FGM coatings due to thermal spraying by thermo-mechanical finite element analysis. They also discussed the residual stress-induced failure model of coatings.

Chapter 4. Experimental Procedure

In this study, a green-body of a Ni / Al_2O_3 FGM was fabricated using Powder Metallurgy technique and was sintered using the Pressureless Sintering Method. The nickel selected for this study has strong oxidation resistance properties at low temperatures, can be forged, and is a rich material for ductility. Nickel is a metal that is widely used as a construction material. In addition, alumina provides excellent heat resistance, wear resistance, electrical insulation properties, and chemical resistance. Alumina also is easy to sinter, and is a strong material. Thus it is applied in various fields.

In addition to the characteristics described above, nickel and alumina are used in this study for the following additional reasons: nickel has a high melting point and is easily joined with ceramics having a high melting point. In addition, alumina features a relatively high thermal expansion coefficient for a ceramic material. Therefore, alumina is suitable for bonding with a metal that has a relatively higher thermal expansion coefficient than do normal ceramics. Because of these properties, many studies of bonding between nickel and alumina have been performed [6-10].

However, the CTE of nickel is 13.1E-6/℃, and the CTE of alumina is 5.5E-6/℃ [80]. The difference of CTE between nickel and alumina is still high. Thus, it is difficult to fabricate a complete Ni / Al_2O_3 FGM. In addition, the generation ratio of pores is higher when manufacturing a FGM using the

Pressureless Sintering Method. Generated pores also decrease the strength and change the outer shape of the FGM. Furthermore, other problems may occur, including the difficulty of the mixed powder production generated by the density difference between nickel and alumina [9, 11, 12].

For these reasons, Bruck *et al*. [48] made a crack-free Ni / Al_2O_3 FGM using a 60 vol.% nickel layer instead of 100 vol.% nickel layer. In addition, Lee *et al*. [9, 11, 12] fabricated a crack-free Ni / Al_2O_3 FGM using a weight fraction, however the outer shape of the fabricated FGM was significantly deformed.

In this study, many parts of the manufacturing process were improved based on previous studies. Finally, a crack-free Ni / Al_2O_3 FGM was fabricated that provided a better outer shape than the previous FGMs provided.

4.1 Layer design of a FGM

The composition of each layer of FGM was designed to change linearly 10 vol.% interval, and the volume of each layer was planned to be kept constant. However, the volume of each layer of FGM was unable to be determined. Therefore, simulation for determining the appropriate volume was performed using the finite element method.

At the start of the research, a "Voigt model (mixture rule)" was applied to make the gradient because it has been widely used in the modeling of FGMs [41]. A material having two components, denoted as A and B, is considered. Let P_A and P_B be the values of some particular property for pure A and pure B, respectively, and let their respective volume fractions be V_A and V_B, where $V_B = 1 - V_A$ assuming that the material is 100% dense and ideal joining and dispersion between the two materials.

$$P_c = V_A \cdot P_A + V_B \cdot P_B \tag{4.1}$$

This Voigt model was applied to calculate density of each graded layer, and thickness of FGM layers is decided by calculated density. Material properties of the Ni / Al_2O_3 FGM were calculated as shown in Table 4.1. Here, values used as material properties for pure alumina and pure nickel are quoted from the literature [80].

The thermal residual stresses of the FGM were computed using the finite element method (FEM): ANSYS APDL.

The thermal strain, ε_T, of each isotropic layer was determined from

$$\{\varepsilon_T\} = \{\alpha \Delta T\} \tag{4.2}$$

where α is the CTE of the material and ΔT is the temperature change. The thermal stress, σ_T, was calculated from the thermal strain,

$$\{\sigma_T\} = [D]\{\varepsilon_T\} \tag{4.3}$$

where $[D]$ is the stress-strain matrix derived from Poisson's ratio (v) of the materials and the one-dimensional elastic modulus (E) [81].

If the trivial relations $\tau_{r\theta} = 0$ and $\tau_{\theta z} = 0$ are omitted, the most general axisymmetric form of Equation (4.3) for the coordinates shown in Figure 4.1 is as follows [82] :

$$\begin{Bmatrix} \sigma_r \\ \sigma_\theta \\ \sigma_z \\ \tau_{zr} \end{Bmatrix} = \frac{(1-v)E}{(1+v)(1-2v)} \times \begin{bmatrix} 1 & \frac{v}{1-v} & \frac{v}{1-v} & 0 \\ \frac{v}{1-v} & 1 & \frac{v}{1-v} & 0 \\ \frac{v}{1-v} & \frac{v}{1-v} & 1 & 0 \\ 0 & 0 & 0 & \frac{1-2v}{2(1-v)} \end{bmatrix} \begin{Bmatrix} \propto \Delta T \\ \propto \Delta T \\ \propto \Delta T \\ 0 \end{Bmatrix} \tag{4.4}$$

For finite element analysis, a two-dimensional, four-node plane element (PLANE42) was used in the ANSYS APDL. The two-dimensional axisymmetric model was meshed using 0.1 mm elements.

Figure 4.2 shows a schematic model of 2D from 3D (a) and the elements and boundary conditions of the FEM model (b) used for the finite element analysis.

The temperature conditions are a cooling condition from 1350℃ to 25℃. Thermal residual stress caused by the difference of the thermal expansion coefficient between properties of each layer of FGM was computed.

In the analysis result, when the volume of each layer of the FGM was 1.0 cc, the 1st principal stress was higher than the failure strength at the 20 vol.% Ni / 80 vol.% Al_2O_3 layer, as shown in Figure 4.2. Meanwhile, when the volume of each layer of the FGM was reduced to 0.5 cc, the 1st principal stress was lower than the failure strength, as shown in Figure 4.3.

Finally, the volume of each layer of the FGM to be applied to this study was determined as 0.5 cc. Then, the weight of each material to be inserted into each graded layer of the FGM was calculated as shown in Table 4.2.

Table 4.1 Material properties of each layer of the FGM calculated by Voigt model (assuming that the material is 100% dense)

Layer	Composition (Volume %)	Volume fraction		Elastic modulus (MPa)	Poisson's ratio	CTE (㎛/m℃)	Failure strength (MPa)
		Ni	Al_2O_3				
1	100% Al_2O_3	0.00	1.00	370000	0.220	5.50	300.0
2	10% Ni / 90% Al_2O_3	0.10	0.90	353700	0.229	6.26	301.7
3	20% Ni / 80% Al_2O_3	0.20	0.80	337400	0.238	7.02	303.4
4	30% Ni / 70% Al_2O_3	0.30	0.70	321100	0.247	7.78	305.1
5	40% Ni / 60% Al_2O_3	0.40	0.60	304800	0.256	8.54	306.8
6	50% Ni / 50% Al_2O_3	0.50	0.50	288500	0.265	9.30	308.5
7	60% Ni / 40% Al_2O_3	0.60	0.40	272200	0.274	10.06	310.2
8	70% Ni / 30% Al_2O_3	0.70	0.30	255900	0.283	10.82	311.9
9	80% Ni / 20% Al_2O_3	0.80	0.20	239600	0.292	11.58	313.6
10	90% Ni / 10% Al_2O_3	0.90	0.10	223300	0.301	12.34	315.3
11	100% Ni	1.00	0.00	207000	0.310	13.10	317.0

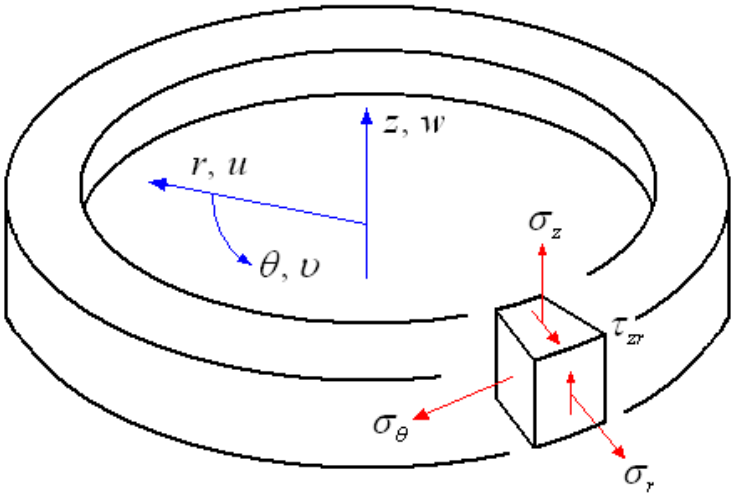

Figure 4.1 An axisymmetric finite element, showing stresses associated with axisymmetric loading

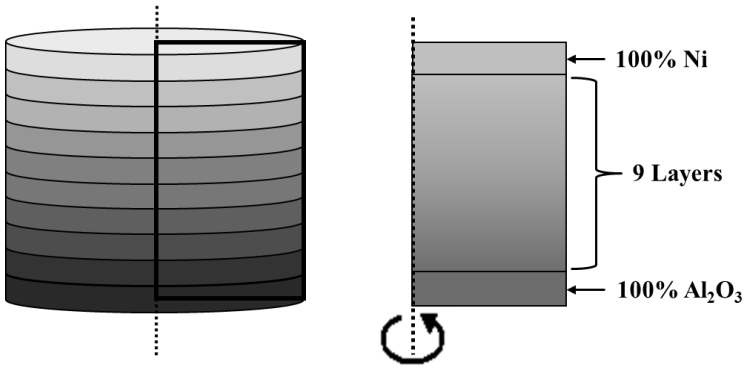

(a)

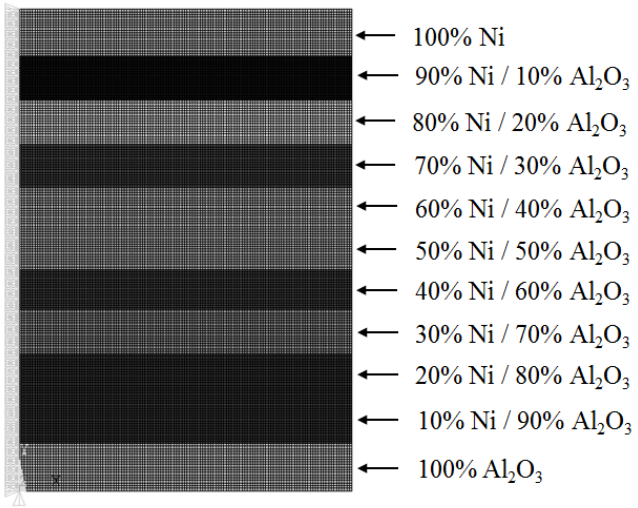

(b)

Figure 4.2 (a) a schematic model of 2D from 3D, (b) the elements and boundary conditions of FEM model

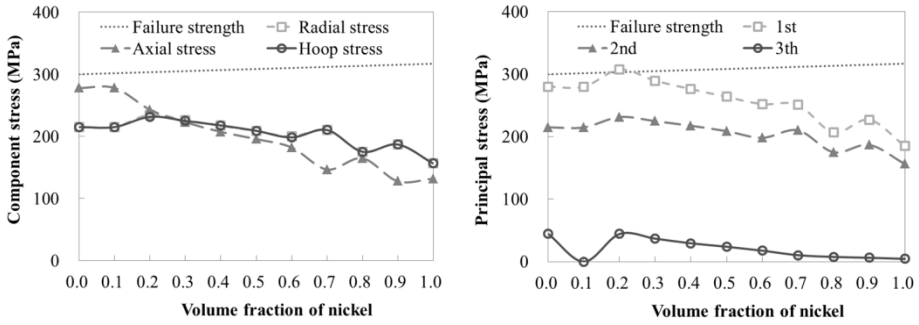

(a) The volume of each layer =1.0 cc

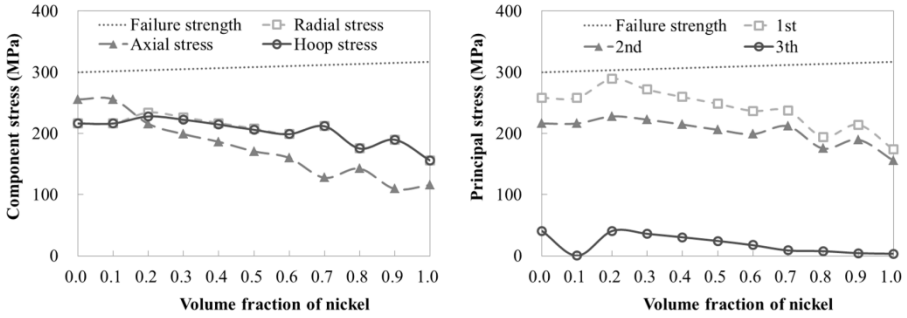

(b) The volume of each layer =0.5 cc

Figure 4.3 Analysis results of thermal residual stress

Table 4.2 Calculated weight to be inserted into each layer of the FGM when the volume of each layer is 0.5 cc

Layer	Composition (Volume %)	Volume fraction		Theoretical true density (g/cc)	Volume (cc)	Weight (g)	
		Ni	Al_2O_3			Ni	Al_2O_3
1	100% Al_2O_3	0.00	1.00	3.960	0.50	0.000	1.980
2	10% Ni / 90% Al_2O_3	0.10	0.90	4.454	0.50	0.445	1.782
3	20% Ni / 80% Al_2O_3	0.20	0.80	4.948	0.50	0.890	1.584
4	30% Ni / 70% Al_2O_3	0.30	0.70	5.442	0.50	1.335	1.386
5	40% Ni / 60% Al_2O_3	0.40	0.60	5.936	0.50	1.780	1.188
6	50% Ni / 50% Al_2O_3	0.50	0.50	6.430	0.50	2.225	0.990
7	60% Ni / 40% Al_2O_3	0.60	0.40	6.924	0.50	2.670	0.792
8	70% Ni / 30% Al_2O_3	0.70	0.30	7.418	0.50	3.115	0.594
9	80% Ni / 20% Al_2O_3	0.80	0.20	7.912	0.50	3.560	0.396
10	90% Ni / 10% Al_2O_3	0.90	0.10	8.406	0.50	4.005	0.198
11	100% Ni	1.00	0.00	8.900	0.50	4.450	0.000

4.2 Fabrication of specimen

4.2.1 Powder processing

The fabrication process used to produce the specimen in the study proceeded in the order of mixing the powder, molding the green-body, and sintering the green-body.

The powders have an average particle size of 3 ㎛ (Sigma Aldrich, Co., Ltd., Figure 4.5) for nickel, and 0.16 ㎛ (TM-DAR, TAIMICRON Co., Ltd, Figure 4.4) and 1.0 ㎛ (AL003PB, KOJUNDO KOREA Co., Ltd) for alumina. According to the manufacturer's report [83], TM-DAR is the alpha type on the crystalline form. The average of particle size for TM-DAR is 0.1 ㎛. Its green-body density was 2.3 g/㎤ when pressure was 98 MPa in uniaxial compression, and its sintered-body density was 3.96 g/㎤ when sintering time was 1 hour at 1350℃ in air.

Nickel and alumina particles were mixed using solvent (99.9% ethanol) in a 1000 mL flask, according to Table 4.2 and as shown in Figure 4.6.

The powders were mixed efficiently with simultaneous use of an evaporator and sonicator of bath type to prevent segregation caused by the density differences between Ni and Al_2O_3 powders (Ni: 8.88 g/cc, Al_2O_3: 3.96 g/cc), as shown in Figure 4.7. Mixed and dried powder was dried again for approximately 5 minutes in the 120℃ oven to fully eliminate solvent.

Dry powder was sieved using 100 mesh sieve, as shown in Figure 4.8. Then, the fabricated powder of each layer of the FGM was produced at a size smaller than 150 ㎛.

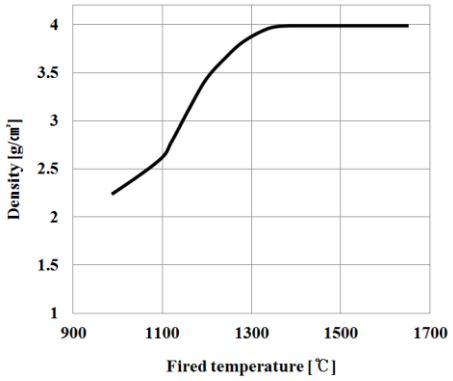

Densification behaviors

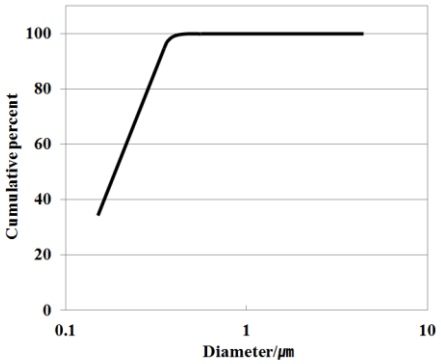

Particle size distributions

[Uniaxial pressed (98 MPa) and fired (1 hour in air)]

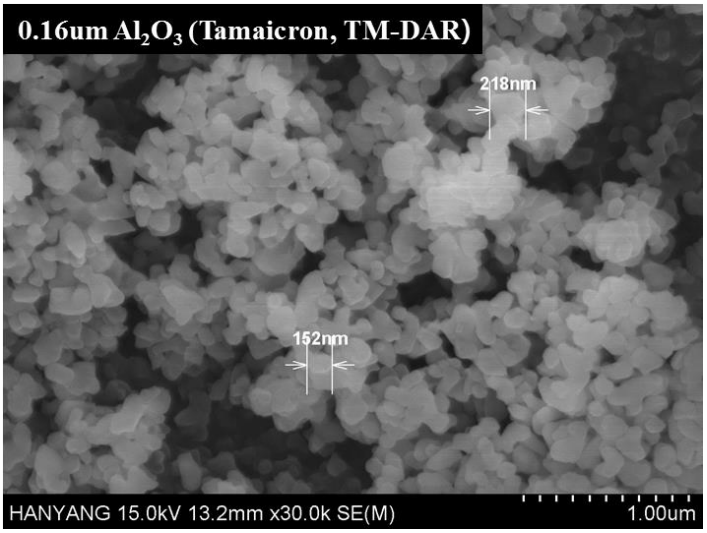

SEM photograph of 'TM-DAR'

Figure 4.4 Information and SEM photograph of alumina particles (TM-DAR) used in the study

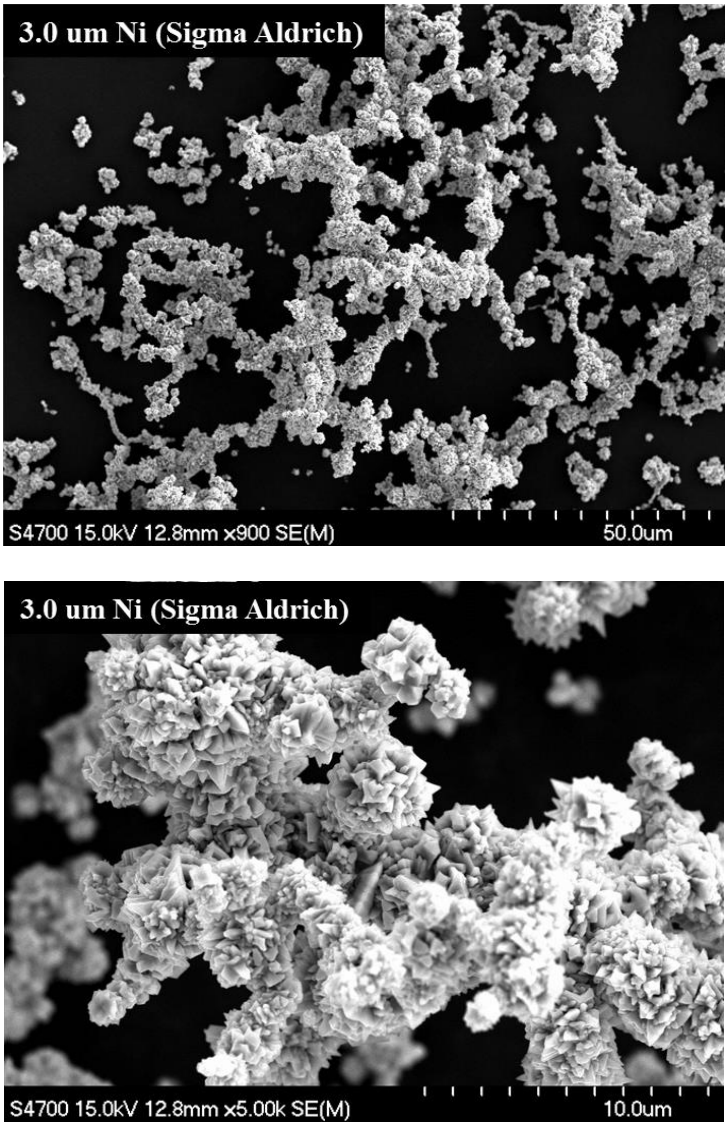

Figure 4.5 SEM photograph of nickel particles used in the study

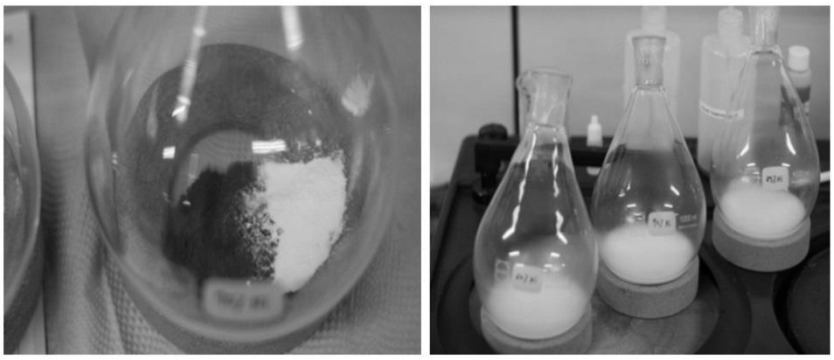

Figure 4.6 Mixed powder using solvent (99.9% ethanol) in 1000 mL flask

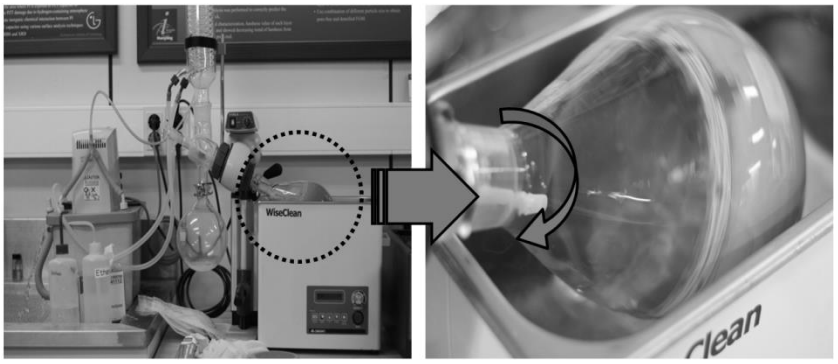

Figure 4.7 Simultaneous use of an evaporator and sonicator for drying and mixing

Figure 4.8 Sieving of dry powder using 100 mesh sieve

4.2.2 Green-body

Because a green-body of ceramic powder is weak and can exhibit cracking, special care should be taken to its fabrication during manufacturing. Fabricated powder was stacked sequentially into a cylindrical mold that was 25.4 mm in diameter. The stacked powder received a constant pressure by uniaxial cold press (CP). The stacked powder was pressed using a cold press with an 8000 kg load for 8 minutes. The stacked powder became the green-body. When the stacked powder was pressed by the CP, the stress gradient in the interior of stacked powder was generated from the shear stress generated by the friction of the mold wall. The large gradient of the generated stress negatively influences the density of the green-body. To improve green-body density, a cold isostatic press (CIP) method was used. The green-body was pressed using the cold isostatic press with a 100 MPa load for 5 minutes.

4.2.3 Sintering

The fabricated green-body was sintered in a tube furnace with argon (Ar) atmosphere to prevent nickel oxidation. The maximum sintering temperature was 1350℃, and the specimen was cooled slowly at 2℃/min to minimize thermal residual stress during cooling. Figure 4.9 presents the sintering profile.

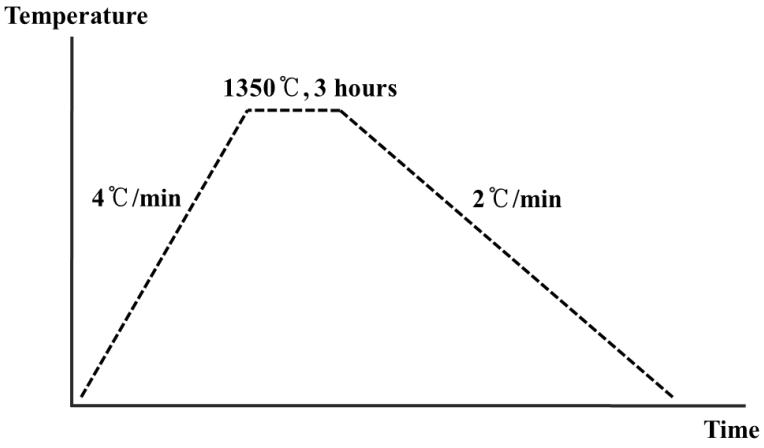

Figure 4.9 The sintering temperature curve used in the study

4.2.4 Fabricated FGM specimens

The FGM specimens used in the study were fabricated as shown in Figure 4.10. The 0.16 ㎛ Al_2O_3 + 3.0 ㎛ Ni FGM specimen has a rapidly changing curve at the outline of the 100% Ni layer because of the large difference in sintering shrinkage between the 100% Ni layer and the 90 vol.% Ni / 10 vol.% Al_2O_3 layer.

In comparison, the 1.0 ㎛ Al_2O_3 + 3.0 ㎛ Ni FGM specimen has a relatively small difference in sintering shrinkage; therefore, the outline of the 1.0 ㎛ Al_2O_3 + 3.0 ㎛ Ni FGM shows a gentle curve.

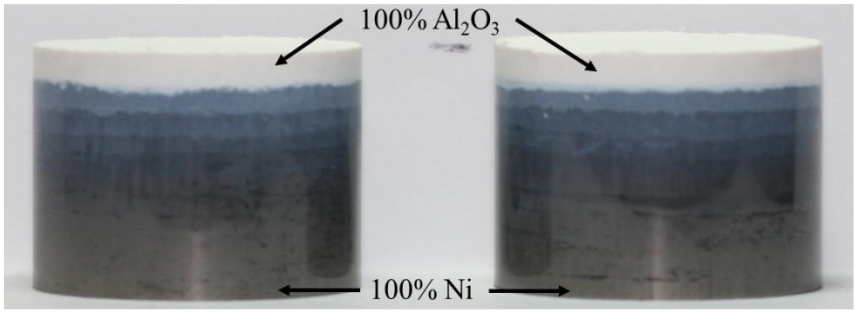

(a) Green-body

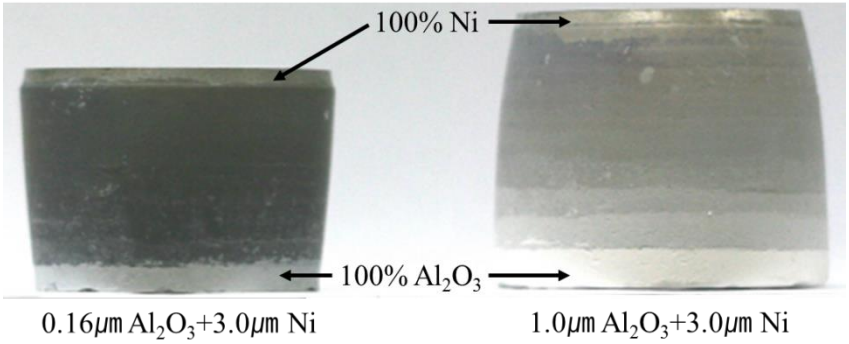

(b) Sintered-body

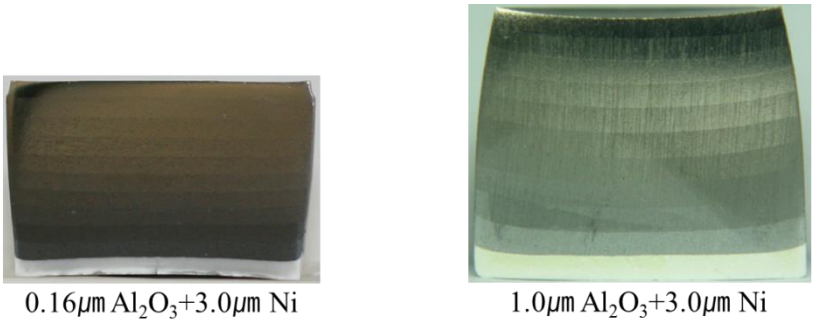

(c) Cross-section of sintered-body

Figure 4.10 The fabricated FGM used in the study

Chapter 5. Analysis of FGM density

The fabricated FGM contains pores. Therefore, it is necessary to distinguish the type of density corresponding to the existing pores. Pores generally can be divided into “closed pores” and “open pores.” The bulk volume includes all the pores of the subject. The true volume does not include any pores of the subject, as shown in Figure 5.1. However, the weight is not classified based on the pores.

Porosity can be calculated using Equation (5.1) and Equation (5.2), which present the relation between the bulk density and the true density:

$$D_{bulk} = \frac{M}{V_{bulk}} \qquad D_{true} = \frac{M}{V_{true}} \tag{5.1}$$

$$Porosity = \frac{(D_{true} - D_{bulk})}{D_{true}} \tag{5.2}$$

where *D* is density, *M* is weight, and *V* is volume [46, 47].

The value of the true density used in this study was quoted from the literature [80].

Shabana [48] estimated sintering shrinkage using the diameter measurement of the green-body and the sintered-body for the cylindrical FGM. The porosity of each layer of the FGM was calculated by estimated sintering shrinkage. However, this method presents significant error. This is

because the outer shell of the FGM has curves, and there is no flat boundary between the layers.

Also, a method using Archimedes principle can be used to measure the density of the entire FGM, but cannot be used to measure the density of each layer of the FGM.

Therefore, the following two methods were devised to estimate a more accurate bulk density for each layer of the FGM:

The first method makes individual specimens for the composition of each layer of the FGM in the same manufacturing of the FGM. Then, the bulk density of each layer of the FGM and the bulk density of the entire FGM are estimated using the weight and the volume measured from individual specimens.

With the second method, the fabricated FGM is cut in half. The image pixel of the cut cross-section of the FGM is measured using the Image Processing function of MATLAB. The measured image is compared with images already known for the area to calculate the area of the cut cross-section of the FGM. The volume of the FGM is estimated using the calculated area of the measured image. The bulk density of the FGM is calculated using the estimated volume and the weight inserted for each layer of the fabricated FGM.

In this study, the bulk density of each layer of the FGM was calculated by

a method using the individual specimen and a method using the Image Processing function of MATLAB. The bulk density of the entire FGM was also measured using the Archimedes principle. Its density was compared with the bulk densities estimated by proposed methods to check the validity of the proposed methods.

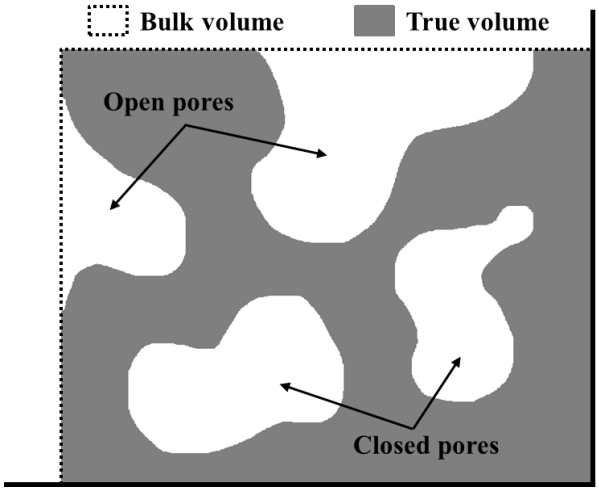

Figure 5.1 Bulk volume and true volume for specimen containing pores

5.1 Bulk density measurement of the FGM using Archimedes principle

If the object of the solid is immersed in a liquid, the weight of the solid is reduced. And its reduced weight is the same as the weight of the liquid displaced by the solid object. This is the Archimedes principle.

In this study, the bulk density of the entire FGM was measured using this principle. This method can measured the density of the entire FGM, but cannot measured the density of each layer of the FGM. The measurement procedure for the bulk density of the entire FGM using the Archimedes principle is the following:

(1) Measurement of the dry weight of the FGM:

The fabricated FGM is dried for 3 hours at 110℃, and then the dry weight (W1) is measured.

(2) Preparation of water-saturated sample:

The FGM is immersed into distilled water and boiled for 3 hours, and cooled to room temperature. This is the water-saturated sample.

(3) Weight measurement of water-saturated samples in water:

A weight of water-saturated samples hanging in the water with a wire having a diameter of 1 mm is measured. The weight (W2) in the water of the water-saturated sample is obtained by subtracting the weight of the wire from the measured value.

(4) Weight measurement of water-saturated samples in air:

A water-saturated sample is taken out of the water. The sample surface is wiped with a towel, and the weight of this sample is measured in air. This is the weight (W3) of the water-saturated sample in air.

The determined W1, W2, W3, and density of water at room temperature (ρ_{water}) are substituted into Equation (5.3). Thus, the bulk density of the entire FGM is calculated as shown in Table 5.1:

$$Bulk\ density = \frac{W1}{W3-W2} \times \rho_{water} \tag{5.3}$$

The calculated bulk density of the 0.16 ㎛ Al_2O_3 + 3.0 ㎛ Ni FGM specimen was 90.65% of 6.43 g/cc, which is true density of the entire FGM calculated by the Voigt model. In addition, the bulk density of the 1.0 ㎛ Al_2O_3 + 3.0 ㎛ Ni FGM specimen was confirmed to be 63.76% of 6.43 g/cc.

Table 5.1 Variables that are used in calculating bulk density of the entire FGM and the calculated result

	W1 [g]	W2 [g]	W3 [g]	ρ_{water} [g/cc]	Bulk density [g/cc]
0.16 ㎛ Al_2O_3 + 3.0 ㎛ Ni FGM specimen	35.21	29.59	35.61	0.9965	5.83
1.0 ㎛ Al_2O_3 + 3.0 ㎛ Ni FGM specimen	35.23	29.58	38.15	0.9965	4.10

5.2 Bulk density measurement of each layer of the FGM using individual specimens

The green-body of the individual specimens for the composition of each layer of the fabricated FGM was made with the same mixed powders that were used in the fabrication of the FGM into the 12 mm diameter cylindrical mold. Then, its green-body was sintered with the same conditions and processes that were used in the fabrication of the FGM. Figure 5.2 shows the individual specimens used in the study. Height and diameter of the green-body of the individual specimens were measured using Vernier calipers, and their volume was calculated by measured values. The bulk density of the green-body of the individual specimens was estimated using the measured weight and the calculated volume, as shown in Table 5.2.

The green-body of the individual specimens of each layer of the 0.16 ㎛ Al_2O_3 + 3.0 ㎛ Ni FGM was sintered using the conditions that are employed in the fabrication of the FGM, such as the temperature rise rate of 4℃/min, the maintenance of 3 hours at 1350℃, and cooling rate of 2℃/min in a tube furnace with argon (Ar) atmosphere to prevent nickel oxidation. The weight of the individual specimens of each layer of the 0.16 ㎛ Al_2O_3 + 3.0 ㎛ Ni FGM was measured using an electronic balance. Then, the bulk density of its specimens was measured using the Archimedes principle. Further, the porosity was estimated by the obtained bulk density and the calculated theoretical true density, as shown in Table 5.3.

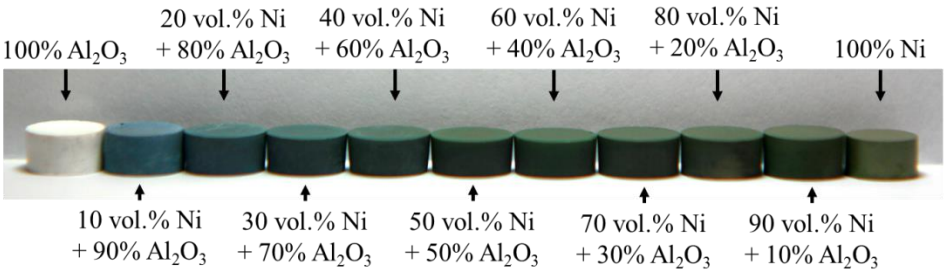

Figure 5.2 The fabricated individual specimens of each layer of the 0.16 ㎛ Al_2O_3 + 3.0 ㎛ Ni FGM

Table 5.2 The measured weight and volume and the bulk density after CIP and after CP of the green-body for individual specimens of each layer of the 0.16 μm Al_2O_3 + 3.0 μm Ni FGM

Ni vol. fraction	Specimen after CP (green-body)			Specimen after CIP (green-body)		
	Weight (g)	Bulk volume (cc)	Bulk density (g/cc)	Weight (g)	Bulk volume (cc)	Bulk density (g/cc)
0	1.559	0.705	2.210	1.559	0.695	2.242
0.1	1.753	0.679	2.583	1.753	0.672	2.610
0.2	1.949	0.655	2.976	1.949	0.648	3.008
0.3	2.140	0.640	3.346	2.140	0.630	3.396
0.4	2.334	0.627	3.722	2.334	0.618	3.777
0.5	2.530	0.607	4.168	2.530	0.599	4.225
0.6	2.725	0.604	4.510	2.725	0.596	4.569
0.7	2.920	0.631	4.625	2.920	0.624	4.683
0.8	3.114	0.654	4.762	3.114	0.648	4.804
0.9	3.307	0.683	4.842	3.307	0.674	4.907
1	3.502	0.721	4.855	3.502	0.713	4.909

Table 5.3 The measured weight and bulk density, and the porosity of the individual specimens of each layer of the 0.16 ㎛ Al_2O_3 + 3.0 ㎛ Ni FGM

Ni vol. fraction	Sintered-body		Theoretical true density (g/cc)	Green-body	Sintered-body
	Weight (g)	Bulk density (g/cc)		Porosity	Porosity
0	1.535	3.372	3.960	0.434	0.148
0.1	1.745	3.736	4.454	0.414	0.161
0.2	1.946	4.093	4.948	0.392	0.173
0.3	2.133	4.456	5.442	0.376	0.181
0.4	2.330	4.844	5.936	0.364	0.184
0.5	2.522	5.227	6.430	0.343	0.187
0.6	2.717	5.613	6.924	0.340	0.189
0.7	2.911	5.768	7.418	0.369	0.222
0.8	3.107	5.929	7.912	0.393	0.251
0.9	3.298	6.213	8.406	0.416	0.261
1	3.494	8.687	8.900	0.448	0.024

5.3 Bulk density measurement of each layer of the FGM using Image Processing of MATLAB

The second method estimated the bulk volume and the bulk density of the 0.16 ㎛ Al_2O_3 + 3.0 ㎛ Ni FGM by the following process.

(1) The fabricated FGM was precisely cut in half.

(2) The cut cross-section of the FGM was polished to clearly confirm interface of layers of the FGM.

(3) High-resolution image files of the cut cross-section was generated using the digital microscope.

(4) The outermost curve of the captured cross-sectional image was made as shown in Figure 5.3. Then, the rectangularness contained in this curve completely was generated to compare with the outermost curve of the captured cross-sectional image. The area of the rectangularness was calculated by measurement of the width and height.

(5) The captured cross-sectional image and the rectangularness generated as target image were placed side by side, as shown in Figure 5.4. Then, the area proportion of the captured cross-sectional image as compared with the rectangularness was calculated by image pixel using the Image Processing function of MATLAB.

(6) In the same way, the image for each layer from the captured cross-sectional image of the FGM was made as shown in Figure 5.5. Then, the area proportion of this image for each layer as compared with the captured cross-sectional image of the FGM was calculated the same way.

(7) Because the fabricated FGM has a cylindrical shape, the area ratio of each layer of the FGM is the same as the ratio of the volume created by rotation of the center axis of the area. Therefore, the bulk volume of each layer of the FGM was calculated using this principle as the following process.

The area of the rectangularness as target image of the green-body of the FGM, as shown in Figure 5.3 (a), was calculated using Equation (5.4).

$$2.519 * 1.849 = 4.6576\ cm^2 \tag{5.4}$$

The volume of the rectangularness was calculated as Equation (5.5) using one-half of the area of the rectangularness.

$$\pi * \left(\frac{2.519}{2}\right)^2 * 1.849 = 9.2147\ \text{cm}^3 \tag{5.5}$$

The area proportion of the captured cross-sectional image of the green-

body of the FGM as compared with the rectangularness was 97.9574%, as shown in Figure 5.4 (a).Thus, the bulk volume of the green-body of the FGM was calculated using Equation (5.6).

$$9.2147 * 0.979574 = 9.02648\ \mathrm{cm}^3 \quad (5.6)$$

The bulk volume of each layer of the FGM was determined by the same method. The area proportion of the 60 vol.% Ni/40 vol.% Al_2O_3 layer as compared with the captured cross-sectional image of the green-body of the entire FGM was 8.5651%, as shown in Figure 5.5 (a).

Accordingly, 8.5651% of the bulk volume of the green-body of the FGM calculated by Equation (5.6) became the bulk volume of the 60 vol.% Ni/40 vol.% Al_2O_3 layer, as shown in Equation (5.7).

$$9.02648 * 0.085651 = 0.7731\mathrm{cm}^3 \quad (5.7)$$

The bulk volume of all the layers making up the FGM was calculated in the same way.

(8) The final weight and volume of each layer of the FGM require correction. This is because the sum of the area ratio of each layer must become 1.0. However, the measured sum is 0.9955. This error was generated by the inserted boundary line. Therefore, the area ratio of each layer of the FGM

was divided into the sum of the area ratio to become 1. The corrected bulk volume of each layer of the FGM was determined, as shown in Table 5.4, by multiplying the corrected area ratio and the previously calculated bulk volume of each layer of the FGM. In the same manner, the weight of the green-body of the FGM (35.365 g) and the weight of the sintered-body of the FGM (35.192 g) showed a slight difference. This is because the powder was lost in the manufacturing process, and the moisture and other impurities contained in the powder was removed by the sintering process. This weight of each layer was corrected at the same rate based on the weight of the sintered-body, as shown in Table 5.5.

The final bulk density of 0.16 ㎛ Al_2O_3 + 3.0 ㎛ Ni FGM was calculated as shown in Table 5.4 (green-body) and Table 5.5 (sintered-body).

(a) Green-body

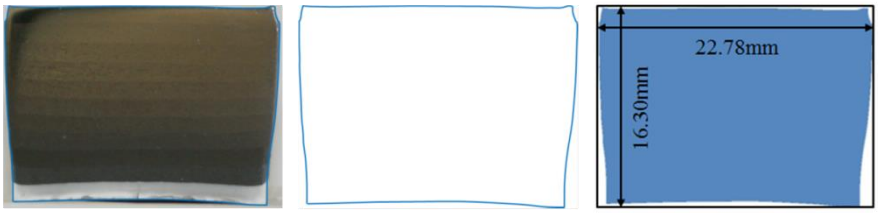

(b) Sintered body

Figure 5.3 The outermost curve of captured cross-sectional image and the rectangularness contained this curve completely for the 0.16 ㎛ Al_2O_3 + 3.0 ㎛ Ni FGM

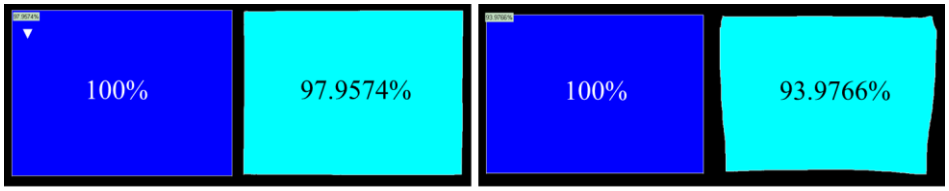

(a) Green-body (b) Sintered body

Figure 5.4 The measurement of area proportion of the captured cross-sectional image of the FGM as compared with the rectangularness using Image Processing of MATLAB

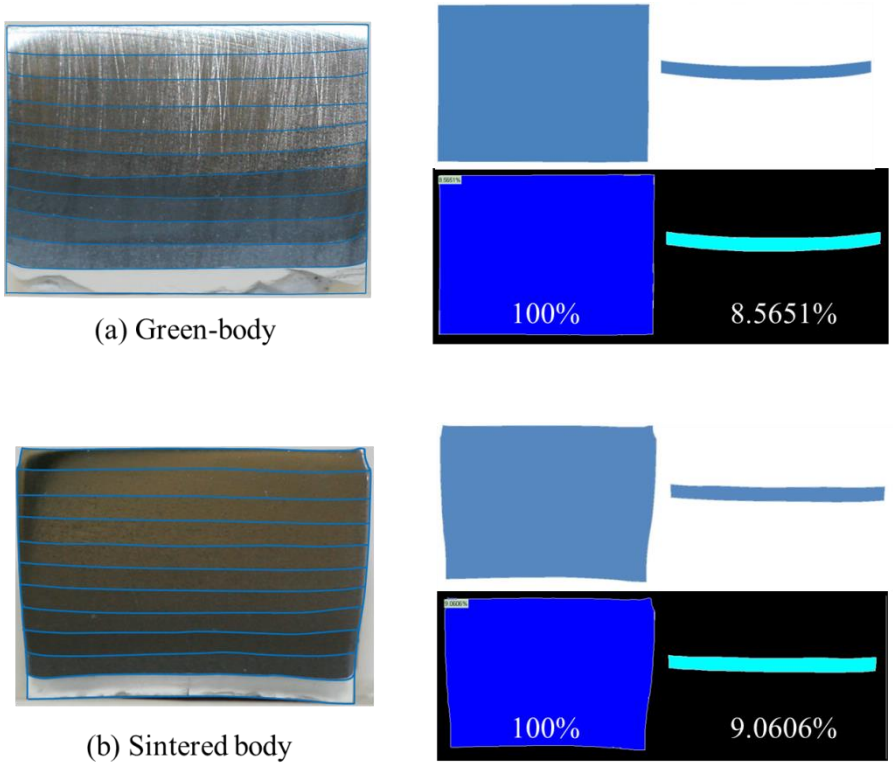

(a) Green-body

(b) Sintered body

Figure 5.5 The measurement of area proportion of 60 vol.% Ni / 40 vol.% Al_2O_3 layer consist of the FGM using Image Processing of MATLAB

Table 5.4 Measured, corrected, and final estimated bulk density of each layer of green-body of the 0.16 ㎛ Al_2O_3 + 3.0 ㎛ Ni FGM

Layer no.	Ni vol. fraction	Measured area rate (%)	Modified area rate	Modified bulk volume (cc)	Measured weight (g)	Bulk density (g/cc)
1	0	9.7745	0.09818	0.88625	1.980	2.234
2	0.1	9.3601	0.09402	0.84868	2.227	2.624
3	0.2	9.2023	0.09244	0.83437	2.474	2.965
4	0.3	8.967	0.09007	0.81304	2.721	3.347
5	0.4	8.4786	0.08517	0.76875	2.968	3.861
6	0.5	8.3831	0.08421	0.76009	3.215	4.230
7	0.6	8.5651	0.08604	0.77660	3.462	4.458
8	0.7	8.8977	0.08938	0.80675	3.709	4.597
9	0.8	9.0831	0.09124	0.82356	3.956	4.804
10	0.9	9.2037	0.09245	0.83450	4.203	5.037
11	1	9.6381	0.09681	0.87389	4.450	5.092
	Total	99.5533	1.00000	9.02648	35.365	

Table 5.5 Measured, corrected, and final estimated bulk density of each layer of sintered-body of the 0.16 ㎛ Al_2O_3 + 3.0 ㎛ Ni FGM

Layer no.	Ni vol. fraction	Measured area rate (%)	Modified area rate	Bulk volume (cc)	Modified weight (g)	Bulk density (g/cc)
1	0	8.3292	0.08526	0.53231	1.970	3.701
2	0.1	8.3412	0.08538	0.53307	2.216	4.157
3	0.2	8.3675	0.08565	0.53475	2.462	4.604
4	0.3	8.4507	0.08651	0.54007	2.708	5.014
5	0.4	8.5851	0.08788	0.54866	2.953	5.382
6	0.5	8.7913	0.08999	0.56184	3.199	5.694
7	0.6	9.0606	0.09275	0.57905	3.445	5.949
8	0.7	9.5205	0.09746	0.60844	3.691	6.066
9	0.8	9.9314	0.10166	0.63470	3.937	6.203
10	0.9	10.138	0.10378	0.64790	4.182	6.455
11	1	8.1738	0.08367	0.52237	4.428	8.477
Total		97.6893	1.00000	6.24316	35.192	

5.4 Comparison of bulk density results

In this study, the method using individual specimens and the method using Image Processing were proposed as measurement methods of the bulk density of each layer of the FGM. The bulk density of each layer of 0.16 ㎛ Al_2O_3 + 3.0 ㎛ Ni FGM was estimated by these methods, as shown in Table 5.6. Moreover, the bulk density of the entire FGM was measured using the Archimedes principle to confirm the validity of both methods. The measurement result was 5.829 g/cc. This bulk density was reduced by 9.35% as compared with the theoretical true density.

The bulk density of the entire FGM obtained by the method of individual specimens was 5.267 g/cc. This bulk density had a difference of 9.64% as compared with the bulk density measured by the Archimedes principle.

Meanwhile, the bulk density of the entire FGM obtained by the Image Processing method was 5.772 g/cc. This bulk density had a difference of 0.98% as compared with the bulk density measured by the Archimedes principle.

Thus, this author concludes that the method using Image Processing is more suitable for measurement of the bulk density of each layer of the FGM than the method using the individual specimens.

For this reason, the bulk density of each layer of 1.0 ㎛ Al_2O_3 + 3.0 ㎛ Ni FGM was estimated using the Image Processing function of MATLAB, as shown in Table 5.7.

This bulk density of sintered-body was compared with the bulk density of sintered-body of 0.16 ㎛ Al_2O_3 + 3.0 ㎛ Ni FGM, as shown in Figure 5.8.

Then, the porosities for the sintered-body of 0.16 ㎛ Al_2O_3 + 3.0 ㎛ Ni FGM and the sintered-body of 1.0 ㎛ Al_2O_3 + 3.0 ㎛ Ni FGM were calculated by Equation (5.2), as shown in Figure 5.9

Table 5.6 The bulk density estimated by two methods for each layer of sintered-body of 0.16 ㎛ Al_2O_3 + 3.0 ㎛ Ni FGM and theoretical true density

Ni vol. fraction	Bulk density of the FGM using Archimedes principle (g/cc)	Bulk density using individual specimens (g/cc)	Bulk density using Image Processing (g/cc)	Theoretical true density (g/cc)
0	-	3.372	3.807	3.960
0.1		3.736	4.276	4.454
0.2		4.093	4.758	4.948
0.3		4.456	5.157	5.442
0.4		4.844	5.536	5.936
0.5		5.227	5.857	6.430
0.6		5.613	6.119	6.924
0.7		5.768	6.240	7.418
0.8		5.929	6.380	7.912
0.9		6.213	6.639	8.406
1		8.687	8.719	8.900
Avg. Density	5.829	5.267	5.772	6.430

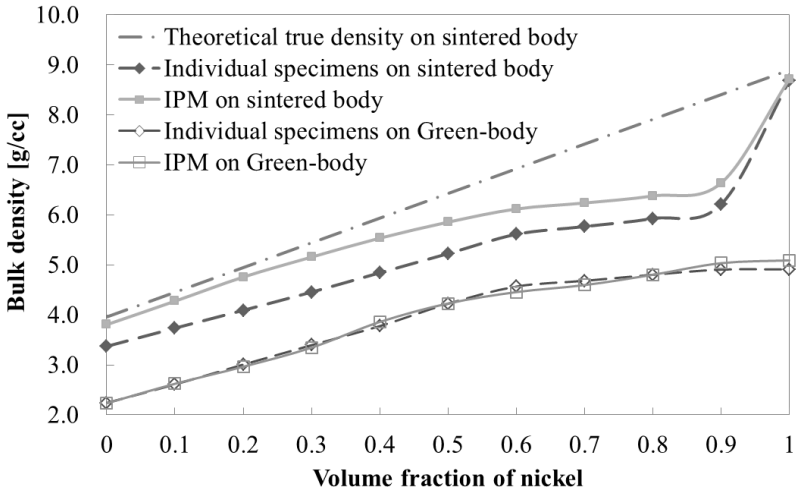

Figure 5.6 Bulk density corresponding to the volume fraction of nickel calculated by the proposed methods for 0.16 ㎛ Al_2O_3 + 3.0 ㎛ Ni FGM

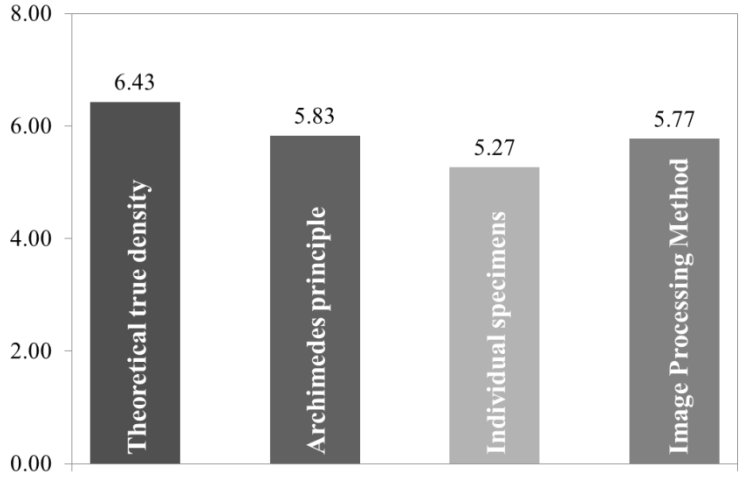

Figure 5.7 Bulk density calculated by the proposed methods and Archimedes principle and theoretical true density for 0.16 ㎛ Al_2O_3 + 3.0 ㎛ Ni FGM

Table 5.7 Measured, corrected, and final estimated bulk density of each layer of sintered-body of 1.0 ㎛ Al_2O_3 + 3.0 ㎛ Ni FGM

Layer no.	Ni vol. fraction	Measured area rate (%)	Modified area rate	Bulk volume (cc)	Modified weight (g)	Bulk density (g/cc)
1	0	10.400	0.103	0.891	1.980	2.221
2	0.1	10.186	0.101	0.873	2.227	2.551
3	0.2	9.969	0.099	0.854	2.474	2.895
4	0.3	9.787	0.097	0.839	2.721	3.244
5	0.4	9.598	0.095	0.823	2.968	3.608
6	0.5	9.376	0.093	0.804	3.215	4.001
7	0.6	9.009	0.090	0.772	3.462	4.483
8	0.7	8.731	0.087	0.748	3.709	4.956
9	0.8	8.349	0.083	0.716	3.956	5.528
10	0.9	7.873	0.078	0.675	4.203	6.228
11	1	7.359	0.073	0.631	4.450	7.054
Total		100.635	1.000	8.626	35.365	

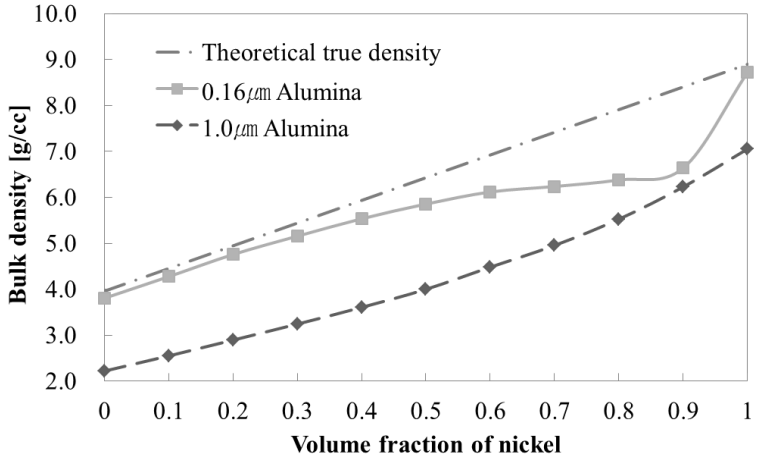

Figure 5.8 Bulk density corresponding to the volume fraction of nickel calculated using Image Processing for sintered-body of 0.16 ㎛ Al_2O_3 + 3.0 ㎛ Ni FGM and 1.0 ㎛ Al_2O_3 + 3.0 ㎛ Ni FGM

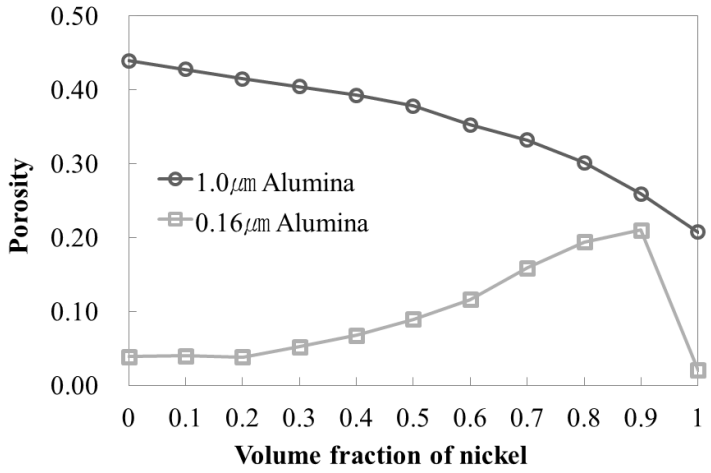

Figure 5.9 Porosity corresponding to the volume fraction of nickel calculated using Image Processing for sintered-body of 0.16 ㎛ Al_2O_3 + 3.0 ㎛ Ni FGM and 1.0 ㎛ Al_2O_3 + 3.0 ㎛ Ni FGM

Chapter 6. Material properties according to density variation

To analyze the sintering behavior of functionally graded materials, material properties such as elastic modulus, Poisson's ratio, and coefficient of thermal expansion are required. These can be obtained by experiment; however, it is possible to greatly increase the efficiency of experiments if the characteristics of FGM, as described in the following paragraphs, are used well.

Selection of materials between which a chemical reaction is not generated in the manufacturing process is the principle of the FGM field. This care in material selection is because it is difficult to predict the properties of a new material generated by a chemical bond. In addition, it is a principle that materials are mixed at a temperature below the melting point of the materials. Because of this principle, a FGM has an inherent characteristic of a solid material. The material properties also are changed to the same trend corresponding to the volume fraction of a material because of this characteristic. That is, when materials A and B are mixed, the elastic modulus of material A is greater than that of material B. Then, a composite mixed from 10 vol. % of material A is never greater than a composite mixed from 20 vol. % of material A for elastic modulus.

Several models have been proposed to estimate the material properties of two-phase composites based on this characteristic. The simplest and most

general of these models is the classical linear law of mixtures [13], which sums the product of volume fractions and corresponding properties of each material. The ‘modified law of mixtures’ [14] represents an advanced version of this model and applies empirical values to determine the compositional gradient between the two materials in the stress-strain curves. The ‘generalized law of mixtures’ [15], suggested by Fan *et al.* considers not only the volume fraction but also grain shape, particle size, and phase distribution and results in a better fit with experimental results than the other two methods. However, the general law of mixtures requires too many parameters for practical calculations and predicts only the elastic modulus and yield strength of a given material. Another means of calculating composite material properties is the ‘variation method’ derived by Hanshin and Shtrikman [33]. The variation method employs upper and lower boundaries according to the variables being calculated. The ‘micromechanical approach’ by Hill [17], Mori and Tanaka [16], Wakashima and Tsukamoto [84], and Ravichandran [51] *et al.* predicts effective material properties of composites by defining the relationship between reinforced particles and the matrix on the micro-scale.

However, these models all assume ideal bonding of the two materials and do not consider variables such as the porosity generated during pressureless sintering processes. New models that include process-induced factors, such as porosity, have been insufficient to describe the end composite properties.

Conversely, there exists a wealth of information on the elastic modulus of pure materials as a function of porosity. Models described by Sprigs [85] and

Hasselman [86] at the American Ceramic Conference in the 1960s are still widely used to describe the effects of porosity on the elastic modulus of ceramics. These models predict values that differ from experimental results by approximately 7% and differ by less than 1% from experimental results with cold-press sintering methods. However, these models are accurate for systems in which the porosity is less than 0.164; the error increases with the degree of porosity.

The self-congruent method, which was developed by Skorokhod [30], Mori and Tanaka [16], Zhao *et al*. [31], and Budiansky and O'Connell [32], based on studies by Mackenzie [27], Esheby [28], and Hill [29], represents another technique used to predict the material properties of pure, porous materials using a variation method [40]. However, self-congruent methods, which are based entirely on mathematical theory, tend to result in large differences with experimental values. For this reason, Koval'chenko [33] developed an approximation model to estimate the material properties of nickel as a function of porosity.

Study of property estimation for two composite mixed materials, as well as study of property change corresponding to porosity for a single material, have progressed as discussed. Research on property estimation of a composite that includes the two materials and the pores together, such as the FGM of this study, has not yet begun.

The current study proposes new models, based on the aforementioned studies, to predict the effective elastic modulus of Ni / Al_2O_3 FGMs fabricated by pressureless sintering as a function of porosity. The models

described here were verified by comparisons with measured values.

The Voigt (Equation (6.1)) and Reuss (Equation (6.2)) models have been used to describe the effective elastic modulus of a two-phase composite: Voigt model represents upper bound of the estimated properties and Reuss model shows the lower bound of the estimated properties.

Voigt model $$E_{composite} = E_{Ni} \cdot V_{Ni} + E_{Al_2O_3} \cdot V_{Al_2O_3} \quad (6.1)$$

Reuss model $$E_{composite} = \frac{E_{Ni} \cdot E_{Al_2O_3}}{E_{Ni} \cdot V_{Al_2O_3} + E_{Al_2O_3} \cdot V_{Ni}} \quad (6.2)$$

where E, P, and V are the elastic modulus, porosity, and volume fraction, respectively.

The Sprigs model (Equation (6.3)) was used to describe the effective elastic modulus of pure, porous alumina:

$$E(P) = E(0)\exp(-bP) \quad (6.3)$$

where $E(0)$ is the elastic modulus at zero percent porosity and b is an empirically derived parameter, with a value of 3.44 [85] as shown in Table 6.1. This model yields errors less than 1% relative to experimental results using cold-press sintering methods.

The current study also includes an approximation for the Poisson's ratio (ν), shear modulus (μ), and elastic modulus of pure nickel according to Koval'chenko as shown in Equation (6.4-6) [40]:

$$\frac{\nu(P)}{\nu(0)} = \rho^{\frac{3}{(1-k^2)\rho}} \tag{6.4}$$

$$\frac{\mu(P)}{\mu(0)} = \rho^{\frac{c-(1-k^2)\rho}{(1-k^2)\rho}} \tag{6.5}$$

$$E(P) = 2\mu(0)\left\{\frac{\mu(P)}{\mu(0)}\right\}\left\{1+\nu(0)\frac{\nu(P)}{\nu(0)}\right\} = 2\mu(P)\{1+\nu(P)\} \tag{6.6}$$

where ρ is the relative density of the material (or $P = 1-\rho$), c correlates with the Poisson's ratio ($c = 2$ for metallic materials such as nickel), and k accounts for the approximation curve ($k = 0$ for perfect material, $k = 6.5$ for imperfect material).

Figure 6.1 shows that the Koval'chenko model approximates the measured values for nickel when c and k are 2 and 4.0, respectively. Consequently, this model can be simplified as follows Equation (6.7):

$$E(P) = 2\mu(0)\left(\rho^{\frac{1}{0.42\rho}-1}\right)\left\{1+\nu(0)\rho^{\frac{1}{0.28\rho}}\right\} \tag{6.7}$$

The current study proposes three models for the prediction of effective elastic modulus in porous composite materials.

Table 6.1 Summary of values of constants E_0 and b for relation between elastic modulus (E) and porosity (P) for polycrystalline alumina specimens of several investigators [85]

General equation form : $E = E_0 \exp(-bP)$

Investigator	No. data point	Fabrication Technique *	Modulus measurement technique †	Porosity range (%) ‡	Zero porosity modulus ($\times 10^{-6}$ lb./sq. in.)	Empirical constant b	Max. range of differences between exp. and cal., moduli (- % to + %) #
Crandall et al.	13	H. P.	E_l	0.30- 4.32	59.96	4.08	0.56 to 0.38
Sprigs and Vasilos	18	H. P.	V_l	0.93-32.28	59.10	4.35	5.01 to 6.94
Lang	9	C. P.	E_{fe}	2.13-16.42	59.38	3.44	0.46 to 0.85
Lang	9	C. P.	E_{fw}	2.13-16.42	59.54	3.44	0.93 to 0.81
Lang	7	C. P.	E_l	4.09-16.42	60.08	3.55	0.17 to 0.22
Coble and Kingery	5	S.C	E_{tb}	10.0-37.0	58.77	2.73	4.34 to 2.72
Lang	7	H. P.	E_{fw}	0.11-2.78	58.76	2.06	0.87 to 0.68
Lang	7	H. P.	E_{fe}	0.11-2.78	58.53	1.61	1.08 to 0.41

* Fabrication code: **H.P.** = hot-pressed, **C. P.** = cold-pressed and sintered, **S. C.** = slip cast and sintered

† Modulus measurement code: E_l =longitydinal resonant frequency, V_l =longitudinal velocity of sound, E_{fe} =edgewise flexural vibration, E_{fw} =flatwise flexural vibration, E_{tb} =static modulus from transverse bend.

‡ A value of 3.987 gm./cc has been taken as the limiting theoretical X-ray density of Al_2O_3

In terms of per cent of calculated value of the modulus

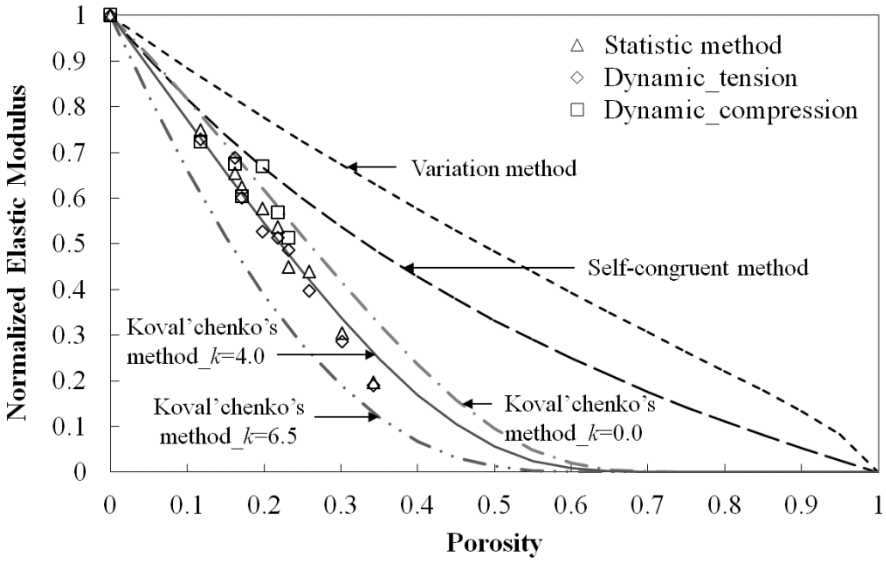

Figure 6.1 Comparison of calculated and measured values [22] of elastic modulus as a function of porosity

6.1 First model for estimation of effective material property: porosity can be separated by volume fraction

The first model formulate a hypothesis that the porosity of a composite can be divided according to the volume fraction of pores in each material, as illustrated in Figure 6.2.

Based on this hypothesis, porosities of each material were calculated according to Equation (6.8):

$$P_{Al_2O_3} = P_{composite} V_{Al_2O_3} \quad ; \quad P_{Ni} = P_{composite} V_{Ni} \tag{6.8}$$

A model for the effective elastic modulus of alumina was determined by substituting the alumina porosity obtained by Equation (6.8) for Sprigs' model, as shown in Equation (6.9). An analogous model was generated for nickel using Equation (6.9) and Equation (6.10):

$$E_{Al_2O_3}\left(P_{Al_2O_3}\right) = E_{Al_2O_3}(0)\exp\left(-bP_{Al_2O_3}\right) \tag{6.9}$$

$$E_{Ni}\left(P_{Ni}\right) = 2\mu_{Ni}(0)\left\{\left(1-P_{Ni}\right)^{\frac{1}{0.42\left(1-P_{Ni}\right)}-1}\right\}\left\{1+\nu_{Ni}(0)\left(1-P_{Ni}\right)^{\frac{1}{0.28\left(1-P_{Ni}\right)}}\right\} \tag{6.10}$$

The models of effective elastic modulus for each material were then substituted into the form of the Voigt and Reuss models, as given in Equation (6.11) and Equation (6.12), respectively:

$$E_{composite}(P) = E_{Al_2O_3}\left(P_{Al_2O_3}\right)V_{Al_2O_3} + E_{Ni}(P_{Ni})V_{Ni} \tag{6.11}$$

$$E_{composite}(P) = \left(\frac{V_{Al_2O_3}}{E_{Al_2O_3}\left(P_{Al_2O_3}\right)} + \frac{V_{Ni}}{E_{Ni}(P_{Ni})} \right)^{-1} \tag{6.12}$$

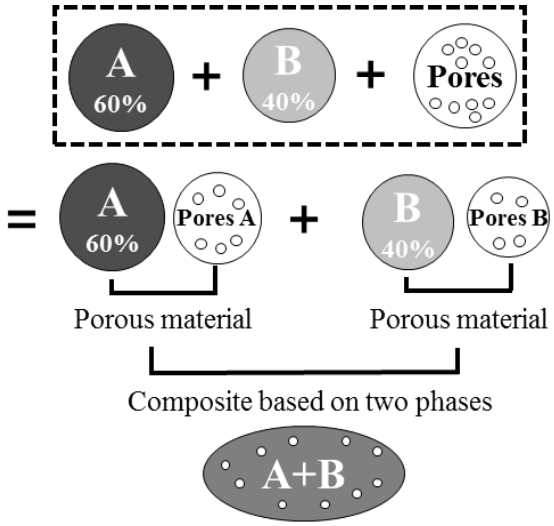

Figure 6.2 Schematic diagram of the first model

6.2 Second model for estimation of effective material property: all porosity is associated with the matrix

The second model formulate a hypothesis that the porosity of the composite occurs only in the matrix material as illustrated in Figure 6.3. As defined in previous studies [46-48], the alumina matrix of the nickel/alumina composite contains greater than 40 volume percent alumina.

Based on this hypothesis, the model of the effective elastic modulus of alumina was determined by substituting the alumina porosity in Equation (6.3). The effective elastic modulus of nickel, however, was unchanged when alumina was present at matrix levels (Equation (6.13)). Similarly, the model of the effective elastic modulus of nickel was determined by substituting the nickel porosity in Equation (6.3), while that of alumina was unchanged when nickel was present at matrix levels (Equation (6.14)).

Alumina matrix:

$$E_{Al_2O_3}(P) = E_{Al_2O_3}(0)\exp(-bP) \quad , \quad E_{Ni}(0) = E_{Ni} \tag{6.13}$$

Nickel matrix:

$$E_{Ni}(P) = 2\mu_{Ni}(0)\left\{(1-P)^{\frac{1}{0.42(1-P)}-1}\right\}\left\{1+\nu_{Ni}(0)(1-P)^{\frac{1}{0.28(1-P)}}\right\} \quad , \quad E_{Al_2O_3}(0) = E_{Al_2O_3} \tag{6.14}$$

As above, these models were then substituted into the Voigt and Reuss models. The final forms of the second model were as follows Equation

(6.15-18).

Voigt model form of the second model

Alumina matrix:

$$E_{composite}(P) = E_{Al_2O_3}(P)V_{Al_2O_3} + E_{Ni}(0)V_{Ni} \tag{6.15}$$

Nickel matrix:

$$E_{composite}(P) = E_{Al_2O_3}(0)V_{Al_2O_3} + E_{Ni}(P)V_{Ni} \tag{6.16}$$

Reuss model form of the second model

Alumina matrix:

$$E_{composite}(P) = \left(\frac{V_{Al_2O_3}}{E_{Al_2O_3}(P)} + \frac{V_{Ni}}{E_{Ni}(0)} \right)^{-1} \tag{6.17}$$

Nickel matrix:

$$E_{composite}(P) = \left(\frac{V_{Al_2O_3}}{E_{Al_2O_3}(0)} + \frac{V_{Ni}}{E_{Ni}(P)} \right)^{-1} \tag{6.18}$$

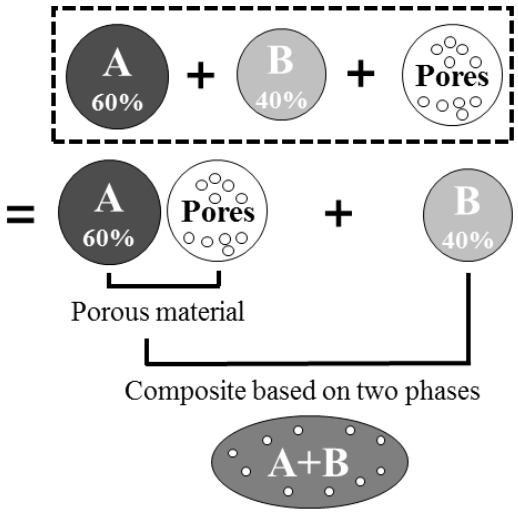

Figure 6.3 Schematic diagram of the second model: (A) matrix, (B) reinforced particles

6.3 Third model for estimation of effective material property: Using fitting curve based on experimental values

The third model generates a curve that fit experimental data of alumina and nickel porosity. This curve then represents the effective material properties of a composite as a function of porosity. First, the elastic modulus of nonporous composites was calculated according to the Voigt and Reuss models. Second, a new fitting curve, shown in Figure 6.5, was applied to represent the elastic modulus of the final composite.

Variation in the measured elastic modulus of pure materials as a function of porosity was adapted from previous studies [85, 86, 40]; fitting curves of the final composites were induced from a modified form of the Koval'chenko model. Modified forms of Poisson's ratio and shear modulus are given in Equation (6.19) and Equation (6.20) respectively:

$$\nu_{composite}(P) = \nu_{composite}(0)\left\{(1-P)^{\frac{3}{(1-P)}}\right\} \tag{6.19}$$

$$\mu_{composite}(P) = \mu_{composite}(0)\left\{(1-P)^{\frac{2.8-(1-P)}{(1-P)}}\right\} = \mu_{composite}(0)\left\{(1-P)^{\frac{2.8}{(1-P)}-1}\right\} \tag{6.20}$$

where $\nu_{composite}(0)$ and $\mu_{composite}(0)$ are Poisson's ratio and the shear modulus of a composite as calculated by the Voigt and Reuss models assuming zero percent porosity.

Then, the elastic modulus of composites as a function of porosity, $E_{composite}(P)$, was calculated by combining Equation (6.19) and Equation (6.19) to generate Equation (6.21):

$$E_{composite}(P) = 2\mu_{composite}(P)\{1+\nu_{composite}(P)\} \tag{6.21}$$

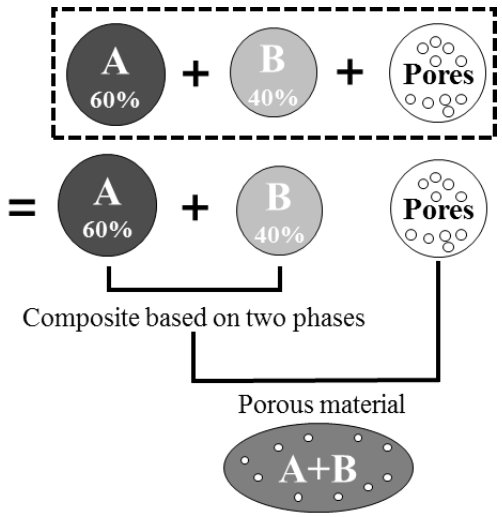

Figure 6.4 Schematic diagram of the third model

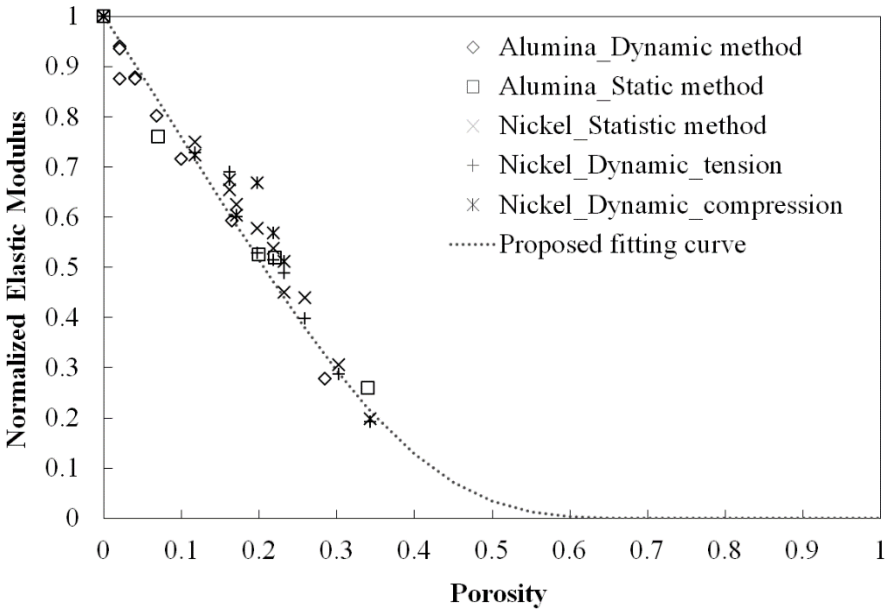

Figure 6.5 Measured elastic modulus as a function of porosity [85, 86, 40] and the fitting curve representing the final composite

6.4 Elastic modulus measurement on the FGM

A FISCHERSCOPE® HM2000 microindenter as shown in Figure 6.6 was used to measure the elastic modulus of each layer of the FGM and is suitable for determining surface hardness, elastic and plastic properties, indentation modulus, and elastic-plastic energy portions according to ISO 14577-1.

Polished cross-section was adjusted to be horizontal with indenter tip of Micro Indenter. And this measurement was conducted 10 times as a certain distance in each layer of the FGM. Maximum and minimum values of the measured results were excluded. And, the average value, the upper limit, and lower limit was determined in the rest value of the measured results.

Technical data Measuring head: Maximum test load: 2000 mN, Maximum indentation depth: 150 μm, Load resolution: ≤ 0.04 mN, Distance resolution: ≤ 100 pm, Approach speed of the indenter: ≤ 2 μm/s

Figure 6.6 FISCHERSCOPE® HM2000 used in elastic modulus measurement

6.5 Comparison between estimated values and measured values on elastic modulus

Elastic modulus values calculated according to each of the aforementioned models were compared to values measured by the micro indenter for 0.16㎛ Al_2O_3 + 3.0㎛ Ni FGM as shown in Figure 6.7 (Voigt model) and Figure 6.8 (Reuss model). The data in Figure 6.7 and Figure 6.8 show that the first and second models exhibited significant differences with the experimental measurements. In contrast, the third model yielded values within the error range of those measured with the micro indenter.

The value of the elastic modulus of 1.0㎛ Al_2O_3 + 3.0㎛ Ni FGM was estimated using the third model. Then it was measured by Micro Indenter in the same way.

The estimated values and the measured values of each layer of 1.0㎛ Al_2O_3 + 3.0㎛ Ni FGM were compared to each other as shown in Figure 6.10. An error range of the measured values included the estimated values such as previous 0.16㎛ Al_2O_3 + 3.0㎛ Ni FGM result (Figure 6.9).

Based on this result, third model was the most suitable for an estimation method of elastic modulus of the composite according to the porosity. Thus, it has become possible to estimate the elastic property of the composite which include pores in a manufacturing process.

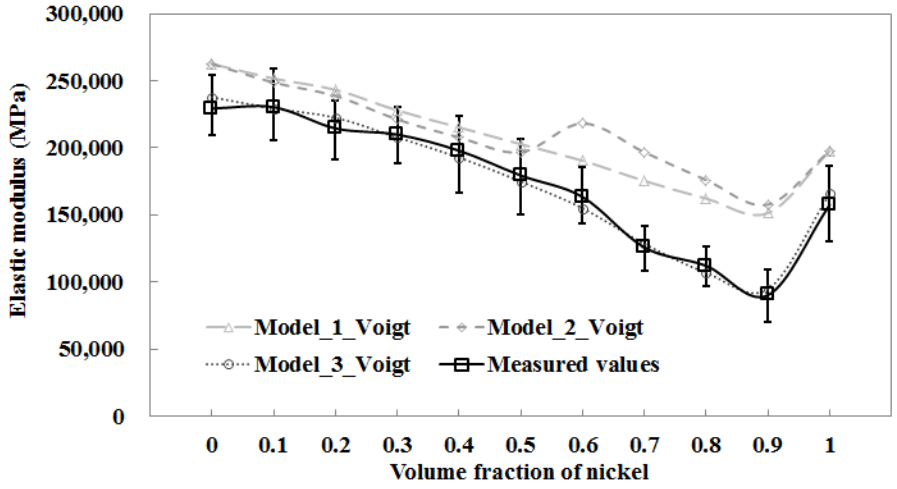

Figure 6.7 Comparison of measured values and those calculated according to the Voigt model for 0.16㎛ Al_2O_3 + 3.0㎛ Ni FGM

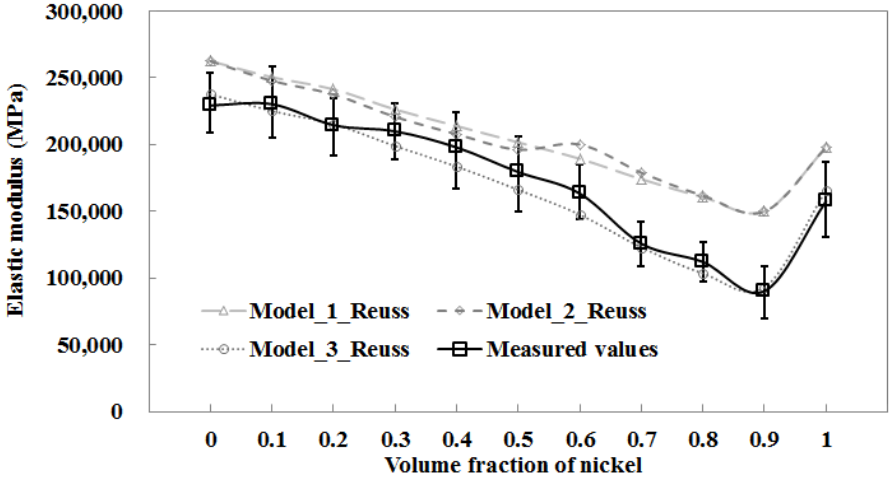

Figure 6.8 Comparison of measured values and those calculated according to the Reuss model for 0.16㎛ Al_2O_3 + 3.0㎛ Ni FGM

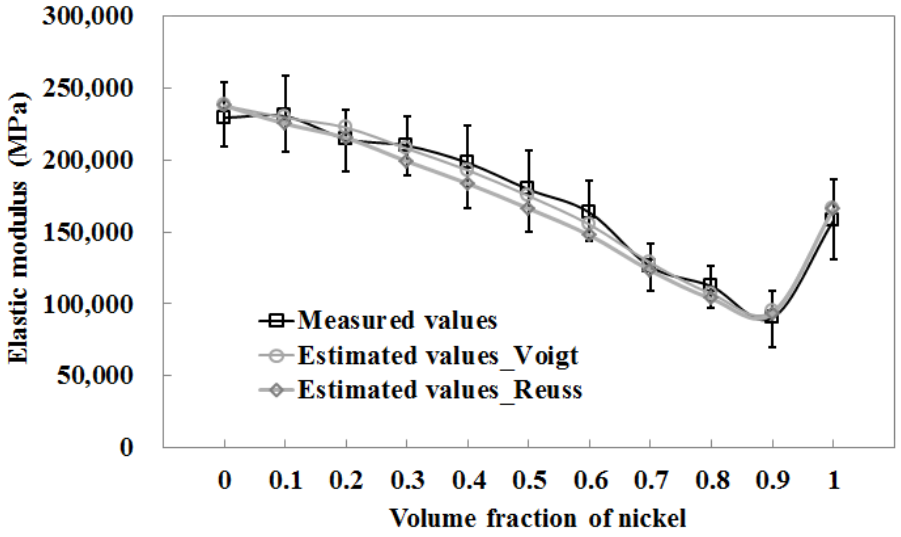

Figure 6.9 Comparison of measured values and those calculated according to the third model for 0.16㎛ Al_2O_3 + 3.0㎛ Ni FGM

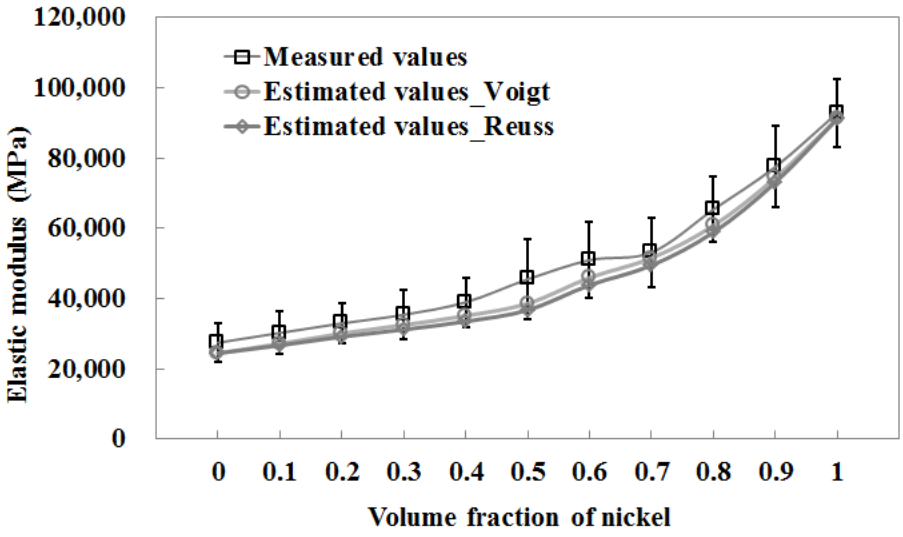

Figure 6.10 Comparison of measured values and those calculated according to the third model for 1.0㎛ Al_2O_3 + 3.0㎛ Ni FGM

6.6 Estimation of ultimate strength of the FGM

To estimate ultimate strength of each layer of the FGM, the third model, which was proposed and verified in elastic modulus, was used.

First, values of the ultimate strength and the ultimate strength corresponding to porosity for nickel and alumina was confirmed through the literature [87, 88]. To obtain the normalized strength of the nickel and alumina, the ultimate strength corresponding to porosity was divided into the ultimate strength of the pure nickel and pure alumina. The fitting curve through the normalized strength was defined by the quadratic Equation, as shown in Figure 6.11.

Values of the ultimate strength of the FGM corresponding to the volume fraction of nickel were calculated by Voigt and Reuss models, as shown in Figure 6.12.

The values of porosity of 0.16 ㎛ Al_2O_3 + 3.0 ㎛ Ni FGM and 1.0 ㎛ Al_2O_3 + 3.0 ㎛ Ni FGM, as shown in Figure 5.9, were combined with the fitting curve of Figure 6.11. In this manner, the change ratio of ultimate strength for each layer of the FGM was determined. Then, the determined change ratio was combined with the values of the ultimate strength of the FGM corresponding to the volume fraction of nickel.

The ultimate strength considering porosity and corresponding to the nickel volume fraction was estimated for 0.16 ㎛ Al_2O_3 + 3.0 ㎛ Ni FGM, as shown in Figure 6.13, and 1.0 ㎛ Al_2O_3 + 3.0 ㎛ Ni FGM, as shown in Figure 6.14.

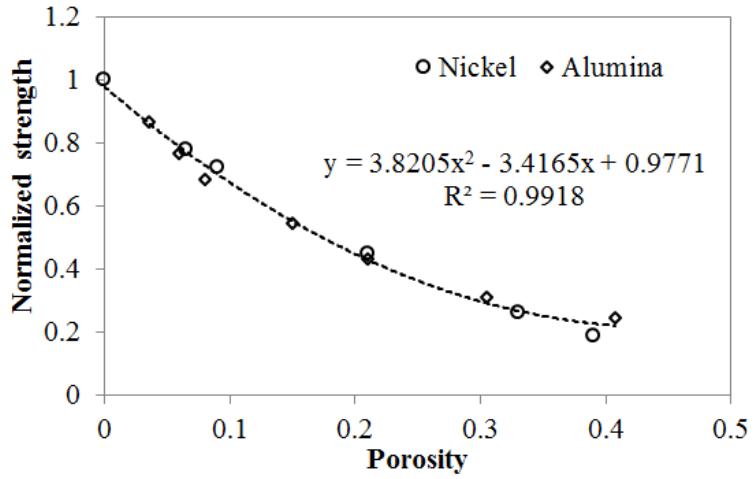

Figure 6.11 The fitting curve through the normalized strength and the quadratic equation of the fitting curve

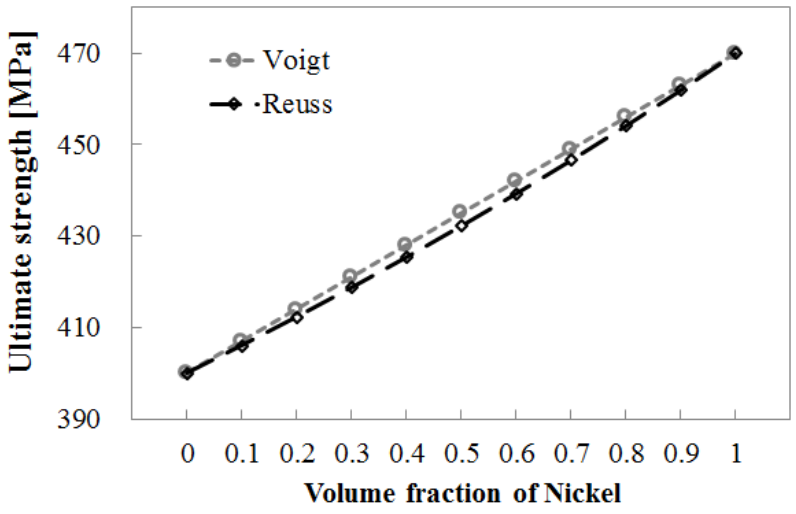

Figure 6.12 Ultimate strength corresponding to nickel volume fraction calculated by Voigt and Reuss models

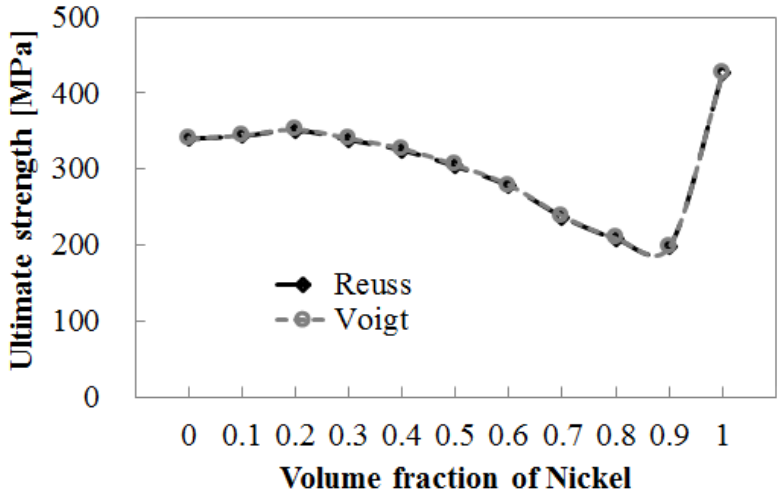

Figure 6.13 The estimated ultimate strength considering porosity and corresponding to the nickel volume fraction for 0.16 ㎛ Al_2O_3 + 3.0 ㎛ Ni FGM

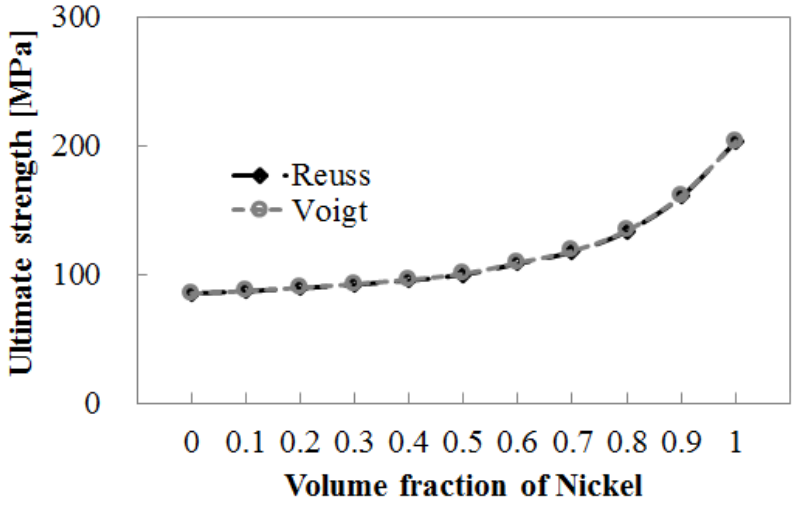

Figure 6.14 The estimated ultimate strength considering porosity and corresponding to the nickel volume fraction for 1.0 ㎛ Al_2O_3 + 3.0 ㎛ Ni FGM

Chapter 7. Measurement and prediction of sintering shrinkage

A FGM was manufactured in a variety of methods, including powder metallurgy, thermal spray, combustion synthesis, and deposition. Powder metallurgy is the science and technology of producing solid material from a powder by compaction and sintering. This method has the advantage of being a relatively simple process, and it can implement a variety of compositions with precision. For this reason, the powder metallurgy method was used in this study.

Pressureless sintering, hot pressing, hot isostatic pressing, spark plasma sintering, and microwave sintering are different types of sintering methods that are used in powder metallurgy.

The most economical manufacturing process of these sintering techniques is the pressureless sintering method. This method is simple, compared with other sintering methods, and does not require additional equipment.

However, the pressureless sintering method is difficult to use when fabricating a 100% dense sample. Moreover, when two components, which are different from each other in sintering shrinkage, are sintered in one material, this sample may become warped or deformed [6-10, 93-97].

To develop a new method for solving these problems, research is being conducted into a control of mold shape. In this new method, it is critical to

accurately predict the shape of the sintered specimen when the shape of the mold is not considered. This is because the difference in the predicted shape previously became the shape error of the final specimen. Therefore, for the exact shape prediction of the sintering specimen, the sintering shrinkage of the specimen material must be accurately measured.

This is also true for the FGM of this study. However, to measure sintering shrinkage of each layer of a FGM by experiment, specimens to measure sintering shrinkage must be fabricated up to the number of layers making up a FGM. Moreover, measurement time of 20 hours or more for each specimen is required.

Therefore, a method to reduce the cost and time for measuring sintering shrinkage effectively was devised using the material properties of FGMs mentioned in chapter 6 of this study. This method measured the sintering shrinkage of individual specimens of specific layers comprising the FGM. Then, a fitting curve of measured values was constructed. Using this fitting curve, the sintering shrinkage of individual specimens of the other layers that are not measured, and which make up the FGM, can be estimated.

7.1 Sintering shrinkage measurement on individual specimen of each layer of the FGM

The individual specimen of each layer of 0.16 ㎛ Al_2O_3 + 3.0 ㎛ Ni FGM was sintered using identical conditions and fabrication process employed for the FGM in the study. When this individual specimen was sintered, a dilatometer was used instead of a tube furnace. Thus, the sintering shrinkage of each specimen was measured, as shown in Figure 7.1.

Shrinkage of the specimen of 100% Ni was initiated at 585℃, and shrinkage of the specimen of 100% Al_2O_3 was initiated at 965℃. While maintaining the temperature at 1350℃ for 3 hours, the higher the volume fraction of nickel, the larger the radius of curvature of the shrinkage to a moderate extent. In addition, the measured sintering shrinkage between the specimen of 100% Ni and the specimen of 90 vol.% Ni + 10 vol.% Al_2O_3 showed a very large difference.

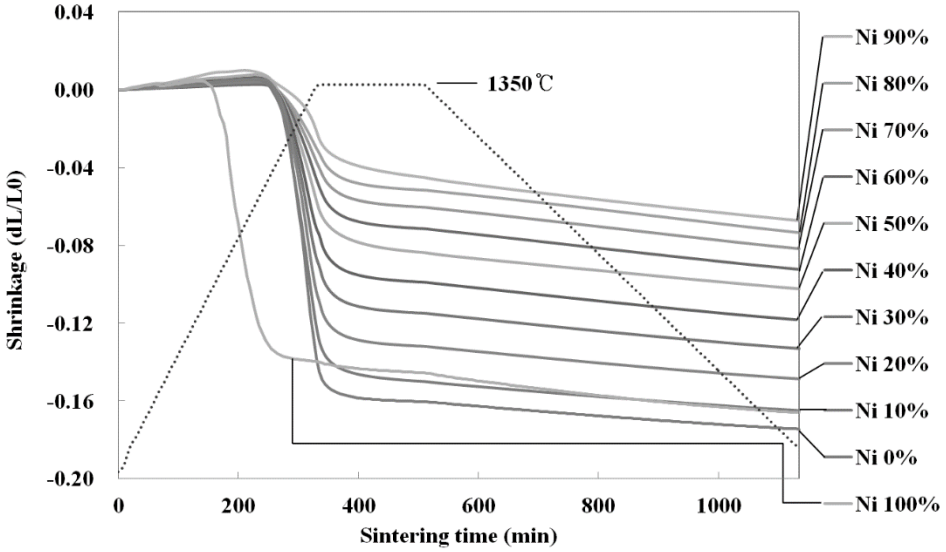

Figure 7.1 The measurement results of sintering shrinkage for the individual specimen of each layer of 0.16 ㎛ Al_2O_3 + 3.0 ㎛ Ni FGM and sintering temperature curve

7.2 Fitting model for sintering shrinkage of individual specimens of each layer of the FGM

In this study, a prediction model of sintering shrinkage for each layer of a FGM was devised using the fitting curve obtained by measuring the sintering shrinkage of individual specimens of each layer of the FGM. This fitting curve was termed the shrinkage fitting parameter (SFP).

The prediction model is defined as a function of volume fraction of a material. Thus, when a sintered-body having the same powder processing and the same sintering conditions is manufactured in the same way as other volume fractions of a material, it is possible to predict the shrinkage of the sintered-body.

The sintering shrinkage graph shown in Figure 7.2 is classified into four sections, depending on changing sintering shrinkage.

In Section 1-1, it is considered the “Expanding section” in the study. In this area, the specimen expands in correlation with the temperature rise.

In Section 1-2, known as the “Short-time shrinkage section,” the specimen rapidly shrinks in the short length of time until sintering temperature reaches 1350℃.

In Section 2, termed the “Stabilizing section”, the sintering shrinkage is stable, maintaining a sintering temperature of 1350℃ for 3 hours.

In Section 3, known as the “Long-time shrinkage section”, the specimen slowly shrinks when the sintering temperature decreases at a rate of 2℃ per minute. Sintering shrinkage is not great in this section. However, particles bond by sintering until Section 2 receives the thermal residual stress during the temperature cooling process.

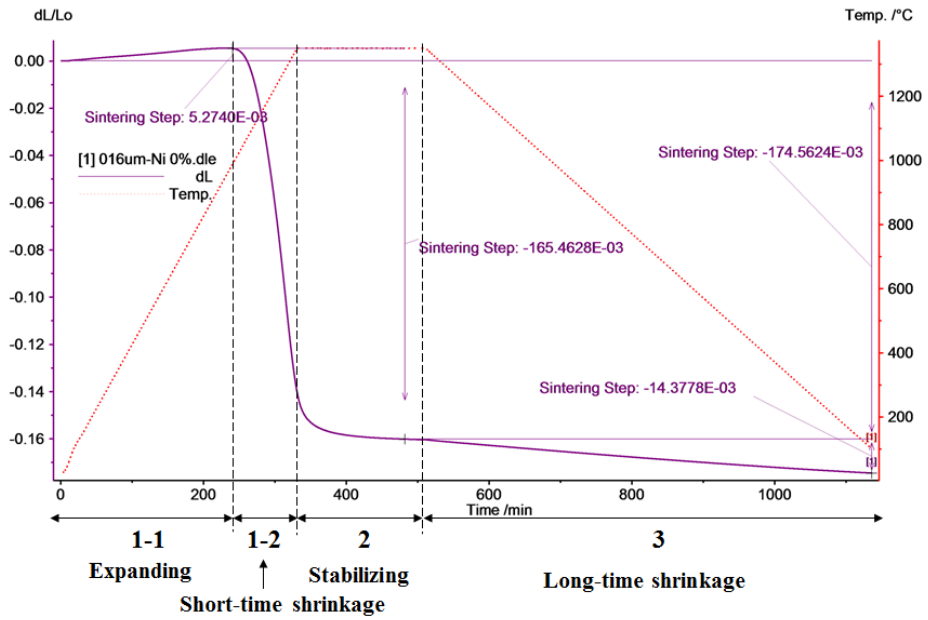

Figure 7.2 The measurement results of the sintering shrinkage of 100% Al_2O_3 with 0.16 ㎛ average particle size, showing definitions of sections

In Section 1-1 (Expanding), the sintering shrinkage of specimens increases well, corresponding to temperature rise. However, this increase is very small when compared with the total strain. Therefore, it does not have a significant effect on the final shape of the specimen.

Sintering shrinkage was begun at approximately the same temperature except for 100% Ni, as shown in Figure 7.1. Therefore, sintering shrinkage of specimens from 10 vol.% Ni + 90 vol.% Al_2O_3 to 90 vol.% Ni + 10 vol.% Al_2O_3 were approximated, as was the shrinkage of 100% Al_2O_3 in Section 1-1, as Equation (7.1). The slope of the strain of all specimens except 100% Ni are similar. Thus, the prediction model of Section 1-1 was constructed based on the slope of 100% Al_2O_3 as Equation (7.2).

$$SFP(Ni_x) = 1 \tag{7.1}$$

$$\varepsilon_s(Ni_x)_{1\ldots n}^{1-1} = \varepsilon_s(Ni_0)_{1\ldots n}^{1-1} * SFP(Ni_x) \tag{7.2}$$

where ε_s is sintering shrinkage (DL/L0), subscript x is the volume fraction of nickel from 10 vol.% Ni + 90 vol.% Al_2O_3 to 90 vol.% Ni + 10 vol.% Al_2O_3 (0.1~0.9), superscript 1-1 signifies Section 1-1, subscript $1 \ldots n$ identifies a continuous time (1 is the first time of the interval, n is the last time of the interval in the section), Ni_0 represents 100% Al_2O_3, and SFP is the shrinkage fitting parameter.

The value of the sintering shrinkage of 100% Al_2O_3 was measured previously, as shown in Figure 7.1. The value of SFP was also defined as

Equation (7.1). Therefore, $\varepsilon_s(Ni_x)_{1\ldots n}^{1-1}$ of Equation (7.2) was calculated as shown in Figure 7.4.

In Section 1-2 (Short-time shrinkage), the specimen including the Al_2O_3 particle rapidly shrinks in the short amount of time until the sintering temperature is reached at 1350℃. The greatest shrinkage was present for 10 vol.% Al_2O_3, and the sintering shrinkage of the specimen decreased corresponding to the increasing volume fraction of nickel. The ratio to be decreased was determined using a sintering shrinkage measurement of 10 vol.% Ni + 90 vol.% Al_2O_3, 50 vol.% Ni + 50 vol.% Al_2O_3, and 90 vol.% Ni + 10 vol.% Al_2O_3, as shown in Figure 7.3. Then, the *SFP* used in Section 1-2 as Equation (7.3) was determined by the curve fitted using values of this measurement. The sintering shrinkage in Section 1-2 as Equation (7.4) was determined by $SFP(Ni_x)$, as shown in Figure 7.3, and sintering shrinkage of 100% Al_2O_3, as revealed in Figure 7.4. The designation of M_Ni 90% in Figure 7.4 signifies measured sintering shrinkage of 90 vol.% Ni + 10 vol.% Al_2O_3, and P_Ni 90% is the predicted sintering shrinkage of 90 vol.% Ni + 10 vol.% Al_2O_3 by the prediction model proposed in the study.

$$SFP(Ni_x) = 0.7375\left(V_{Ni_x}\right)^2 - 1.62V_{Ni_x} + 1.0456 \tag{7.3}$$

$$\varepsilon_s(Ni_x)_{1\ldots n}^{1-2} = \varepsilon_s(Ni_0)_{1\ldots n}^{1-2} * SFP(Ni_x) \tag{7.4}$$

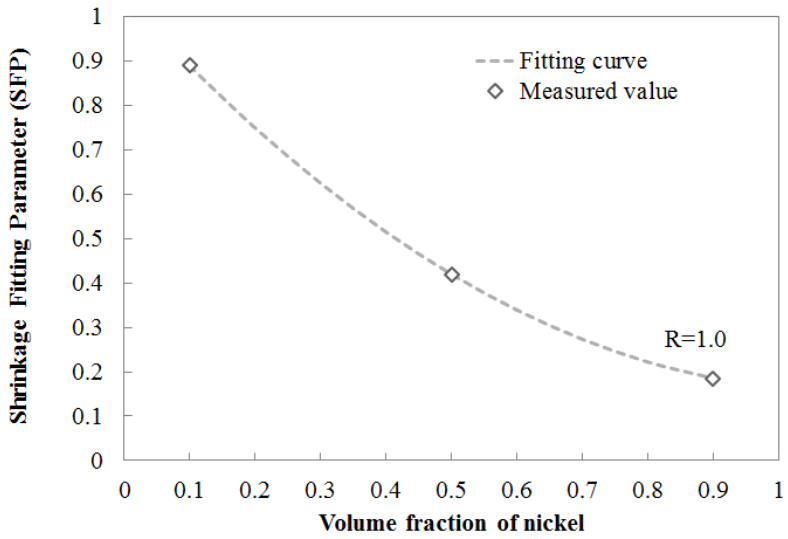

Figure 7.3 The shrinkage fitting parameter graph in Section 1-2

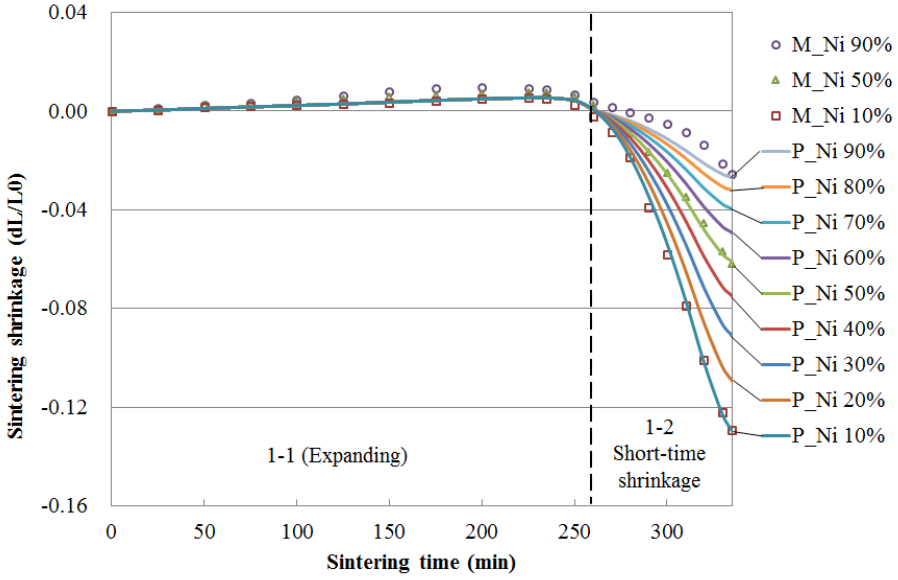

Figure 7.4 The prediction results in Section 1-1 and 1-2, and the measurement results of specific layers of the FGM

In Section 2 (Stabilizing), the sintering shrinkage is stable over a maintained sintering temperature of 1350℃ for 3 hours.

The *SFP*, the curve fitted by measured sintering shrinkages of 10 vol.% Ni + 90 vol.% Al_2O_3, 50 vol.% Ni + 50 vol.% Al_2O_3, and 90 vol.% Ni + 10 vol.% Al_2O_3, as shown in Figure 7.5, was used in Section 2 as Equation (7.5).

Sintering shrinkage of Section 1-2 and 100% Al_2O_3 were already a known value. Therefore, $\varepsilon_s(Ni_x)_{1\ldots n}^{2}$ of Equation (7.6) was able to be calculated, as shown in Figure 7.6. In addition, Equation (7.6) was expanded as Equation (7.7) for easier calculation.

$$SFP(Ni_x) = 0.2752\left(V_{Ni_x}\right)^{-0.921} \tag{7.5}$$

$$\varepsilon_s(Ni_x)_{1\ldots n}^{2} = \varepsilon_s(Ni_x)_{n}^{1-2} \Big/ \left\langle \left[\frac{\varepsilon_s(Ni_0)_{n}^{1-2}}{\varepsilon_s(Ni_0)_{1\ldots n}^{2}}\right] - \left\{\left[\frac{\varepsilon_s(Ni_0)_{n}^{1-2}}{\varepsilon_s(Ni_0)_{n}^{2}}\right] - \left[\frac{\varepsilon_s(Ni_0)_{n}^{1-2}}{\varepsilon_s(Ni_0)_{1\ldots n}^{2}}\right]\right\} / SFP(Ni_x) \right\rangle \tag{7.6}$$

$$\varepsilon_s(Ni_x)_{1\ldots n}^{2} = \varepsilon_s(Ni_x)_{n}^{1-2} \Big/ \left\langle \left\{\left[\frac{\varepsilon_s(Ni_0)_{n}^{1-2}}{\varepsilon_s(Ni_0)_{1\ldots n}^{2}}\right]\left(1 + \frac{1}{SFP(Ni_x)}\right)\right\} - \left(\frac{1}{SFP(Ni_x)}\right) \right\rangle \tag{7.7}$$

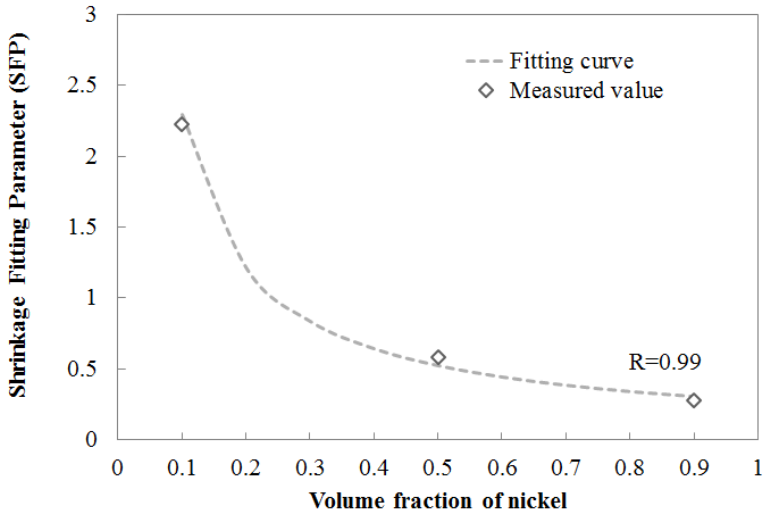

Figure 7.5 The shrinkage fitting parameter graph in Section 2

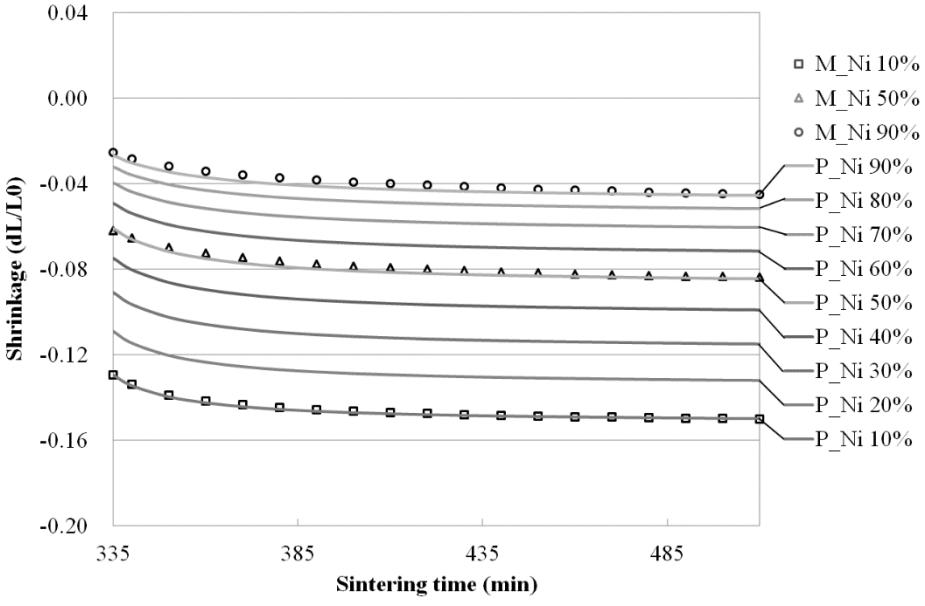

Figure 7.6 The prediction results in Section 2 and the measurement results of specific layers of the FGM

In Section 3 (Long-time shrinkage), the specimen slowly shrinks as sintering temperature decreases at a rate of 2℃ per minute. The prediction model of sintering shrinkage in this section has a similar form to the model in Section 2.

The *SFP* of Section 3, as shown in Figure 7.7, was defined as Equation (7.8). Sintering shrinkage of Section 2 and 100% Al_2O_3 was already known. Therefore, $\varepsilon_s(Ni_x)_{1\ldots n}^3$ of Equation (7.8) was calculated as shown in Figure 7.8.

$$SFP(Ni_x) = 0.2735\left(V_{Ni_x}\right)^{-1.386} \tag{7.8}$$

$$\varepsilon_s(Ni_x)_{1\ldots n}^3 = \varepsilon_s(Ni_x)_n^2 \,/\, \langle\left\{\left[\frac{\varepsilon_s(Ni_0)_n^2}{\varepsilon_s(Ni_0)_{1\ldots n}^3}\right]\left(1+\frac{1}{SFP(Ni_x)}\right)\right\} - \left(\frac{1}{SFP(Ni_x)}\right)\rangle \tag{7.9}$$

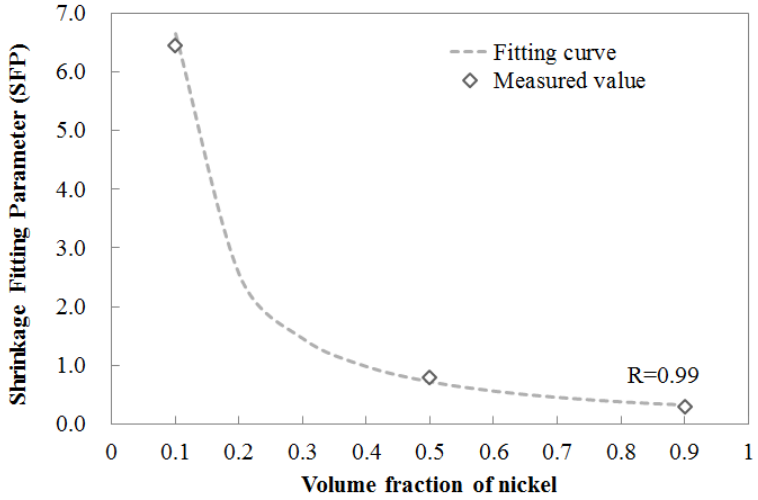

Figure 7.7 The shrinkage fitting parameter graph in Section 3

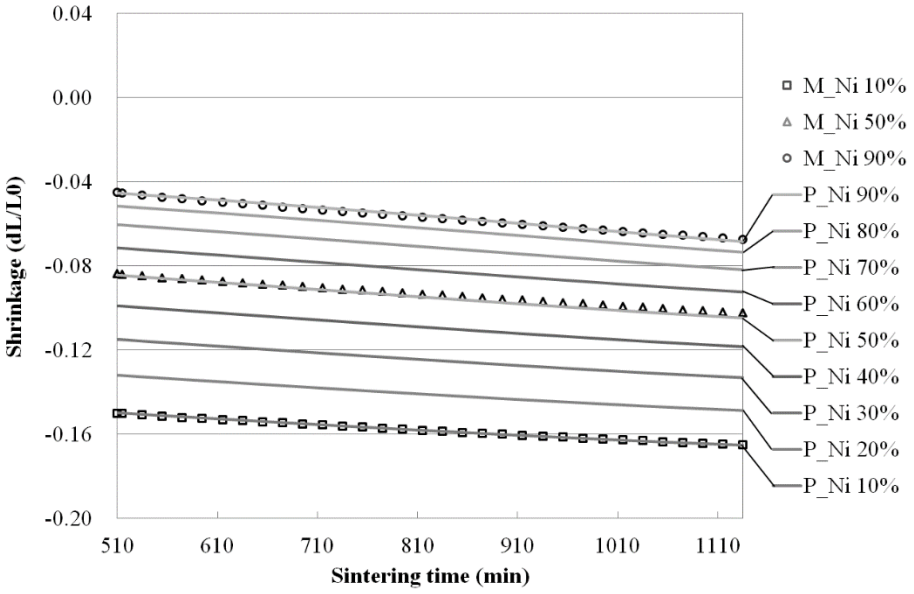

Figure 7.8 The prediction results in Section 3 and the measurement results of specific layers of the FGM

The sintering shrinkage predicted by the prediction model proposed in the study and the measured sintering shrinkage for all the layers consisting of 0.16 ㎛ Al_2O_3 + 3.0 ㎛ Ni FGM is illustrated in Figure 7.9. For 90 vol.% Ni of Section 1-1, Section 1-2, and Section 2, a slight error occurred between the predicted value and the measured value. However, generally, the value of the proposed model compared well with the measured value. Accordingly, the prediction model is determined to be reliable.

Therefore, the sintering shrinkage of 1.0 ㎛ Al_2O_3 + 3.0 ㎛ Ni FGM was predicted in the same way, and it produced the results shown in Figure 7.10.

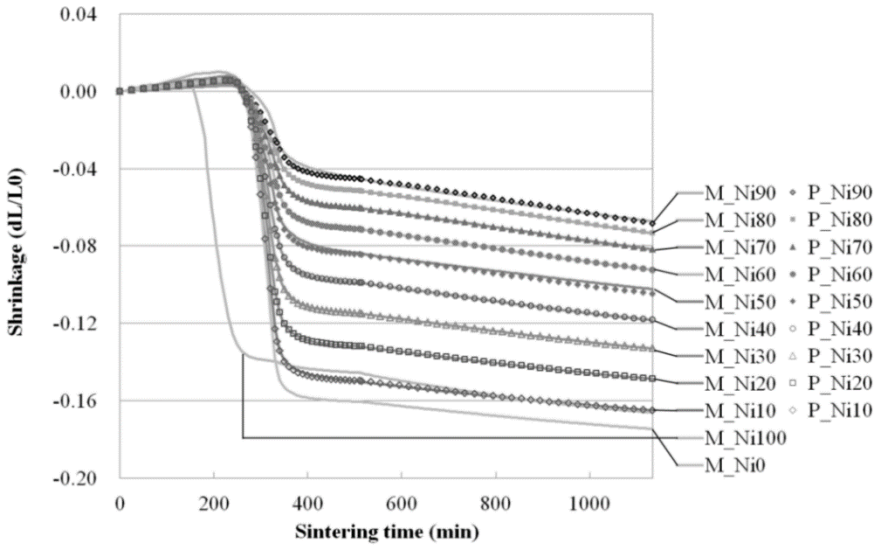

Figure 7.9 The measurement results of 0.16 ㎛ Al_2O_3 + 3.0 ㎛ Ni FGM and the prediction results of specific layers of the FGM

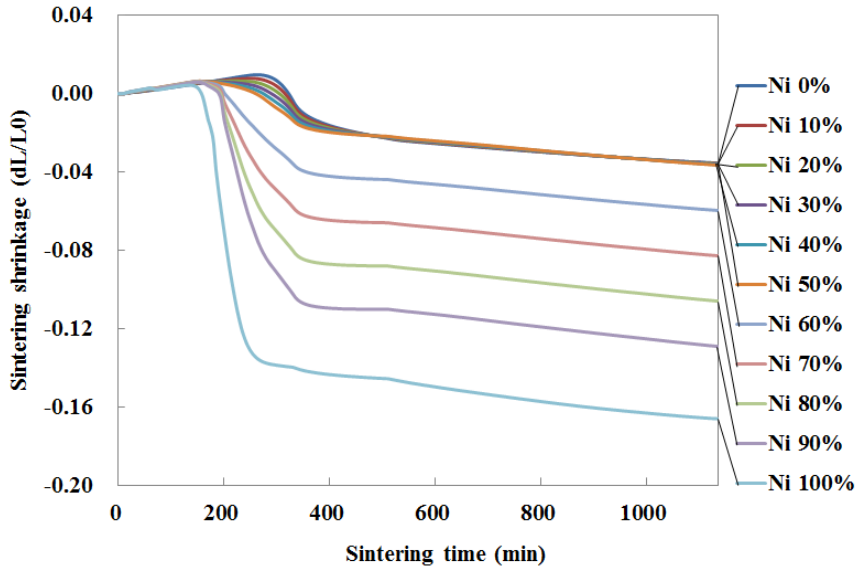

Figure 7.10 The prediction results of 1.0 ㎛ Al_2O_3 + 3.0 ㎛ Ni FGM and the measurement results of specific layers of the FGM

Chapter 8. Sintering behavior of FGM fabricated by pressureless sintering method

8.1 Temperature dependent material properties

To analyze the sintering behavior of the FGM, material properties relating to the temperature were required. The FGM fabricated in the study was sintered at 1350℃. Therefore, there is a need for material properties in the range of Ni and Al_2O_3 to 1350℃ at room temperature. The material properties corresponding to temperature in the previous studies were quoted in this study.

A large amount of research into the elastic modulus of nickel, corresponding to temperature, has been conducted in the mid-20th century. These studies were organized by Ledbetter and Reed [89], as shown in Figure 8.1. The quoted value in this study is the value given in the paper written by Farraro and McLellan [90], as shown in Figure 8.2. However, the temperature range given in this paper is up to 1000℃. Thus, the study of Saunders *et al*. [91], as presented in Figure 8.3, was used to confirm the elastic modulus of nickel at 1350℃. The previous studies [90-94] reported as follows: the melting point of pure nickel is 1453℃. Thus, this material tends to decrease suddenly in fraction solid at about 1300℃. Therefore, a rapid decrease in elastic modulus of the material from this point was observed.

The value of elastic modulus of alumina corresponding to temperature by Latellaw and Liu [92], as shown in Figure 8.4, was quoted.

Poisson's ratio, depending on temperature, was referenced in the literature [89, 95]. Poisson's ratio confirmed that there are no significant changes corresponding to temperature for both nickel and alumina, as shown in Figure 8.5. Therefore, in this study, it was assumed that Poisson's ratio has a fixed value depending on temperature. The elastic modulus and Poisson's ratio according to temperature is shown in Figure 8.6.

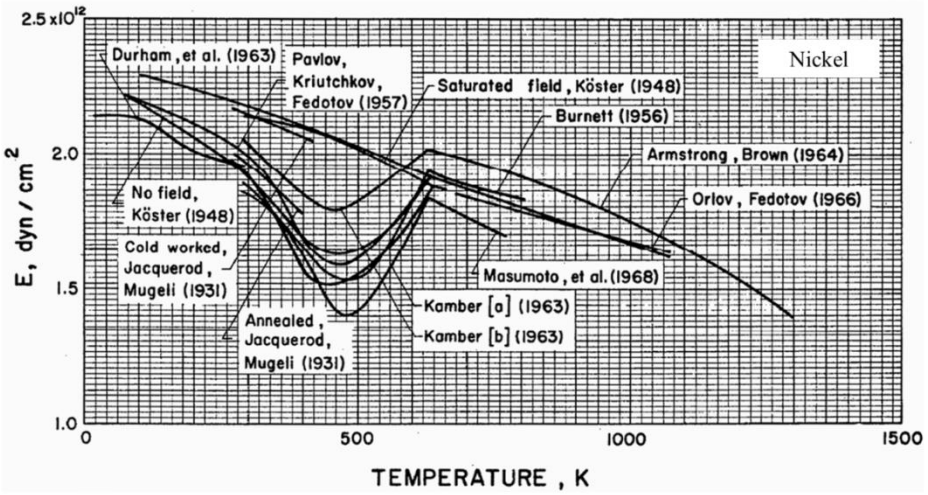

Figure 8.1 Summary of measured results of elastic modulus of nickel corresponding to temperature [89]

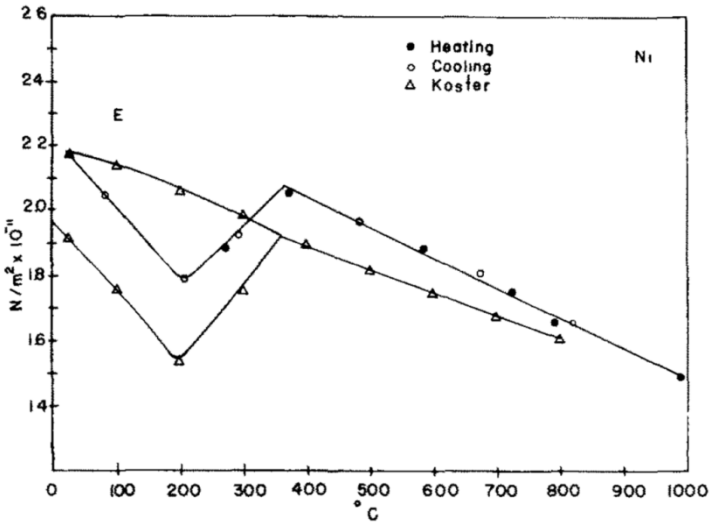

Figure 8.2 The quoted elastic modulus of nickel, corresponding to temperature (25-1000℃) [90]

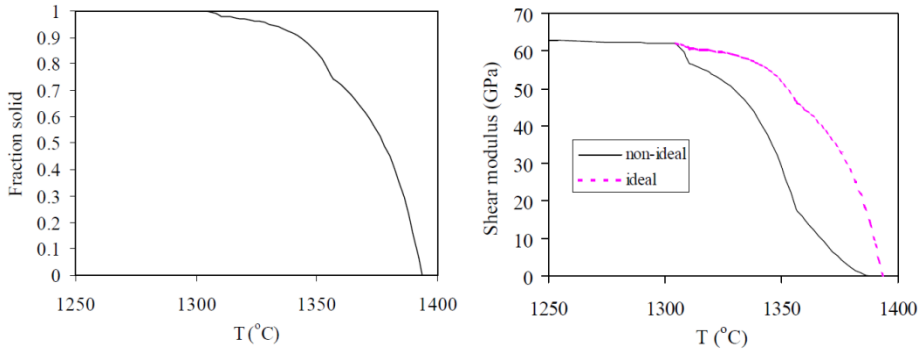

Figure 8.3 Variation of fraction solid and shear modulus at high temperature (1250-1400℃) [91]

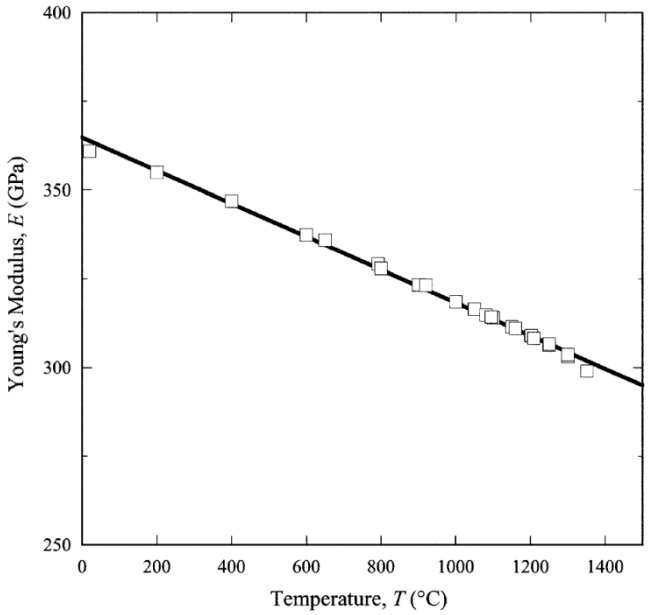

Figure 8.4 The quoted elastic modulus of alumina corresponding to temperature [92]

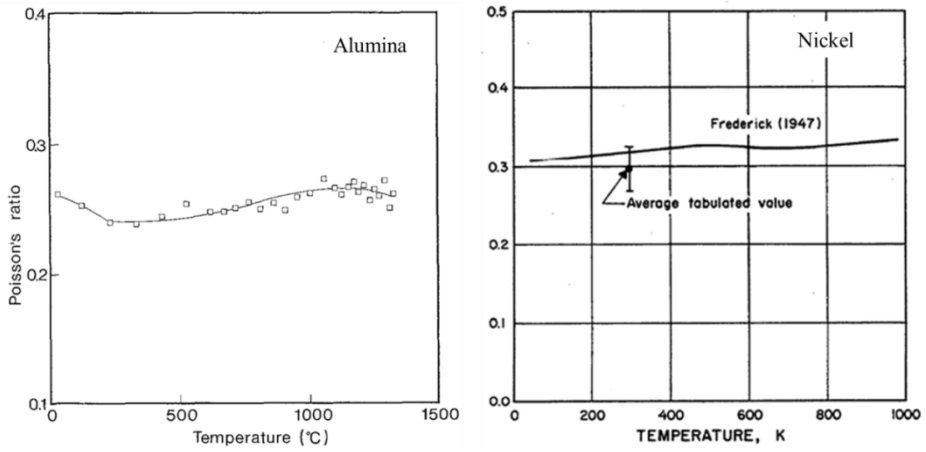

Figure 8.5 Poisson's ratio of nickel and alumina corresponding to temperature [99, 95]

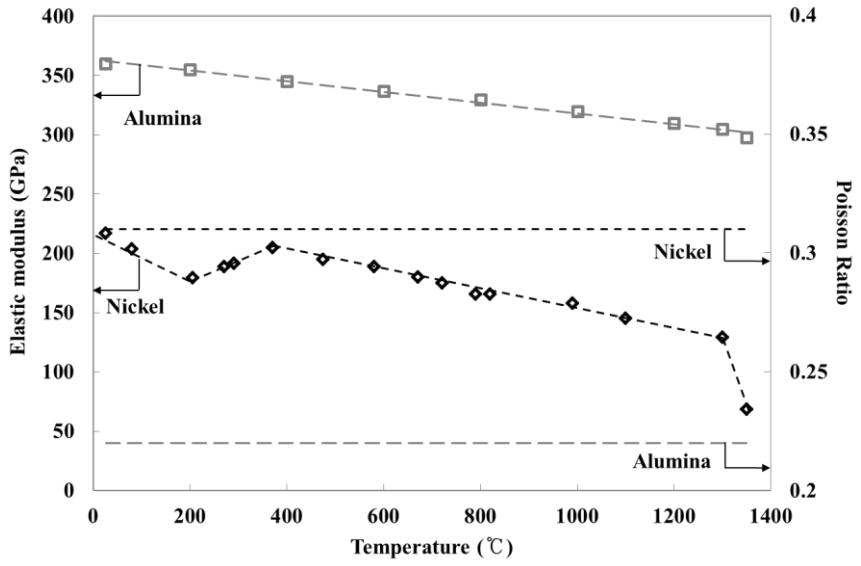

Figure 8.6 The elastic modulus and Poisson's ratio of nickel and alumina used in the study

8.2 Analysis for sintering deformation

The sintering deformation of the FGM layers was computed using the finite element method (FEM): ANSYS APDL. A two-dimensional four-node plane element (PLANE42) was used in the ANSYS APDL. The two-dimensional axisymmetric model was meshed using 0.1 mm elements, as shown in Figure 4.2. The temperature was cooled from 1350℃ to 25℃.

The measured values throughout the experiments and the values estimated by the proposed models in the study were employed in the sintering deformation analysis of 0.16 ㎛ Al_2O_3 + 3.0 ㎛ Ni FGM using the finite element method, as shown in Table 8.1.

The analysis model using the measured values throughout the experiments was not able to measure the elastic modulus at 1350℃ into each layer of the FGM. Thus, porosity of each layer of the FGM at 1350℃ was calculated using the measured sintering shrinkage. Then, the calculated porosity was put into the proposed model to estimate the elastic modulus at 1350℃ as follows.

The porosity of each layer of the FGM at 1350℃ (P_{1350}) was computed using theoretical true density (ρ_{TTD}) and the density of each layer of the FGM at 1350℃(ρ_{1350}), as shown in Equation (8.1).

$$P_{1350} = \frac{\rho_{TTD} - \rho_{1350}}{\rho_{TTD}} \tag{8.1}$$

Because the mass (weight) of powder inserted in the FGM does not

change with temperature, Equation (8.1) can be expressed as Equation (8.2).

$$P_{1350} = 1 - \frac{m}{V_{1350} \cdot \rho_{TTD}} \tag{8.2}$$

where the volume of each layer of the FGM at 1350℃(V_{1350}) can be calculated using the measured sintering shrinkage and the volume at 25℃ as Equation (8.3).

$$V_{1350} = V_{25}(1 + \varepsilon_s)^3 \tag{8.3}$$

The mass at 25℃ was expressed as Equation (8.4).

$$m = (1 - P_{25}) \cdot V_{25} \cdot \rho_{TTD} \tag{8.4}$$

The Equation (8.5) was formulated by substituting Equations (8.3) and (8.4) into Equation (8.2). Equation (8.5) can be calculated for the porosity of each layer of the FGM at 1350℃ using the porosity at 25℃ and the measured sintering shrinkage.

$$P_{1350} = 1 - \frac{(1 - P_{25})}{(1 + \varepsilon_s)^3} \tag{8.5}$$

The porosity calculated by Equation (8.5) and the material properties corresponding to temperature in Figure 8.6 were used in Equations (6.19 -

6.21), which are the proposed model in chapter 6.3 of the study. Finally, the elastic modulus of each layer of 0.16 ㎛ Al_2O_3 + 3.0 ㎛ Ni FGM at 1350℃ were estimated.

Table 8.1 Classification of material properties used in sintering deformation analysis of 0.16 ㎛ Al_2O_3 + 3.0 ㎛ Ni FGM

	Analysis model using the measured values (M_Model)	Analysis model using the estimated values (P_Model)
Elastic modulus (using Voigt model)	Figure 6.9 Chapter 8.2	Equation (6.21) Figure 8.6
Poisson's ratio	Figure 8.6	Equation (6.19)
Sintering shrinkage	Figure 7.1	Equation (7.7), Equation (7.9)

8.3 Result comparison for sintering deformation analysis

The primary sintering mechanism of the green-body of the FGM is completed almost in the end step of Second 2 in the definition of the section of sintering shrinkage as Figure 7.2. Thus, sintering deformation of the specimen is large, and internal stress of the specimen is the lowest at this time.

Over time, analysis models using the measured values (M_Model) and using the estimated values (P_Model) were conducted for sintering deformation analysis. These results are presented in Figure 8.7. The maximum displacement of M_Model was 2.49629 mm, and the maximum displacement of P_Model was 2.49389 mm. The maximum displacement of the two models are identical to 10 ㎛.

The end step of Section 3 is completed perfectly for the sintering mechanism of the green-body of the FGM. In this section, the specimen is slowly shrunk when the sintering temperature decreases at a rate of 2℃ per a minute, and sintering shrinkage of the specimen is not large. However, particles bond by sintering until Section 2 receives the thermal residual stress of temperature cooling.

For the end step of Section 3, analysis results of models using the measured values (M_Model) and using the estimated values (P_Model) for sintering deformation analysis are shown in Figure 8.8. The maximum displacement of the M_Model was 0.395 mm, and the maximum displacement of the P_Model was 0.399 mm. Error between the maximum displacements of the two models was 0.98%.

Analysis results of models using the measured values (M_Model) and using the estimated values (P_Model) and the measured result of 0.16 ㎛ Al_2O_3 + 3.0 ㎛ Ni FGM are compared in Figure 8.9. Error between analysis and measured values of the 100% Al_2O_3 layer was 1.2%. By the time the volume fraction of the nickel was 70 vol.%, error between the two values was maintained at the level of the 100% Al_2O_3 layer. Meanwhile, when the volume fraction of the nickel was 90 vol.%, the error between the two values was increased up to 3.9%. However, this error is determined to be a reasonable value because the result analyzed by the finite element method has an error generated by numerical integration error, and the measured result has an error that occurs when the material properties are measured.

Figure 8.10 is a diagram showing the same scale analysis results of the P_Model in the cross-section of fabricated 0.16 ㎛ Al_2O_3 + 3.0 ㎛ Ni FGM.

Based on the comparison result, the proposed models in the study are determined to be reliable. Thus, the analysis model using estimated values of the proposed model (P_Model) is able to be used for the sintering deformation analysis instead of the analysis model using the measured value (M_Model).

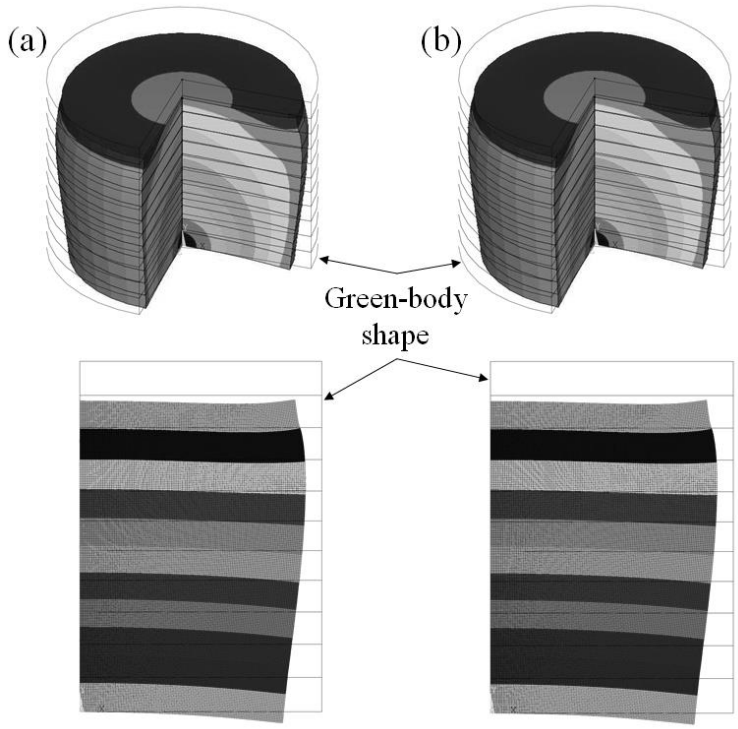

Figure 8.7 The results of sintering deformation analysis at 1350℃:

(a) the result of M_Model and (b) the result of P_Model

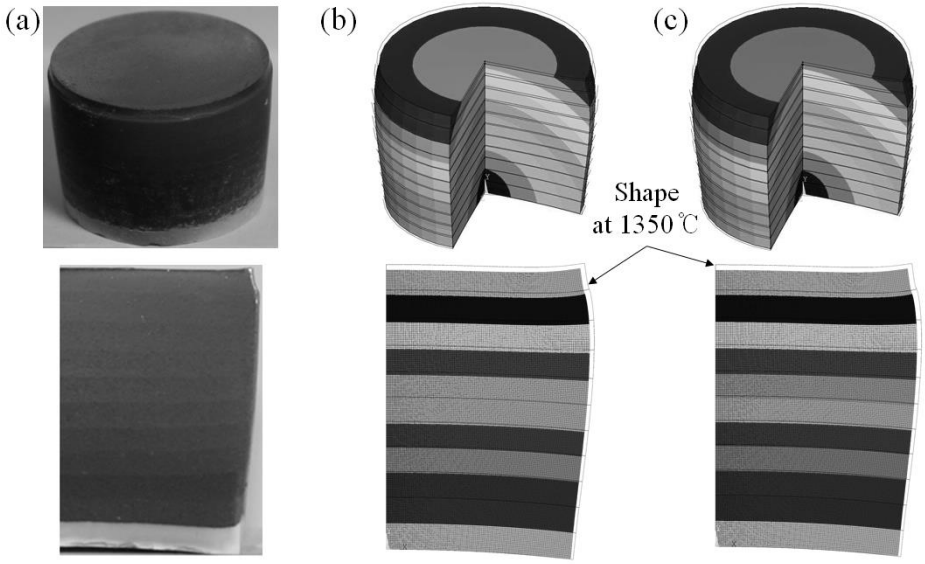

Figure 8.8 (a) fabricated 0.16 ㎛ Al_2O_3 + 3.0 ㎛ Ni FGM specimen, the results of sintering deformation analysis at 25℃ of Section 3: (b) the result of M_Model and (c) the result of P_Model

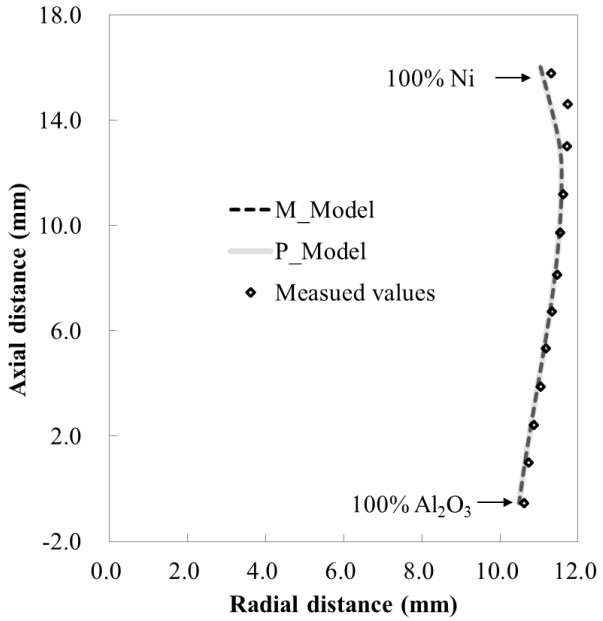

Figure 8.9 Comparison between the measured data of 0.16 ㎛ Al_2O_3 + 3.0 ㎛ Ni FGM and both model results on sintering deformation analysis at 25℃ of Section 3

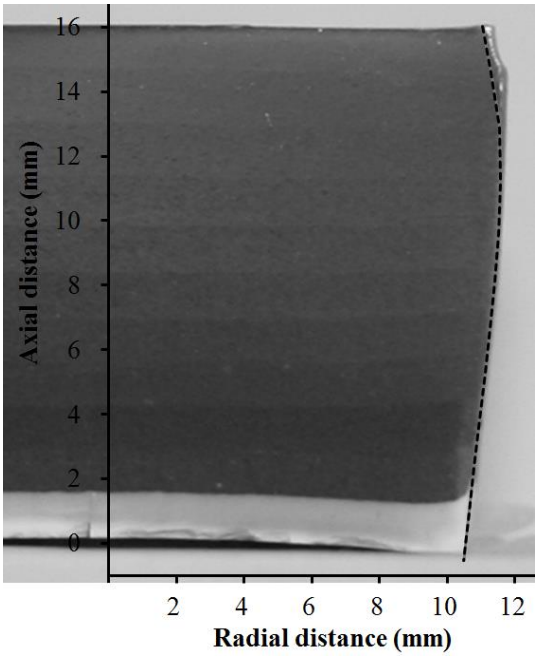

Figure 8.10 Compared diagram between the cross-section image of 0.16 ㎛ Al_2O_3 + 3.0 ㎛ Ni FGM and P_Model results on sintering deformation analysis at 25℃ of Section 3

8.4 Analysis of thermal residual stress on sintering process

To confirm the validity of the proposed model in the study, the thermal residual stresses of the FGMs were analyzed using the material properties estimated by the proposed models, and then the analysis results were compared with the estimated ultimate strength of the FGMs to predict any damage that may occur and the location of the damage. Finally, the predicted results were compared with the FGM.

The used elastic modulus, Poisson's ratio, and CTE were estimated by Equation (6.20), Equation (6.18), and Equation (7.9), respectively, and the values in Figure 6.14 in chapter 6.6 were used as tensile strength of the FGM. The FEM model used to analyze thermal residual stress was identical to the FEM model of sintering deformation analysis.

The FGM layer including nickel and alumina powder showed both a ductile and a brittle character. When a FGM including both a ductile and a brittle character has a brittle characteristic and receives a tensile load, a FGM is most vulnerable. Therefore, maximum tensile stress theory and maximum principal stress theory were used as failure criteria in the study. These failure criteria are applied generally for brittle materials.

A brittle material is generally weaker in tensile yield strength than in compressive yield strength. Therefore, maximum tensile stress theory can be applied to estimate failure:

$$\sigma_x \geq \sigma_{yt} \quad \text{OR} \quad \sigma_y \geq \sigma_{yt} \quad \text{OR} \quad \sigma_z \geq \sigma_{yt} \tag{8.6}$$

where σ_x, σ_y, and σ_z are radial, axial, and hoop stresses, respectively, and σ_{yt} is tensile yield strength or ultimate strength.

Maximum principal stress theory can be applied to estimate failure:

$$\sigma_1 \geq \sigma_{yt} \quad \text{OR} \quad \sigma_2 \geq \sigma_{yt} \quad \text{OR} \quad \sigma_3 \geq \sigma_{yt} \tag{8.7}$$

where σ_1, σ_2, and σ_3 are 1st principal, 2nd principal, and 3rd principal stresses, respectively, and σ_{yt} is tensile yield strength or ultimate strength. These formulas can be used to predict the onset of crack formation.

8.5 Result comparison on analysis of thermal residual stress

Maximum tensile stresses for 0.16 ㎛ Al_2O_3 + 3.0 ㎛ Ni FGM and 1.0 ㎛ Al_2O_3 + 3.0 ㎛ Ni FGM were calculated by ANSYS. These results were then compared with the estimated ultimate strength to confirm whether damage may occur, as shown in Figure 8.11 and Figure 8.12.

In the analysis result of 0.16 ㎛ Al_2O_3 + 3.0 ㎛ Ni FGM, radial stress and hoop stress were close to the ultimate strength boundary but did not exceed it, as shown in Figure 8.11. However, radial stress at the 60 vol.% Ni / 40 vol.% Al_2O_3 layer became higher than the ultimate strength in the analysis result of 1.0 ㎛ Al_2O_3 + 3.0 ㎛ Ni FGM, as shown in Figure 8.12.

Maximum principal stresses of the FGMs were also calculated and compared in the same process as shown in Figure 8.13 and Figure 8.14. In the analysis result of 0.16 ㎛ Al_2O_3 + 3.0 ㎛ Ni FGM, the 1st principal stresses at the 50 vol.% Ni / 50 vol.% Al_2O_3 layer and the 60 vol.% Ni / 40 vol.% Al_2O_3 layer were close to the ultimate strength boundary but did not exceed it, as shown in Figure 8.13. However, the 1st principal stresses at the 60 vol.% Ni / 40 vol.% Al_2O_3 layer and the 70 vol.% Ni / 30 vol.% Al_2O_3 layer became higher than the ultimate strength in the analysis result of 1.0 ㎛ Al_2O_3 + 3.0 ㎛ Ni FGM, as shown in Figure 8.14.

This analysis result predicted that a crack would be generated in the 60 vol.% Ni / 40 vol.% Al_2O_3 layer and the 70 vol.% Ni / 30 vol.% Al_2O_3 layer of 1.0 ㎛ Al_2O_3 + 3.0 ㎛ Ni FGM. Then, this prediction was agreed as the crack position of 1.0 ㎛ Al_2O_3 + 3.0 ㎛ Ni FGM, as shown in Figure 8.15.

Based on the comparison result, the proposed models in the study are determined to be reliable. Moreover, it is possible to conduct damage analysis of the FGM using the proposed models.

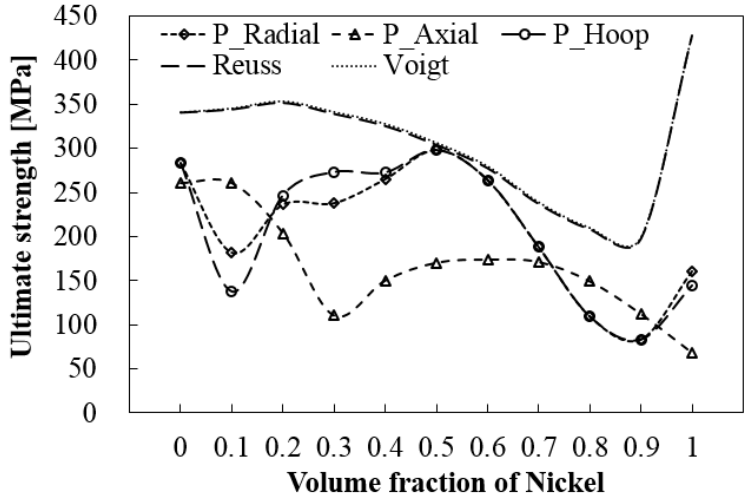

Figure 8.11 Comparison between the maximum tensile stresses and ultimate strength for 0.16 ㎛ Al_2O_3 + 3.0 ㎛ Ni FGM

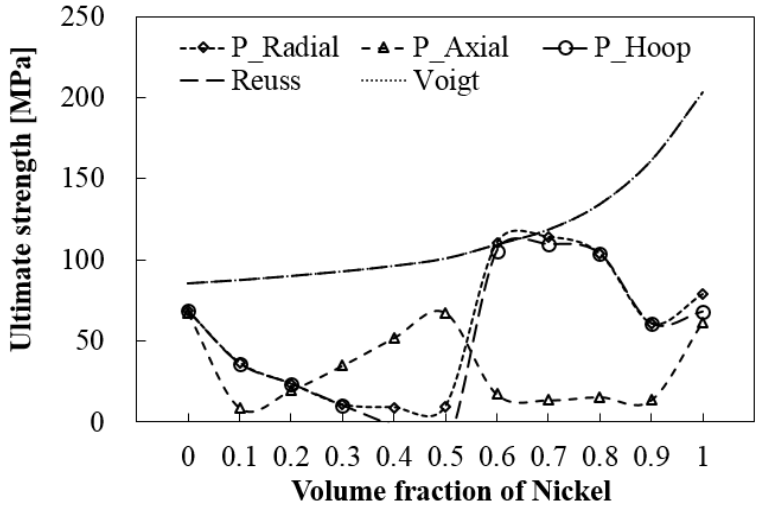

Figure 8.12 Comparison between the maximum tensile stresses and ultimate strength for 1.0 ㎛ Al_2O_3 + 3.0 ㎛ Ni FGM

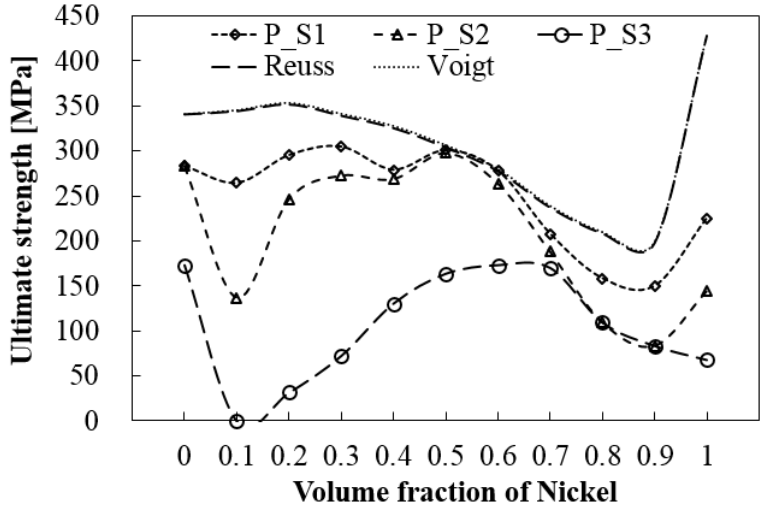

Figure 8.13 Comparison between the maximum principal stresses and ultimate strength for 0.16 ㎛ Al_2O_3 + 3.0 ㎛ Ni FGM

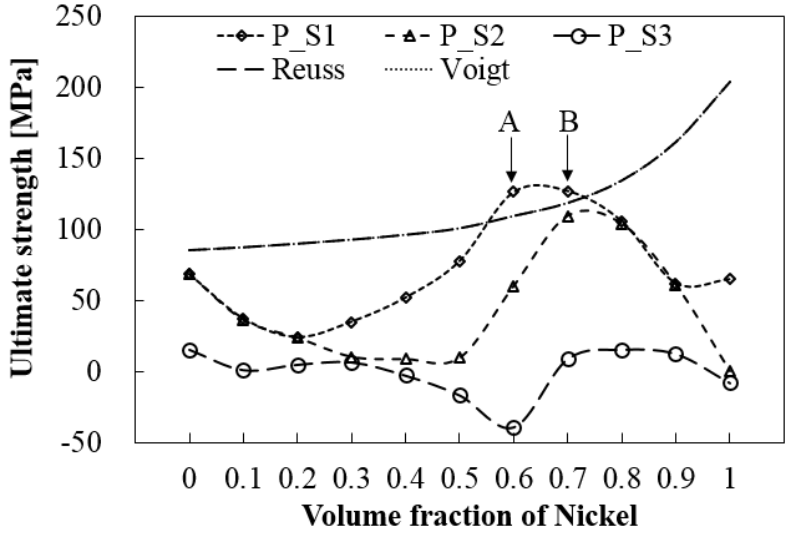

Figure 8.14 Comparison between the maximum principal stresses and ultimate strength for 1.0 ㎛ Al_2O_3 + 3.0 ㎛ Ni FGM

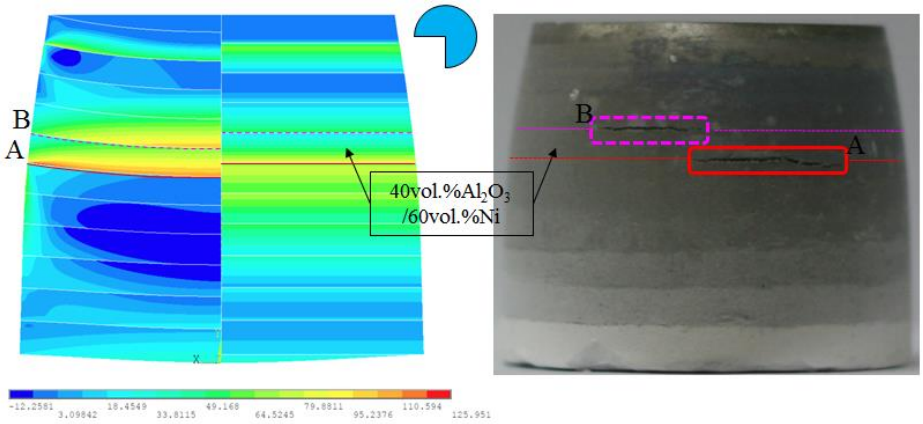

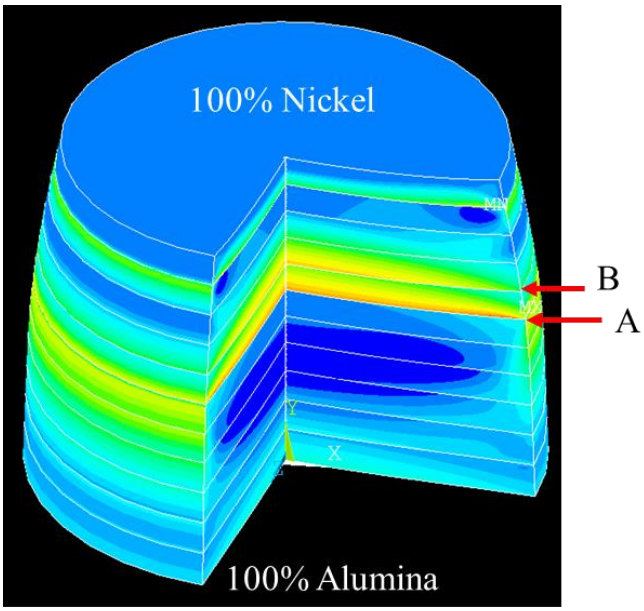

Figure 8.15 Comparison between crack positions of the analysis result and fabricated 1.0 ㎛ Al_2O_3 + 3.0 ㎛ Ni FGM

Chapter 9. Conclusion

The research and development of industrial materials is a constantly evolving fields with new material improved materials being steadily developed. Nevertheless, modern machine parts are used in complicated conditions and severe environment, and require to be optimized simultaneously for a number of functions and environmental conditions.

Currently, in order to meet these needs, instead of a single material, composite material combining a suitable material for their needs is being developed rapidly. Composite materials have improved properties through the careful selection of the characteristics of the different materials. However, these composite materials have disadvantages that the interface between the materials and components can be separated by the residual stress caused by differences of the coefficient of thermal expansion, lattice constant, physicochemical properties and others. To overcome this disadvantages and to improve bonding strength at the interface, FGMs have been developed.

In this study, a heat-resistant material is developed to increase the operating temperature as a strategy for increasing the thermal energy efficiency. To do so, the use of FGMs is introduced. As a heat shielding material, alumina was used, and nickel was employed as the structural material of the FGM. The powder metallurgy process and the pressureless sintering method were used for efficient and cost-efficient manufacturing of the FGM.

To allow mechanical engineers without a strong background in material science to develop FGM parts, a system making use of a material science database was required. To make this system, the variables to be considered for the design and fabrication of FGMs from the materials science field should be input into the database; the experiments required from the materials science field should be standardized; and the number of required experiment should be reduced.

A measurement method and estimated models of material properties including the following have been studied in the thesis.

1. A measurement method of porosity for each layer of a FGM:

To devise a method with higher accuracy than conventional measurement methods, a method using the individual specimen of each layer of a FGM and a method using Image Processing of MATLAB were suggested. It was determined by the experimental result that the method using Image Processing is more suitable for measurement of the porosity of each layer of the FGM than the method using the individual specimens.

2. A method and a model to estimate material properties depending on porosity for the fabricated nickel/alumina FGM:

A study on property estimation of the composite that include the two materials and the pores together, such as the FGM of this study, has not yet begun. Therefore, three new models are proposed to estimate

elastic modulus of the fabricated FGM. Elastic modulus values calculated according to each of the aforementioned models were compared to values measured by the micro indenter for the FGM. In the results, the first and second models exhibited significant differences with the experimental measurements. In contrast, the third model yielded values within the error range of those measured with the micro indenter. Therefore, the ultimate strength of each layer of the FGM was estimated using the third model, which was proposed and verified in elastic modulus.

3. A method and a model to predict sintering shrinkage of each layer of a FGM:

A method to reduce the time and cost of sintering shrinkage measurement effectively was devised using the material property characteristics of FGMs. This method measured the sintering shrinkage of individual specimens of specific layers making up the FGM. Then, a fitting curve of measured values was made. Using this fitting curve, the sintering shrinkage of individual specimens of the other layers, which are not measured, and which make up the FGM, can be estimated.

A precise measurement method for the porosity of the FGM, an estimation method for the material properties depending on porosity of the FGM, and an estimation model that can predict the sintering shrinkage with a minimal

number of experiments are suggested in this study as basic research for the development of a database of the materials science field. To confirm the reliability of the estimation model, an analysis of the results using estimated values from the estimation model were compared with measured values of fabricated FGMs. The proposed estimation models in the study are determined to be reliable using the comparison results.

When a mechanical engineer who designs and fabricates a FGM uses the database employing basic data made by this study, it is possible to predict the stress and displacement of the FGM. Finally, a FGM providing excellent performance can be manufactured using this database system.

Chapter 10. Bibliography

[1] D. M. Hulbert, D. Jiang, D. V. Dudina, amd A. K. Mukherjee, "The synthesis and consolidation of hard materials by spark plasma sintering," *Int. Journal of Refractory Metal & Hard Materials*, Vol. 27, pp. 367-375, 2009.

[2] http://fgmdb.kakuda.jaxa.jp/e_index.html

[3] http://www.geo.ucalgary.ca/~macrae/t_origins/carbbones/dinobone .html

[4] http://www.3dham.com/microgallery/bamboo.html

[5] J. L. Pelletier, "Thermoelastic Analysis and Optimization of Functionally Graded Plates and Shells," *Thesis in The graduated school of The University of Maine*, 2005.

[6] J. C. Lee, J. H. Park, S. H. Ryu, H. J. Hong, D. H. Riu, S. H. Ahn, and C. S. Lee, "Reduction of functionally graded material layers for Si_3N_4-Al_2O_3 system using 3-dimensional modeling," *Materials Transactions*, Vol. 49, No. 4, pp. 829-834, 2008.

[7] J. H. Park, S. H. Ryu, C. S. Lee, Y. H. Choa, J. C. Lee, and S. H. Ahn, "Fabrication and Simulation of a Ni-Al_2O_3 Crack Free Joining for Multiple Metal-Ceramic Composites Using a New Functionally Graded Material (FGM) Method," *Advanced Materials Research*, Vol. 47-50, pp. 523-527, 2008.

[8] S. H. Ryu, J. H. Park, C. S. Lee, J. C. Lee, S. H. Ahn, J. H. Chae, and D. H. Riu, "Optimization of Crack-Free Polytypoidally Joined Si_3N_4-Al_2O_3 Functionally Graded Materials (FGM) Using 3-Dimensional Modeling," *Advanced Materials Research*, Vol. 47-50, pp. 494-498,

2008.

[9] J. H. Park, J. C. Lee, S. H. Ryu, K. B. Jung, H. B. Song, J. C. Yun, Y. H. Choa, S. H. Ahn, and C. S. Lee, "Crack-free joint in a Ni-Al_2O_3 FGM system using three-dimensional modeling," *Materials Transactions*, Vol. 50, No. 7, pp. 1875-1880, 2009.

[10] S. H. Ryu, J. H. Park, C. S. Lee, J. C. Lee, S. H. Ahn, and S. T. Oh, "Experimental measurement of coefficient of thermal expansion for graded layers in Ni-Al_2O_3 FGM joints for accurate residual stress analysis," *Materials Transactions*, Vol. 50, No. 6, pp. 1553-1557, 2009.

[11] R. W. Davidge, " The Mechanical properties and design data for engineering ceramics," *Ceramics International*, Vol. 1, pp. 75, 1975.

[12] A. Goupee, "Methodology for the Thermomechnical Simulation and Optimization of Functionally Graded Materials", *Thesis in The graduated school of The University of Maine*, 2005.

[13] W. Voigt, "Über die Beziehung Zwischen den Beiden Elasticitäts-Constanten Isotroper Körper," *Annalen der Physik and Chemie*, Vol. 38, pp.573-587, 1889.

[14] I. Tamura, Y. Tomota, and M. Ozawa, "Strength and ductility of Fe-Ni-C alloys composed of austenite and martensite with various strength," *Proceedings of the 3rd International Conference on Strength of Metals and Alloys (Institute of Metals, and Iron and Steel Institute, London 1973)*, Vol. 1, pp.611-615, 1973.

[15] Z. Fan, P. Tsakiropoulos, and A. P. Miodownik, "A generalized law of

mixtures," *Journal of Materials Science*, Vol. 29, pp.141-150, 1994.

[16] T. Mori and T. Tanaka, "Average stresses in matrix and average elastic energy of materials with misfitting inclusions," *Acta Metallurgica*, Vol. 21, pp. 571-574, 1973.

[17] R. Hill, "A self-consistent mechanics of composite materials," *Journal of the Mechanics and Physics of Solids*, Vol. 13, pp. 213-222, 1965.

[18] Y. Benveniste, "A new approach to the application of Mori-Tanaka's theory in composite materials," *Mechanics of Materials*, Vol. 6, pp.147-157, 1987.

[19] T. Reiter, G. J. Dvorak, and V. Tvergaard, "Micromechanical models for graded composite materials," *Journal of the Mechanics and Physics of Solids*, Vol. 45, pp.1281-1302, 1997.

[20] T. Reiter and G. J. Dvorak, "Micromechanical models for graded composite materials: II. Thermomechanical loading," *Journal of the Mechanics and Physics of Solids*, Vol. 46, pp.1655-1673, 1998.

[21] H. Hatta and M. Taya, "Equivalent inclusion method for steady state heat conduction in composites," *International Journal of Engineering Science*, Vol. 24, pp.1159-1172, 1986.

[22] B. W. Rosen and Z. Hashin, "Effective thermal expansion coefficients and specific heats of composite materials," *International Journal of Engineering Science*, Vol. 8, pp.157-173, 1970.

[23] W. S. Slaughter, "The Linearized Theory of Elasticity," *Birkhäuser, Boston*, 2001.

[24] Z. Hashin, "Assessment of the self-consistent scheme approximation:

conductivity of composites," *Journal of Composite Materials*, Vol. 2, pp.284-300, 1968.

[25] A. M. Nikolenko, "Concept of a hierarchical structure for materials," *Poroshk. Metall.*, Nos. 5-6, pp. 105-127, 2002.

[26] M. S. Koval'chenko, "Mechanical properties of porous isotropic material," *Poroshk. Metall.*, No. 3, pp. 89-96, 1993; No. 4, pp. 89-94, 1993; No. 5, pp. 64-70, 1993; Nos. 9-10, pp. 75-83, 1996.

[27] J. K. Mackenzie, "The elastic constants of a solid containing spherical holes," *Proceedings of the Physical Society B*, Vol. 63, No. 1, pp. 2-11, 1950.

[28] J. D. Eshelby, "The determination of the elastic field of an ellipsoidal inclusion and related problems," *Proceedings of the Royal Society of London A: Mathematical, Physical and Engineering Sciences A*, Vol. 241, No. 1226, 1957.

[29] R. Hill, "Elastic properties of reinforced solids: some theoretical principles," *Journal of the Mechanics and Physics of Solids*, Vol. 11, No. 5, pp. 357-372, 1963.

[30] V. V. Skorokhod, "Calculation of elastic isotropic moduli for dispersed solid mixtures," *Poroshk. Metall.*, No. 1, pp. 50-55, 1961.

[31] Y. H. Zhao, G. P. Tandon, and G. J. Weng, "Elastic moduli for a class of porous materials," *Acta Metallurgica*, Vol. 76, Nos. 1-2, pp. 105-136, 1989.

[32] B. Budiansky and R. J. O'Connell, "Elastic moduli of cracked solid," *International Journal of Solids and Structures*, Vol. 12, No. 2, pp. 81-97, 1976.

[33] Z. Hashin and S. Shrikman, “A variational approach to the theory of the elastic behavior of multiphase materials,” *Journal of the Mechanics and Physics of Solids*, Vol. 11, No. 2, pp. 127-140, 1963.

[34] R. Cytermann, “Contiguity and properties of porous materials,” *Proc. Conf. Fragm. Form., Flow Fract. Media, Bristol*, 1986.

[35] A. G. Zherdin, Yu. N. Podrezov, S. A. Firstov, and L. T. Shtyka, “Effect of porosity on the microplastic deformation in powder materials based on iron,” *Poroshk. Metall.*, No. 7, pp. 79-84, 1989.

[36] B. Champagne and A. Roch, “Mechanical properties of hot-pressed B-B4C materials,” *Journal of the American Ceramic Society*, Vol. 62, Nos. 3-4, pp. 149-153, 1979.

[37] G. Hollenberg and J. Waldher, “The elastic modulus and fracture of boron carbide,” *Journal of the American Ceramic Society*, Vol. 63, Nos. 11-12, pp. 610-613, 1980.

[38] O. Gillia and D. Bouvard, “Continuum modelling of sintering of powder compacts,” *in: Recent Developments in Computer Modelling of Powder Metallurgy Processes, A. Zavaliangos and A. Laptev (eds.), IOS Press, Amsterdam; Washington*, pp. 122-134, 2001.

[39] M. B. Sthtern, “Model of the deformation of porous materials taking account of pore formation,” *Poroshk. Metall.*, No. 5, pp. 28-34, 1989; No. 6, pp. 34-39, 1989.

[40] M. S. Koval’chenko, “Elasticity and viscosity of isotropic porous materials, *Powder Metallurgy and Metal Ceramics*, Vol. 42, Nos. 1-2, pp.81-87, 2003.

[41] S. Suresh and A. Mortensen, “Fundamentals of Functionally Graded Materials: Processing and Thermomechanical Behaviour of Graded Metals and Metal-Ceramic Composites,” *The University Press, Cambridge*, pp. 16-33, pp. 82-95, 1998.

[42] Y. Miyamoto, W. A. Kaysser, B. H. Babin, A. Kawasaki, and R. G. Ford, “Functionally Graded Materials: Design, Processing and Applications,” *Kluwer Academic Publishers, Boston*, pp. 68-88, pp. 161-186, 1999.

[43] R. Watanabe, T. Nishida, and T. Hirai, “Technological Overview: Present status of Research on Design and Processing of Functionally Graded Materials,” *Metals and Materials International*, Vol. 9, No. 6, pp. 513-519, 2003.

[44] V. Birman and L. W. Byrd, “Modeling and Analysis of Functionally Graded Materials and Structures,” *Applied Mechanics Reviews*, Vol. 60, pp. 195-216, 2007.

[45] B. Zhang and M. M. Gasik, “Stress evolution in graded materials during densification by sintering processes,” *Computational Materials Science*, Vol. 25, pp. 264–271, 2002.

[46] M. L. Pines and H. A. Bruck, “Pressureless sintering of particle-reinforced metal–ceramic composites for functionally graded materials: Part I. Porosity reduction models,” *Acta Materialia*, Vol. 54, pp. 1457-146, 2006.

[47] M. L. Pines and H. A. Bruck, “Pressureless sintering of particle-reinforced metal–ceramic composites for functionally graded

materials: Part II. Sintering model," *Acta Materialia*, Vol. 54, pp. 1467-1474, 2006.

[48] Y. M. Shabana, H. A. Bruck, M. L. Pines, and J. G. Kruft, "Modeling the evolution of stress due to differential shrinkage in powder-processed functionally graded metal–ceramic composites during pressureless sintering," *International Journal of Solids and Structures*, Vol. 43, pp. 7852-7868, 2006.

[49] A. J. Markworth, K. S. Ramesh, and W. P. Parks Jr., "Modelling studies applied to functionally graded materials," *Journal of materials science*, Vol.30, pp.2183-2193, 1995.

[50] T. Fuchiyama and N. Noda, "Analysis of thermal stress in a plate of functionally gradient material," *JSAE Review*, Vol. 16, pp. 263-268, 1995.

[51] K. S. Ravichandran, "Thermal residual stresses in a functionally graded material system," *Materials Science and Engineering: A*, Vol. 201, pp. 269-276, 1995.

[52] J. Aboundi, M. J. Pindera, and S. M. Arnold, "Thermo-inelastic response of functionally graded composites," *International Journal of Solids and Structures*, Vol. 32, No. 12, pp. 1675-1710, 1995.

[53] J. Aboudi, M. J. Pindera, and S. M. Arnold, "Thermoelastic theory for the response of materials functionally graded in two directions," *International Journal of Solids and Structures*, Vol. 33, No. 7, pp. 931-966, 1996.

[54] J. Aboundi, M. J. Pindera, and S. M. Arnold, "Microstructural

optimizations of functionally graded composites subjected to a thermal gradient via the coupled higher-order theory," *Composites Part B: Engineering*, Vol. 28, Issue 1-2, pp. 93-108, 1997.

[55] J. Aboundi, M. J. Pindera, and S. M. Arnold, "Higher-order theory for functionally graded composites," *Composites Part B: Engineering*, Vol. 30, pp. 777-832, 1999.

[56] J. N. Reddy and C. D. Chin, "Thermomechanical analysis of functionally graded cylinders and plates," *Journal of Thermal Stresses*, Vol. 21, pp. 593-626, 1998.

[57] J. N. Reddy and Z. Q. Cheng, "Three-dimensional thermomechanical deformations of functionally graded rectangular plates," *European Journal of Mechanics- A, Solids*, Vol. 20, No. 5, pp. 841-855, 2001.

[58] J. N. Reddy, "Analysis of functionally graded plates," *International Journal for Numerical Methods in Engineering*, Vol. 47, Issue 1-3, pp. 663-684, 2000.

[59] Z. Q. Cheng and R. C. Batra, "Three-dimensional thermoelastic deformations of a functionally gradedelliptic plate," *Composites Part B: Engineering*, Vol. 31, pp. 97-106, 2000.

[60] S. S. Vel and R. C. Batra, "Exact solution for thermoelastic deformations of a functionally graded thick rectangular plates," *AIAA Journal*, Vol. 40, No. 7, pp. 1421-1433, 2002.

[61] S. S. Vel and R. C. Batra, "Three-dimensional analysis of transient thermal stresses in functionally graded plates," *International Journal of Solids and Structures*, Vol. 40, pp. 7181-7196, 2003.

[62] S. S. Vel and R. C. Batra, “Three-dimensional exact solution for the vibration of functionally graded rectangular plates,” *Journal of Sound and Vibration*, Vol. 272, pp. 703-730, 2004.

[63] L. F. Qian, R. C. Batra, and L. M. Chen, “Static and dynamic deformations of thick functionally graded elastic plates by using higher-order shear and normal deformable plate theory and meshless local Petrov-Galerkin method,” *Composites Part B: Engineering*, Vol. 35, pp. 685-697, 2004.

[64] J. R. Cho and J. T. Oden, “Functionally graded material: A parametric study on thermal-stress characteristics using the Crank-Nicolson Falerkin scheme,” *Computer Methods in Applied Mechanics and Engineering*, Vol. 188, pp. 17-38, 2000.

[65] J. R. Cho and D. Y. Ha, “Averaging and finite-element discretization approaches in the numerical analysis of functionally graded materials,” *Materials Science and Engineering: A*, Vol. 302, pp. 187-196, 2001.

[66] B. L. Wang and Z. H. Tian, “Application of finite element-finite difference method to the determination of transient temperature field in functionally graded materials,” *Finite Element in Analysis and Design*, Vol. 41, pp. 335-349, 2005.

[67] M. M. Gasic, “Micromechanical modeling of functionally graded materials,” *Computational Materials Science*, Vol. 13, pp. 42-55, 1998.

[68] R. Rodriguez-Castro, R. C. Wetherhold, and M. H. Kelestemur, “Microstructure and mechanical behavior of functionally graded

AlA359/SiCp composite," *Materials Science and Engineering: A*, Vol. 323, pp. 445-456, 2002.

[69] H. Tsukamoto, "Analytical method of inelastic thermal stresses on an functionally graded material plate by a combination of micro- and macromechanical approaches," *Composites Part B: Engineering*, Vol. 34, pp. 561-568, 2003.

[70] R. R. Kumar and M. Wang, "Modulus and hardness evaluations of sintered bioceramic powders and functionally graded bioactive composites by nano-indentation technique," *Materials Science and Engineering: A*, Vol. 338, Issue 1-2, pp. 230-236, 2002.

[71] G. Bao and L. Wang, "Multiple cracking in functionally graded ceramic/metal coating," *International Journal of Solids and Structures*, Vol. 32, No. 19, pp. 2853-2871, 1995.

[72] Z. H. Jin and R. C. Batra, "R-curve and strength behavior of a functionally graded material," *Materials and Engineering: A*, Vol. 242, pp. 70-76, 1998.

[73] R. J. Butcher, C. E. Rousseau, and H. V. Tippur, "A functionally graded particulate composite: preparation, measurements and failure analysis," *Acta Materilia*, Vol. 47, No. 1, pp. 259-268, 1999.

[74] H. A. Bruck and A. L. Gershon, "Three-demensional effects near the interface in a functionally graded Ni-Al_2O_3 plate specimen," *International Journal of Solides and Structures*, Vol. 39, pp. 547-557, 2002.

[75] T. L. Becker Jr, R. M. Cannon, and R. O. Richie, "Statistical fracture

modeling: crack path and fracture criteria with application to homogeneous and functionally graded materials," *Engineering Fracture Mechanics*, Vol. 69, pp. 1521-155, 2002.

[76] J. R. Cho and J. H. Choi, "A yield-criteria tailoring of the volume fraction in metal-ceramic functionally graded material," *European Journal of Mechanics- A/Solids*, Vol. 23, pp. 271-281, 2004.

[77] L. Ma, L. Z. Wu, Z. G. Zhou, and L. C. Guo, "Fracture analysis of a functionally graded piezoelectric strip," *Composite structures*, Vol. 69, Issue 3, pp. 294-300, 2005.

[78] Z. Zhang and G. H. Paulino, "Cohesive zone modeling of dynamic failure in homogeneous and functionally graded materials," *International Journal of Plasticity*, Vol. 21, pp. 1195-1254, 2005.

[79] X. C. Zhang, B. S. Xu, H. D. Wang, and Y. X. Wu, "Modeling of the residual stress in plasma-spraying functionally grade ZrO_3/NiCoAlY coating using finite element method," *Materials and Design*, Vol. 27, Issue 4, pp, 308-315, 2006.

[80] MatWeb: www.matweb.com

[81] D. L. Logan, "A Firsr Course in the Finite Element Method: Third Edition," *BROOKS/COLE*, pp. 532–536, 2002.

[82] R. D. Cook, D. S. Malkus, M. E. Plesha, and R. J. Witt, "Concepts and Applications of Finite Element Analysis: Fourth Edition," *John Wiley and Sons, Inc.*, pp. 508–510, 2002.

[83] Taimei Chemicals Co.,Ltd: http://www.taimei-chem.co.jp/ product/english/01.html

[84] K. Wakashima and H. Tsukamoto, “Mean-field micromechanics model and its application to the analysis of thermomechanical behavior of composite materials,” *Materials Science and Engineering A*, Vol. 146, pp. 64-76, 1991.

[85] R. M. Sprigs “Expression for effect of porosity on elastic modulus of polycrystalline refractory materials, particularly aluminium oxide,” *Journal of The American Ceramic Society*, Vol. 44, pp. 628–629, 1961.

[86] D. P. H. Hasselman, “On the Porosity Dependence of the Elastic Moduli of Polycrystalline Refractory Materials,” *Journal of The American Ceramic Society*, Vol. 45, No. 9, pp. 452-453, 1962.

[87] P. H. Bompard and D. Francois. "Effects of porosity on fatigue crack propagation in sintered nickel." *ICF6, New Delhi (India) 1984*, 2013.

[88] R. L. Coble and W. D. Kingery, “Effect of porosity on physical properties of sintered alumina,” *Journal of the American Ceramic Society*, Vol. 39, pp. 377–385, 1956

[89] H. M. Ledbetter and R. P. Reed, “Elastic Properties of Metals and Alloys, I. Iron, Nickel, and Iron-Nickel Alloys,” *Journal of Physical and Chemical Reference Data*, Vol. 2, No. 3, pp. 531-618, 1973.

[90] R. Farraro and R. B. McLellan, “Temperature dependence of the Young’s modulus and shear modulus of pure nickel, platinum, and molybdenum,” *Metallurgical and Materials Transactions A*, Vol.8, No.10, pp.1563-1565, 1977.

[91] N. Saunders, A. P. Miodownik, and J. P. Schille, “Modelling of the thermo-physical and physical properties for solidification of Ni-based superalloys,” *Journal of Materials Science*, Vol.39, pp.7237-7243,

2004.

[92] B. A. Latella and T. Liu, “High-Temperature Young’s Modulus of Alumina During Sintering,” *Journal of the American Ceramic Society*, Vol. 88, No. 3, pp.773-776, 2005.

[93] H. J. Frost and M. F. Ashby, “Deformation Mechanism Maps,” *Pergamon, New York*, 1982.

[94] S. P. Bhat and C. Laird, “High Temperature Cyclic Deformation of Nickel,” *Fatigue of Engineering Materials and Structures*, Vol. 1, pp. 59-77, 1979.

[95] S. Shuji, M. Norimitsu, K. Yasuharu, and W. Fumihiro, “The Poisson's ratio of engineering ceramics at elevated temperature,” *Journal of Materials Science Letters*, No. 10, pp. 282-284, 1991.

초 록

본 연구는 열에너지 효율을 높이기 위한 방안으로 작동 온도를 높이기 위한 열 저항성 재료를 제작하는 것이 목표이다. 이를 위해 경사기능재료를 도입하였고, 열 차폐 재료로 알루미나(Alumina, Al_2O_3)를, 구조 재료로는 니켈(Nickel, Ni)을 사용하였다. 그리고 경사기능재료의 제작방법으로 효율과 비용을 감안하여 분말야금법과 상압소결법을 사용하였다. 하지만 이러한 경사기능재료를 기계부품에 적용하기 위해서는 기계공학적 지식뿐만 아니라 재료과학적 지식도 요구된다. 이에 기계공학자의 입장에서 재료과학 분야의 연구를 데이터베이스화 시켜 경사기능재료 형태의 기계부품을 보다 효율적이고 신속하게 설계·제조하는 시스템을 만들려 한다.

이를 위해 본 연구에서는 경사기능재료 형태의 부품을 제작할 때 필요한 재료과학 분야의 변수를 데이터베이스화 시키고, 이에 필요한 실험을 표준화하여 최소의 실험으로 원하는 물성을 산출할 수 있는 물성 산출 모델을 만들기 위한 기초연구를 다음과 같이 수행하였다.

1. 상압소결법으로 제작된 경사기능재료의 기공률 측정방법
2. 기공률에 따른 니켈/알루미나 경사기능재료의 물성 산출 방법 및 모델
3. 니켈/알루미나 경사기능재료의 각 층에 대한 소결수축율 예측 방법 및 모델

수행된 연구의 결과인 물성 산출 모델들은 경사기능재료 제작에서 재료과학 분야의 데이터베이스화를 위한 핵심 요소이다. 따라서 본 연구에서 제시한 모델들에 의해 산출된 재료 물성으로 경사기능재료의 소결 변형 해석을 수행하였고, 이는 실험에 통해 측정된 재료 물성으로 수행된 해석 결과와의 비교로 제시된 모델들이 신뢰성이 있음을 확인하였다. 또한 본 연구에서 제시한 모델들에 의해 산출된 물성으로 경사기능재료의 열잔류응력 해석을 수행하였고, 이를 통해 경사기능재료의 파손 여부와 파손 위치를 예측하였다. 그리고 예측된 결과는 실제 제작된 경사기능재료 시편의 결과와 일치하였다.

이를 통해 기계공학자가 경사기능재료를 설계하고 제작할 때 본 연구에 의해 구축될 재료과학 분야 데이터베이스를 이용하면 경사기능재료의 물성을 보다 효율적으로 산출할 수 있고, 이 결과를 이용한 수치해석을 통해 경사기능재료의 응력과 변위를 예측할 수 있게 되어 보다 성능이 뛰어난 기계부품을 제작할 수 있게 된다.

주요어 : 니켈/알루미나 경사기능재료, 기공률 측정 방법, 물성 산출 모델, 소결수축율 예측 모델, 열잔류응력 해석

학 번 : 2005-31034